Exploring the Lower Limb of the Atlantic Meridional Overturning Circulation

by

Sijia Zou

Department of Earth and Ocean Sciences
Duke University

Date:_____
Approved:

_____
M. Susan Lozier, Supervisor

_____
Paul Baker

_____
Nicolas Cassar

_____
Amy S. Bower

_____

Dissertation submitted in partial fulfillment of
the requirements for the degree of Doctor
of Philosophy in the Department of
Earth and Ocean Sciences in the Graduate School
of Duke University

2018

ABSTRACT

Exploring the Lower Limb of the Atlantic Meridional Overturning Circulation

by

Sijia Zou

Department of Earth and Ocean Sciences
Duke University

Date:_____
Approved:

_____
M. Susan Lozier, Supervisor

_____
Paul Baker

_____
Nicolas Cassar

_____
Amy S. Bower

_____

An abstract of a dissertation submitted in partial
fulfillment of the requirements for the degree
of Doctor of Philosophy in the Department of
Earth and Ocean Sciences in the Graduate School of
Duke University

2018

Abstract

The Atlantic Meridional Overturning Circulation (AMOC) is characterized as a northward upper limb that carries warm near-surface waters from southern latitudes to the subpolar North Atlantic, and a southward lower limb that transports cold deep waters back to the southern latitudes. Due to its special role in distributing heat, carbon and water masses globally, AMOC as an essential part in the climate system, has long been a strong focus within the ocean community. For decades, AMOC variability has been attributed to changes in deep water production at high latitudes in the North Atlantic through a geostrophic response in the Deep Western Boundary Current (DWBC), the assumed major export pathway of the deep waters. However, recent Lagrangian studies have revealed the importance of eddy-driven interior pathways, challenging the traditional DWBC-dominated spreading pattern, hence the linkage between deep water formation and AMOC. Under the new spreading scheme of the deep waters, this dissertation provides an extended Lagrangian analysis on the spreading pathways of two major deep waters, Labrador Sea Water (LSW) and Iceland Scotland Overflow Water (ISOW), and re-examines the relationships among deep water production, deep water export and the strength of AMOC.

A Lagrangian simulation of newly-formed LSW in an ocean/sea ice model (1/4°) reveals strong recirculation of the water mass in the subpolar gyre, with a small portion

exported to the subtropical gyre through an advective-diffusive pathway. Furthermore, no significant correlation between LSW production and its Lagrangian export to the subtropical gyre is found on interannual to decadal time scales, suggesting a negligible or at best modest impact of LSW production on the subtropical AMOC.

In a combined Lagrangian and Eulerian frame, a first comprehensive description of ISOW spreading branches in the eastern North Atlantic is presented with observational data and output from an eddy-resolving ocean model. The major export pathway for ISOW is shown to be the southward branch into the Western European Basin, instead of the branch through the Charlie Gibbs Fracture Zone, the traditional DWBC pathway. Interestingly, these two branches show compensating relationships in the model, a result assumed to reflect these pathways' interactions with the North Atlantic Current in magnitude and/or position shift.

Finally, with output from ocean circulation models and an ocean reanalysis dataset, the meridional connection of the deep water transport anomalies and their relationships with AMOC are assessed. It is shown that deep water transport anomalies in the subpolar gyre do not propagate coherently to the subtropical gyre in general, particularly so for Upper North Atlantic Deep Water (UNADW, containing LSW). Furthermore, while UNADW and Lower North Atlantic Deep Water (LNADW, containing overflow waters) transports in the subpolar gyre are linked to local AMOC strength on interannual to decadal time scales, in the subtropical gyre only LNADW

transport variability shows this linkage, the latter results consistent with observations. These analyses suggest a dominance of gyre-specific, rather than basin-wide, mechanisms for water mass transport variability. Thus, latitudinal coherence in AMOC is likely unrelated to continuity in water mass transport anomalies. An exception to this generalization is possible with strong LNADW transport events.

Taken together, this dissertation emphasizes the importance of interior pathways to the export of deep waters from the subpolar to the subtropical gyre. It also reveals a tenuous linkage between deep water production and AMOC strength at subtropical latitudes on interannual to decadal time scales.

Dedication

I would like to dedicate this thesis to my beloved parents, 邹广德 (Guangde Zou) and 沈玉凤 (Yufeng Shen), for their unconditional love, for their faith in life, for their encouragements when I face the unknown.

Contents

List of Figures

List of Abbreviations

Commonly used abbreviations in this dissertation:

AMOC	Atlantic Meridional Overturning Circulation
BFZ	Bight Fracture Zone
BPT	Bottom Pressure Torque
CGFZ	Charlie-Gibbs Fracture Zone
DSOW	Denmark Strait Overflow Water
DWBC	Deep Western Boundary Current
ISOW	Iceland Scotland Overflow Water
LDW	Lower Deep Water
LNADW	Lower North Atlantic Deep Water
LSW	Labrador Sea Water
MAR	Mid-Atlantic Ridge
MOW	Mediterranean Outflow Water
NADW	North Atlantic Deep Water
NAO	North Atlantic Oscillation
NAC	North Atlantic Current
OW	Overflow Waters
OSNAP	Overturning in the Subpolar North Atlantic Program

PV	Potential Vorticity
RR	Reykjanes Ridge
RAFOS	Range and Fixing of Sound
Sv	Sverdrup
UNADW	Upper North Atlantic Deep Water
WEB	Western European Basin
WSC	Wind Stress Curl

Acknowledgements

First and foremost, I would like to express my sincere appreciation to my advisor Dr. Susan Lozier. It has been a great honor to be her Ph.D. student both for science and for life. I appreciate her generosity in time, advices, encouragements, and funding support to make my Ph.D. life stimulating and productive. I am thankful for her understanding and patience for me, an international student who was new to everything in the U.S., to gradually adapt to Ph.D. life and grow into an increasingly independent researcher. I am also thankful for her excellent example as a female scientist, who is enthusiastic for research and joyful for life.

I would like to extend my thanks to Dr. Amy Bower, Dr. William Johns, Dr. Walter Zenk, and Dr. Martha Buckley for their insights on my work and fruitful collaborations. I am grateful for Dr. Arne Biastoch and Dr. Claus Böning who hosted me as a visiting student at GEOMAR in Germany and helped me with data and techniques I need for this dissertation. Additionally, I would like to thank Dr. Paul Baker and Dr. Nicolas Cassar for serving on my dissertation committee and for helpful discussions during committee meetings.

I am lucky to be at Duke with wonderful colleagues and friends. I owe special thanks to Nicholas Foukal, my 5-year classmate and labmate who is always there for any support. His nodding in audience always release my anxiety when I give presentations. I

am also thankful for past and present Lozier Lab members, particularly Feili Li, Stefan Gary, Femke de Jong, Laifang Li, Ryan Peabody, Kimberley Drouin, and Cassar Lab members, particularly Zuchuan Li and Weiyi Tang, for their scientific advices and friendships.

I am blessed with every support from my lifelong friend, Qiuying Zhang. We share together, grow up together and will grow old together. I will always thank my beloved parents, Guangde Zou and Yufeng Shen, who make every effort to support me, love me, and to make me who I am. Thank you all.

1. Introduction

1.1 The Atlantic Meridional Overturning Circulation

The Atlantic Meridional Overturning Circulation (AMOC), a fundamental component of the climate system, is characterized as a northward flow of warm, saline upper waters to the subpolar North Atlantic (i.e. the AMOC upper limb), and a southward return flow of cold, fresh deep waters (i.e. the AMOC lower limb) (Figure 1). The two limbs are connected at high latitudes in the North Atlantic, where the warm upper waters sink to depth by losing heat to the atmosphere, thereby forming deep waters, a process referred to as convection. During convection, excessive heat, carbon, and oxygen are brought from the ocean surface to the deep ocean and are then exported globally.

The role of AMOC in the earth system is essential. It re-distributes heat between the tropics and polar latitudes and keeps the northern hemisphere warm and suitable to life. It also serves as a reservoir for additional carbon in the atmosphere and modifies global warming (Takahashi, et al., 2009). Studies also indicate an influence of AMOC on sea level variability along the eastern coast of North America (Vellinga & Wood, 2008), Atlantic hurricane activity (Zhang & Delworth, 2006; Knight, et al., 2006), and Arctic sea ice loss (Serreze, et al., 2007), etc. It is thus compelling and essential to understand how AMOC varies and what drives that variability.

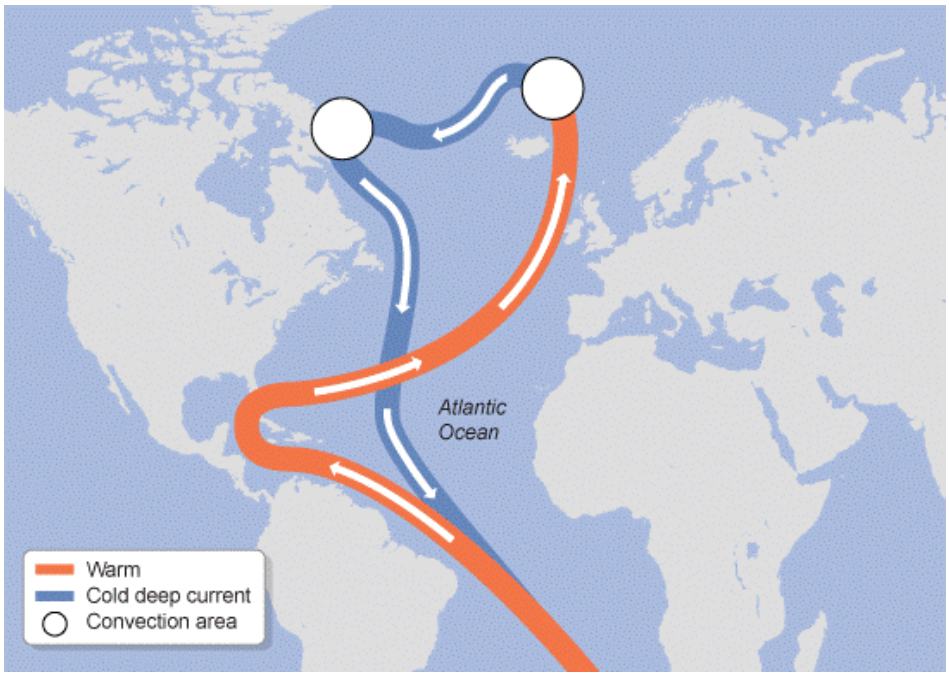

Figure 1: A schematic of the AMOC. Orange (blue) curves represent the warm upper limb (cold lower limb). White circles denote the major convective regions. This figure is reprinted from *BBC weather and climate*.

1.2 The North Atlantic Deep Waters and their linkage to AMOC

For decades, AMOC variability has been linked to the production of North Atlantic Deep Waters (NADW) in subpolar and subarctic North Atlantic (Delworth, et al., 1993; Zhang, 2010; Yeager & Danabasoglu, 2014). NADW, which constitutes the southward lower limb of AMOC, has two primary components: the shallower Labrador Sea Water (LSW) and the deeper Nordic Seas Overflow Water (OW).

Strong cooling during winters leads to unstable surface stratification, which drives convective overturning to depths of approximately 1500m in the central Labrador Sea (Talley & McCartney, 1982). The product of this overturning is a distinct water mass (LSW) with relatively low temperature, salinity ((Talley & McCartney, 1982; Pickart, et

al., 2002; Stramma, et al., 2004; Yashayaev, 2007), potential vorticity (PV) (Talley & McCartney, 1982; Stramma, et al., 2004) and high concentrations of dissolved oxygen (Pickart, et al., 2002) and chlorofluorocarbons (CFCs) (Rhein, et al., 2002; Kieke, et al., 2007). The exchange of heat and freshwater across the air/sea interface and the horizontal advection of heat and salt into the basin via boundary currents have been proposed as the two major factors that create variability in LSW volume and properties (Stramma, et al., 2004). Interannual and interdecadal variability of LSW properties, measured using up to 60 years of hydrographic data, have been linked to changes in the North Atlantic Oscillation (NAO) index (Stramma, et al., 2004; Yashayaev, 2007; Curry, et al., 1998; Kieke & Yashayaev, 2015). A relatively shallow, warm and salty layer of LSW was produced from the 1950s to 1970 when the NAO index was negative, a state characterized by a small difference between the Azores High and Icelandic Low, reduced heat flux to the atmosphere and weak westerlies in the subpolar region (Sarafanov, 2009; van Aken, et al., 2011). The decreased heat flux and the relatively weak westward extension of the subpolar gyre together contributed to the warm and salty intermediate water formed in the Labrador Sea (Sarafanov, 2009). In the early 1990s, when the NAO was positive, the strongest recorded convection occurred, resulting in a thick, cold and fresh LSW layer. From 1994 until 2008, weak convection and steady warming were observed. Enhanced LSW formation resumed in 2008, and was attributed to strong atmospheric cooling (Yashayaev & Loder, 2009). And most recently,

observations in the central Labrador Sea revealed a strong convection during the 2016 winter (Yashayaev & Loder, 2017).

OW is formed in the Nordic Seas via open-ocean convection in the Greenland Sea, dense water formation along the Arctic shelves and the transformation of Atlantic water (Rudels, et al., 1999; Eldevik, et al., 2009). After formation, one branch of OW flows into the North Atlantic through the Denmark Strait between Greenland and Iceland, and thus the water following this branch is referred to as the Denmark Strait Overflow Water (DSOW). The other branch flows into the eastern subpolar gyre between Iceland and Scotland, mainly through the Faroe-Shetland Channel, with a small portion over the Iceland-Faroe Ridge. The water following this branch is named as the Iceland Scotland Overflow Water (ISOW). Both branches have a mean transport of ~3Sv, which has remained relatively stable over the past five decades (Olsen, et al., 2008). After entering the subpolar North Atlantic, OW fills the deep ocean basin with the bottom layer occupied by DSOW and the less dense ISOW above it. The lighter density of ISOW is due to its active entrainment with ambient waters, such as LSW, as it spreads within the Iceland Basin (Fleischmann, et al., 2001; van Aken & Boer, 1995).

Variability in the production of these deep waters has been assumed to generate changes in the deep southward return flow (i.e. the AMOC lower limb): a stronger production of the deep waters generates positive density anomalies that propagate along the western boundary, enhancing the cross-basin density gradient which

strengthens the local flow according to geostrophic dynamics. This strengthened flow in the AMOC lower limb takes place across latitudes, resulting in a latitudinally stronger AMOC (Buckley, et al., 2012; Polo, et al., 2014; Biastoch, et al., 2008). Modeling studies have found that on decadal time scales, this linkage is dominated by the production rate of LSW, while on multi-decadal time scales, the linkage is driven by OW formation (Latif, et al., 2006; Zhang, 2008; Biastoch, et al., 2008).

1.3 NADW spreading in Eulerian frame: the DWBC

Traditionally, the export of NADW from the subpolar to the subtropical gyre was theoretically assumed to follow the DWBC. Using the first order vorticity balance between planetary vorticity and vortex stretching, Stommel and Arons (1960) showed that when deep waters overflow into an ocean basin (i.e. the OW into the North Atlantic), upwelling results elsewhere in the basin. Since the upwelling-induced vorticity has to be balanced by a poleward flow in the basin interior, the requirement of mass conservation is met by a southward flow that is concentrated along the western boundary.

Modern observations along the western boundary of the North Atlantic have revealed southward transport cores in both LSW and OW layers (Talley & McCartney, 1982; Pickart, 1992; Smethie, et al., 2000; Toole, et al., 2017). In the eastern North Atlantic, where ISOW enters the basin, an ISOW transport core is also observed in the DWBC

along the eastern flank of the Reykjanes Ridge (RR) (Saunders, 1996; Kanzow & Zenk., 2014).

These Eulerian-based observations (i.e. measurements at fixed locations) collectively led to the prevailing view that NADW primarily exports to the subtropical gyre by following the DWBC, and consequently, that DWBC variability reflects changes in NADW production, as well as AMOC variability.

1.4 NADW spreading in Lagrangian frame: the Interior Pathway

The Stommel and Arons theory, however, ignores an important factor in the vorticity equation, which is the vorticity flux induced by eddies. The impact of eddies on deep water spreading pathways, unfortunately, is difficult to detect from Eulerian-based measurements conducted in the DWBC. Emerging Lagrangian studies (i.e. measurements following the waters), on the other hand, have provided a unique perspective on the deep water spreading structure, thereby questioning the representativeness of the DWBC as the only export pathway.

For example, Lavender, et al. (2005) studied the mid-depth circulation in the subpolar North Atlantic with neutrally-buoyant, profiling floats. Floats that left the Labrador Sea initially drifted southeastward along the Labrador slope, but none followed the DWBC beyond 44°N. Similarly, for the RAFOS floats launched at LSW depths in the DWBC off the Labrador coast from 2003 to 2006, only 8% were able to enter the subtropical basin via the DWBC (Bower, et al., 2009). Instead, the majority of

the RAFOS floats that reached the subtropical basin from the subpolar latitudes did so by interior pathways (Bower, et al., 2009; Lozier, 2012).

While there has been to date no observational Lagrangian study that describes the spreading OW pathways, simulated Lagrangian trajectories have revealed interior pathways for both ISOW and DSOW in the western North Atlantic (Gary, et al., 2011; Lozier, et al., 2013).

Taken together, these Lagrangian studies emphasize the importance of eddy-driven interior pathways in exporting the NADW to the subtropical gyre, and suggest that the DWBC alone cannot capture the full range of variability of the AMOC lower limb. This finding has implications for where and how the AMOC lower limb is measured. Furthermore, under this new Lagrangian spreading scheme, the linkages among deep water production, deep water export and AMOC strength are set in a new context.

1.5 Research highlights

In this dissertation, in a combined Eulerian and Lagrangian frame, I re-visit the relationship between deep water production and AMOC strength by detailing the processes and linkages involved.

I first explore the linkage between deep water production and its export from the subpolar to the subtropical gyre with a focus on LSW (Chapter 2). Based on model output, no significant correlation is found between the LSW production and its

Lagrangian export on interannual to decadal time scales (Zou & Lozier, 2016). That is to say, an anomalously large (small) production of LSW does not result in an increased (decreased) LSW export to the subtropical gyre in subsequent years, suggesting a negligible or at best modest impact of LSW production on the subtropical AMOC.

As stated above, the amount of OW that flows into the North Atlantic has been quite steady. Thus, any OW-related AMOC variations have to be produced by the spreading processes south of the ridge (Olsen, et al., 2008). However, no observational study so far has explored OW spreading pathways from a Lagrangian perspective, primarily due to data limitation. Additionally, no study to date has assessed the temporal variability of different OW spreading branches. In Chapter 3, I focus on ISOW and use a combination of previously unreported current meter data, hydrographic data, RAFOS float data, and a high resolution (1/12°) numerical ocean model to study its spreading pathways in the eastern North Atlantic. From both Eulerian and Lagrangian perspectives, three major export branches are revealed: an escape branch through fractures in RR; a westward branch via the Charlie Gibbs Fracture Zone (CGFZ); and a southward branch along both flanks of the Mid-Atlantic Ridge (MAR). A model-based investigation provides a first look at the relative importance and temporal variability of these export pathways. It is shown that the southward branch carries most of the ISOW out of Iceland Basin. Interestingly, this branch shows an anti-correlation with the branch

through the CGFZ, a result assumed to reflect these pathways' interactions with the North Atlantic Current (NAC) in magnitude and/or position shift.

In Chapter 4, I investigate the meridional connection of NADW transport anomalies between the subpolar gyre and subtropical gyre, and the linkage between these transport anomalies to AMOC anomalies at each latitude. With output from two ocean circulation models and one ocean reanalysis dataset, it is found that NADW anomalies in the subpolar gyre do not generally propagate coherently to the subtropical gyre, particularly so for Upper NADW (UNADW, containing LSW). Furthermore, while UNADW and Lower NADW (LNADW, containing OW) transports in the subpolar gyre are linked to local AMOC strength on interannual to decadal time scales, in the subtropical gyre only LNADW transport variability shows this linkage. Collectively, our analyses suggest a dominance of gyre-specific, rather than basin-wide, mechanisms for water mass transport variability. Thus, latitudinal coherence in AMOC is likely unrelated to continuity in water mass transport anomalies. An exception to this generalization is possible with strong LNADW transport events.

Finally, in Chapter 5, some ongoing studies are discussed. A decomposition of AMOC strength variability across the North Atlantic has been conducted with an Empirical Orthogonal Function (EOF) analysis. The AMOC variability is shown to constitute a meridionally coherent mode that extends from the subpolar to the subtropical gyre, and a gyre-specific mode that shows out-of-phase variability between

the two gyres. This study points to the subpolar and subtropical gyre-gyre boundary as a key region to detect the coherent mode, and indicates that the wind stress might be responsible for the gyre-specific mode. Another ongoing study, focused on the contradiction between LSW property transit and its advection is also discussed.

2. Breaking the Linkage between LSW Production and Its Export

In this Chapter, a detailed description of the spreading pathways and time scales for the newly-formed LSW are provided. The relationship between LSW production and LSW export to the subtropics is also explored. This work has been published in *Journal of Physical Oceanography* (Zou & Lozier, 2016).

2.1 Introduction

For decades, it was assumed that convection strength in the Labrador Sea would alter deep water export from the subpolar gyre and modify downstream properties at intermediate depths in the North Atlantic. As for the latter, observational studies have shown a strong correlation between LSW thickness and property anomalies near Bermuda (Curry, et al., 1998), with the former leading by 6 years. Similarly, Molinari et al. (1998) and van Sebille et al. (2011) both reported a 10-year transit time of the property signals from Labrador Sea to 26.5°N in the DWBC within LSW layers. A more recent study (Pena-Molino, et al., 2011) observed that water properties in the classical LSW layer within DWBC at the Line W mooring array (39°N), measured in the early 2000s, reflect the intense Labrador Sea convection during the mid-1990s, indicating a 9-year propagation time scale from the central Labrador Sea to Line W. As for the relationship between LSW production and deep water export, some past studies indicate a linkage between LSW production and DWBC strength (Böning, et al., 2006; Han, et al., 2010), yet

other show a contrary result (Schott, et al., 2004; Dengler, et al., 2006). Relatedly, a linkage between LSW production and AMOC strength, via fast boundary wave propagation, has been revealed from a modeling study (Biastoch, et al., 2008) with interannual buoyancy forcing. However, when interannual wind forcing was also considered, the LSW production and AMOC relationship was masked by higher frequency variability in the AMOC anomalies. Despite this focus on LSW production and its downstream impact, currently unanswered is whether there is a relationship between LSW production and the export of that water mass to the subtropical North Atlantic through advection.

Specifically, I seek to understand the extent to which LSW production impacts the volume of newly-formed LSW and blended LSW that are advected across the inter-gyre boundaries to the subtropical basin, and across 30°N, where LSW and the other components of the southward flowing NADW are less likely to recirculate back to the subpolar gyre. By doing so, I aim to improve the understanding of how convection in the Labrador Sea impacts the lower limb of the AMOC.

2.2 Data and methods

2.2.1 Hydrographic data in the Labrador Sea

The Labrador Sea Monitoring Program of Fisheries and Oceans Canada has been conducting oceanographic observations in the Labrador Sea since 1990 along the Atlantic Repeat Hydrography Line 7 West (AR7W), which extends from Hamilton Bank

on the Labrador shelf to Cape Desolation on the Greenland shelf (Figure 2). It has been occupied annually, typically in May, allowing for a determination of LSW vertical structure at the end of each winter. To compare with the model LSW properties, I use the hydrographic data collected from 1992 to 2004 (Carbon Dioxide International Analysis Center, 2015).

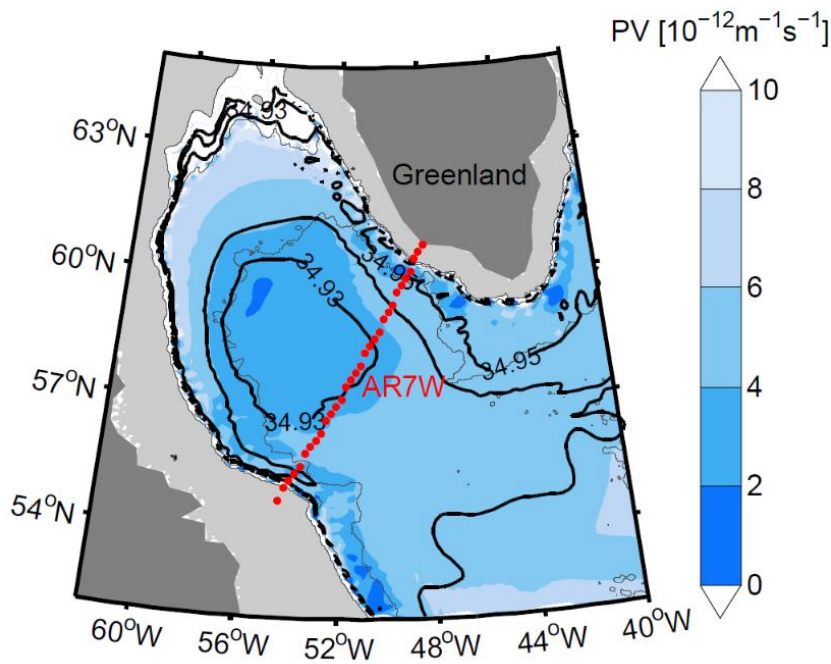

Figure 2: Climatological PV in LSW layer from ORCA025. The LSW layer is between 700m and 1500m. Climatological salinity over LSW layer is contoured in black. AR7W is designated with red dots. Bathymetry shallower than 700m is shaded gray. 1500m and 3000m isobaths are contoured in gray.

2.2.2 ORCA025 model

To conduct this study, I use ORCA025, a global ocean/sea ice model implemented on a quasi-isotropic ORCA grid (a tri-polar grid) at eddy-permitting resolution (1/4°) under the framework of DRAKKAR, a European modelling project

(Bernard, et al., 2006; The DRAKKAR Group, 2007). As described by Bernard et al., 2006 and The DRAKKAR group (2007), the configuration of ORCA025, which has 1442×1021 grid points and 46 vertical layers, is based on the NEMO (Nucleus for European Modeling of the Ocean) system. Vertical grid spacing increases from 6m near the surface to 250m at the bottom. Horizontal resolution increases with latitude, with the coarsest resolution, 27.75 km at the equator. The model uses 2-minute resolution Etopo2 bathymetry from the National Geophysical Data Center and initial conditions are set with a combination of temperature and salinity data derived from Levitus et al. (1998), the PHC2.1 climatology (Steele, et al., 2001) and the Medatlas climatology (Jourdan, et al., 1998).

As reported by Bernard et al. (2006), the climatological daily mean wind stress vector, derived from ERS Scatterometer data (CERSAT, 2002) and NCEP/NCAR reanalysis (Kalnay, et al., 1996) is used to provide the surface momentum flux. An empirical bulk parameterization (Goosse, 1997) is used to compute the surface heat fluxes and freshwater fluxes, with data of climatological daily mean air temperatures are from NCEP/NCAR reanalysis; climatological monthly mean precipitation from CMAP (Xie & Arkin, 1997); monthly mean humidity (Trenberth, et al., 1989), cloud cover (Berliand & Strokina, 1980) and climatological daily mean wind speed from the blend of ERS and NCEP/NCAR reanalysis.

The 5-day model output used in this study is from the model run forced with the global hindcast dataset from 1961 to 2004. Lagrangian trajectories produced from this model output have been shown to reproduce realistic signatures of the deep recirculation gyres in the North Atlantic (Gary, et al., 2011). Gary et al. (2012) also demonstrate that ORCA025 accurately reproduces the distribution of CFC-11 tracers at LSW depths in the North Atlantic. As will be shown in section 2.4, ORCA025 can reproduce the LSW spreading pattern depicted by RAFOS floats. Additionally, the modeled LSW volume transport at 53°N of -11.9 ± 0.9 Sv compares favorably with the observed transport of -11.3 ± 1.0 Sv based on shipboard LADCP measurements (Fischer, et al., 2010). Therefore, ORCA025 is considered highly suitable for the purposes of this study.

2.2.3 Observation and model comparison of LSW properties

To ascertain the ability of the model to capture the variability of LSW properties in the Labrador Sea, the model's temperature, salinity and density fields at LSW depths (between 700m and 1500m) along AR7W are compared to observations, using only model data contemporaneous with the observed data. As seen in Figure 3, the model's long-term trends and interannual variability compare favorably with those from observations: the decadal trend for observed and modeled temperatures are 0.05 °C/year and 0.03 °C/year, respectively, and after detrending the time series, the standard deviations (SD) are 0.04 °C and 0.05 °C respectively; for salinity, the trends between

observations and the model are 0.0009 per year and 0.0003 per year, with the SD of 0.006 psu for the former and 0.006 psu for the latter after detrending; for density, the trend is -0.004 (kg/m^3)/year for observations and -0.003 (kg/m^3)/year for the model. After detrending, the SD for density is 0.006 kg/m^3 and 0.004 kg/m^3 for the observations and the model, respectively.

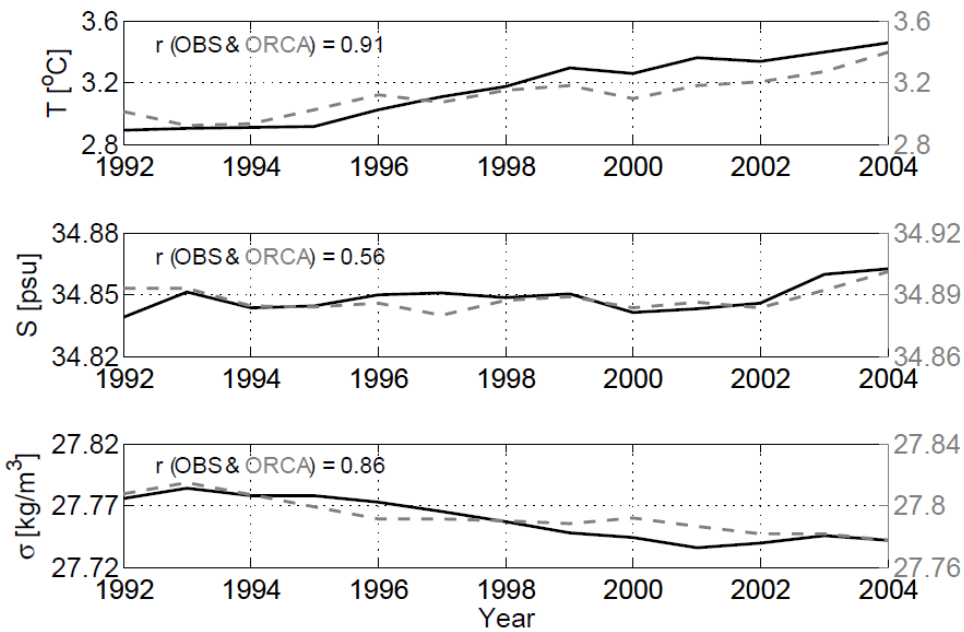

Figure 3: Comparison between observed and modeled time series along AR7W. Time series from observations are plotted in black solid and those from ORCA025 are shown in dashed gray. The plotted time series of temperature (upper), salinity (middle) and density (lower) are averaged between 700m and 1500m. Note that the modeled salinity is slightly higher than observed, and thus the modeled LSW is slightly denser.

2.2.4 Definition of LSW

I use both PV and density to identify LSW in the model. Assuming that relative vorticity is small compared to planetary vorticity, PV can be approximated as:

$$PV = f\frac{N^2}{g} \quad (1)$$

where f is the Coriolis parameter, g is the gravitational constant and N^2 is the Brunt–Väisälä frequency, which is defined as $-\frac{g}{\rho}\frac{d\rho}{dz}$ (Talley & McCartney, 1982), where ρ is density. Thus, PV will be small for a water mass that is weakly stratified in the vertical. In this study, LSW is defined as the water mass in the density range [27.75, 27.84] kg/m^3 with PV < 4×10^{-12} $m^{-1}s^{-1}$, which is the same threshold used by Talley and McCartney (1982). These density limits for LSW differ slightly from those typically used for observed classical LSW ([27.74, 27.80] kg/m^3) (Stramma, et al., 2004) because LSW in the ORCA025 model is saltier and thus denser than that observed (Figure 3).

2.2.5 Trajectory computation and launch configuration

Synthetic floats were launched along a section in the model that replicates AR7W. All launches were dynamic: floats were launched from each grid along AR7W only when properties in a particular grid meet the established water mass criteria, given above as PV < 4×10^{-12} $m^{-1}s^{-1}$ and density within [27.75, 27.84] kg/m^3 (Figure 4). A year-to-year comparison of the number of floats launched in newly-formed LSW along AR7W with the total number of floats launched in newly-formed LSW in the entire Labrador Sea yields a correlation coefficient of 0.93. Therefore, the number of floats launched along AR7W for any 5-day period can be used as a proxy for the amount of LSW present for that same period.

Though floats are launched every five days from 1961 to 2004, only one launch is selected each year for the calculation of trajectories. Since the interest is in the export of newly-formed LSW following its wintertime production, I choose the launch for which the float number is maximized. As such, float integration for each year begins from the 5-day period when the water mass volume has reached its maximum for that winter. It is noted that convection during one winter may reach the depth of fossil LSW, i.e., LSW formed the previous year or years. In this case, the fossil LSW would be considered part of the newly-formed LSW as long as it shares the low PV signature.

For each launch site, float trajectories were calculated from the model's 3-dimensional velocity field using ARIANE, a Fortran code for trajectory computation (Blanke & Grima, 2010). All float trajectories were integrated for 40 years and for those launched after 1964, velocity fields were recycled with a single discontinuity between December 31st, 2004 and January 1st, 1961. This method has been successfully used in previous studies (Gary, et al., 2011; Gary, et al., 2012). The validity of this method is also tested by comparing the trajectories computed from sequential years of data and those computed from data with this discontinuity (not shown). The difference in trajectories between the two is inconsequential to our results.

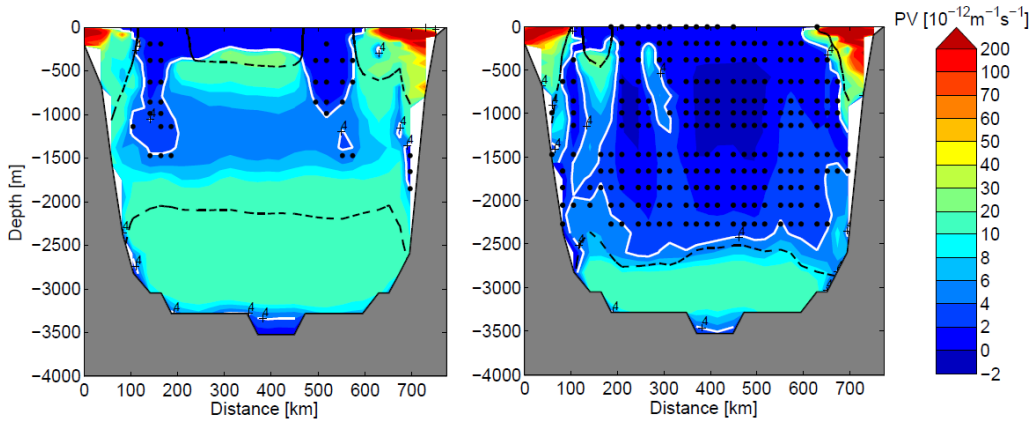

Figure 4: PV along the model's AR7W. The left panel shows PV on March 26th, 1968 and the right shows PV on March 1st, 1990, when the maximum volume of LSW was formed for each year. 75 floats were launched on the former date and 521 on the latter. Black dots indicate float launch positions. White contours denote where PV is smaller than 4×10-12 $m^{-1}s^{-1}$ and black dashed lines indicate where density is between 27.75 and 27.84 kg/m^3. To avoid surface intensification of floats induced by decreasing model vertical resolution with depth, floats were released at a fixed vertical interval, 200m, which is the maximum vertical resolution in the upper 2600m of the model.

2.2.6 Definition of inter-gyre boundaries

To quantify export from the subpolar gyre and import into the subtropical gyre, two boundaries are defined, referred to as the inter-gyre boundaries. These boundaries are calculated using the model's surface dynamic height anomaly, ΔD, relative to 1000 m, which is defined as:

$$\Delta D = \int_{p_{1000}}^{p_{sfc}} \left(\alpha_{S,T,P} - \alpha_{35,0,P}\right) dp \qquad (2)$$

where $\alpha_{S,T,P}$ is the in-situ specific volume and $\alpha_{35,0,P}$ is the specific volume of seawater at a standard temperature and salinity. S, T, and P represent in-situ temperature, salinity and pressure, respectively (Knauss, 1997). ΔD is computed for each grid in the basin

domain at each time step and then averaged over all 44 years to produce a mean value, $\overline{\Delta D}$, at each grid. I choose the $\overline{\Delta D}$ contour of 9 $m^2 s^{-2}$ as the subpolar boundary, north of which is considered to be the subpolar region, and the $\overline{\Delta D}$ contour of 11 $m^2 s^{-2}$ as the subtropical boundary, south of which is the subtropical basin (Figure 5). As will be shown below, some floats that cross the subtropical boundary are carried back to the subpolar basin at one or more times during their 40-year integration. Therefore, another boundary is set in the subtropics, 30°N, from which the floats are not expected to return to the subpolar basin. As shown by previous studies (Bower, et al., 2009) and also shown below, floats that have been exported south of 30°N, are likely to join the southward-flowing DWBC. By 23°N, almost all floats are within the DWBC. For this reason, I also use 23°N as the latitude where LSW is primarily contained within the DWBC.

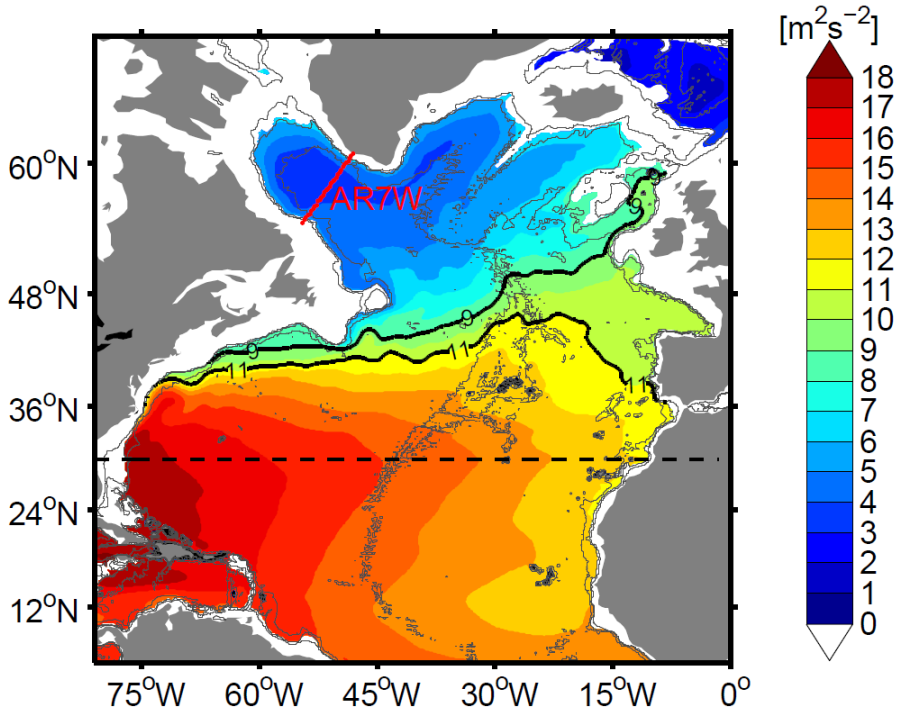

Figure 5: Mean surface dynamic height anomaly ($\overline{\Delta D}$) in the North Atlantic. Black contours (9, 11 m^2s^{-2}) indicate the inter-gyre boundaries. The black dashed line across 30°N serves as another model boundary. 700m, 1500m and 3000m isobaths are contoured in gray.

2.3 Linkage between LSW production and NAO

As mentioned above, I have chosen to quantify the amount of LSW formed each year in the model with the number of floats launched in newly-formed LSW. To ascertain the representativeness of the float number as a proxy for LSW formation, I compare the time series of float number with the LSW thickness in the model (Figure 6). The model LSW thickness is computed as the average depth along AR7W of the water that has PV < 4×10^{-12} $m^{-1}s^{-1}$and density between 27.75 kg/m^3 and 27.84 kg/m^3 on the same day of the float release. The two variables yield a strong correlation (r = 0.91),

leading to the conclusion that the number of floats launched when the maximum amount of newly-formed LSW is present is a good indicator of the interannual variability in LSW thickness, which has been the traditional measure. Actually, the float number provides a more accurate estimate of LSW formation since the number of floats released depends not just on the vertical extent of the newly-formed water, but on its lateral extent as well.

As seen from Figure 6, Labrador Sea convection has strong interannual to interdecadal variability, which has been previously linked to the winter NAO index (Kieke & Yashayaev, 2015; Sarafanov, 2009; van Aken, et al., 2011; Kieke, et al., 2007; Rhein, et al., 2011). A negative NAO winter index has been linked to weaker LSW production from 1960s to 1970s, while a persistent positive NAO from the 1980s to the mid-1990s has resulted in strong convective activity and greater LSW formation. The float number anomaly is correlated with NAO ($r = 0.62$), as is the model's LSW thickness anomaly ($r = 0.66$). Both correlations are significant at 95% confidence level based on a t-test.

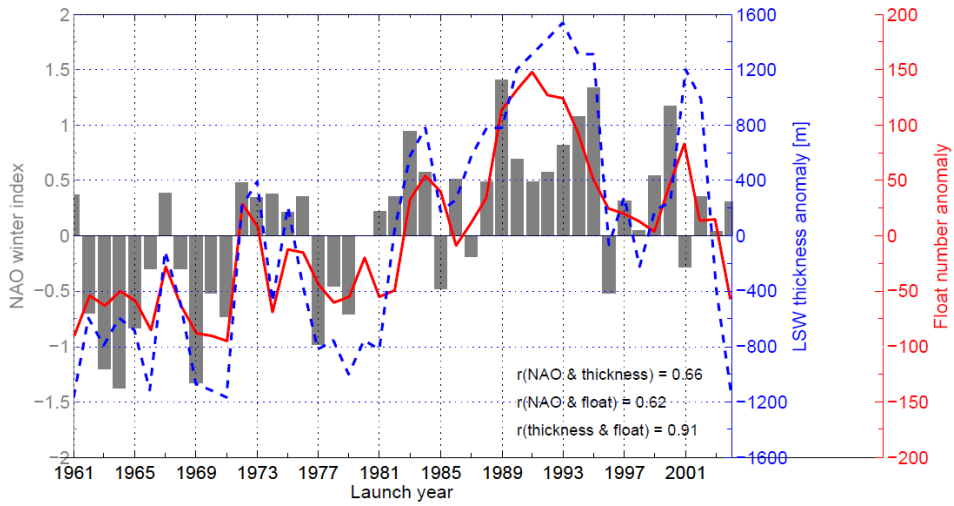

Figure 6: Time series of LSW production and NAO. Interannual variability of float number anomaly (solid red) and LSW thickness anomaly (dashed blue) derived from ORCA025 when the strongest convection takes place each year. The winter NAO index (gray bars) is also shown from 1961 to 2004. The winter NAO index is computed by averaging the monthly NAO index from December to March each year. Data is from the NOAA National Weather Service Climate Prediction Center (2015).

2.4 Spreading pathways of newly-formed LSW

Bower et al. (2009) have shown the 2-year spreading pathways of RAFOS floats launched in the DWBC at 50°N every 3 months from 2003 to 2005. To verify that ORCA025 can accurately reproduce this pattern, test floats were launched within the model with a similar observational design, namely model floats were launched at 50°N at 700m and 1500m every 3 months from 1961 to 2004 and then integrated forward for two years. An example of the float trajectories within 2 years is shown in Figure 7. Of the floats launched over many releases, 27 ± 6% were able to reach the southern tip of Grand Banks (43°N), with 7 ± 6% following the DWBC continuously. The majority of floats (73 ± 6%) drifted eastward and northeastward within the subpolar gyre, which compares

favorably to the observed percentage (70%; 28/40) of RAFOS floats that took this route (Bower et al., 2009). Thus, based on this comparison the model is considered capable of approximating the spreading pathways of LSW.

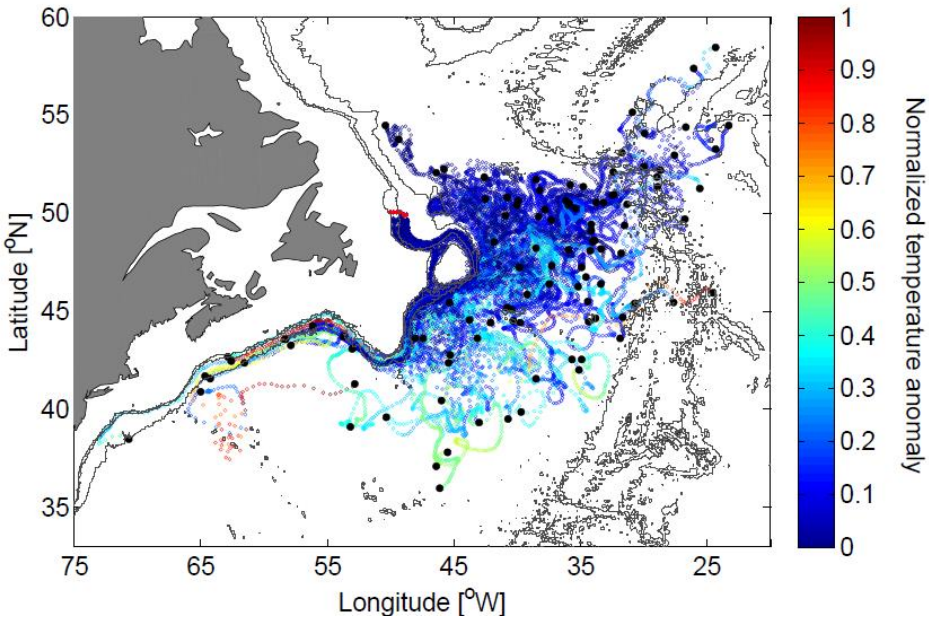

Figure 7: Simulated LSW spreading pathways from DWBC. Test float trajectories launched across 50°N at LSW depths in years from 2000 to 2002 with 2-year lifetime. Initial launch locations for all 108 floats (72 at 700m and 36 at 1500m) at 50°N are shown in red and the final positions are indicated with black dots. Colors represent the normalized temperature anomaly (°C) along the path of each float, computed following Bower et al. (2009): $(T - T_i)/\delta T_{max}$, where T_i is each float's initial temperature, and δT_{max} is the maximum temperature difference, 3°C for floats launched at 700m and 0.72°C for those launched at 1500m. 700m, 1500m, 3000m isobaths are contoured in gray.

To describe the pathways of the simulated float trajectories after the AR7W launch, floats are placed in four categories: (1) never exported – these floats circulated solely within the subpolar basin during their entire lifetime and did not cross either

inter-gyre boundary; (2) recirculated – these floats crossed the subtropical boundary once or more, but they recirculated back and ended their mission in the subpolar gyre; (3) exported – these floats crossed the subtropical boundary and at the end of their mission were in the subtropical gyre. This category includes those that crossed only once during their lifetime, i.e., they never returned to the subpolar gyre, and those that were repeatedly exported – these floats crossed the inter-gyre boundaries several times before they ended their mission in the subtropical basin; (4) in-between – these floats ended their mission located between the subpolar and subtropical boundaries.

An example of the spatial distribution of each trajectory category is revealed by a probability map (Figure 8) constructed from pathway positions for 40 years after the AR7W launch in 1990. Probability maps from other launch years yield qualitatively the same maps. In general, floats are confined north of 30°N during the 40 years of integration. At the end of those 40 years, 31% of them reside in the subpolar gyre: 17% circulated in the subpolar basin the entire time, while 14% returned to the subpolar basin after one or more exports to the subtropical gyre. Only 46% of the floats ended up in the subtropical gyre 40 years after launch, of which 7% crossed the inter-gyre boundaries only once and 17% ended up south of 30°N. The floats that reached the subtropical gyre did so by a number of pathways, including those in the central and eastern North Atlantic basin. The central basin pathways were described previously by recent studies focused on interior pathways (Bower, et al., 2009; Lozier, et al., 2013) of

the subpolar to subtropical export. The eastern basin pathway is along the eastern flank of the RR, in agreement with prior observational studies (Kieke, et al., 2009; Rhein, et al., 2015). This pathway is similar to the southward pathway of ISOW revealed from both observational and modeling studies (Lankhorst & Zenk, 2006; Xu, et al., 2010).

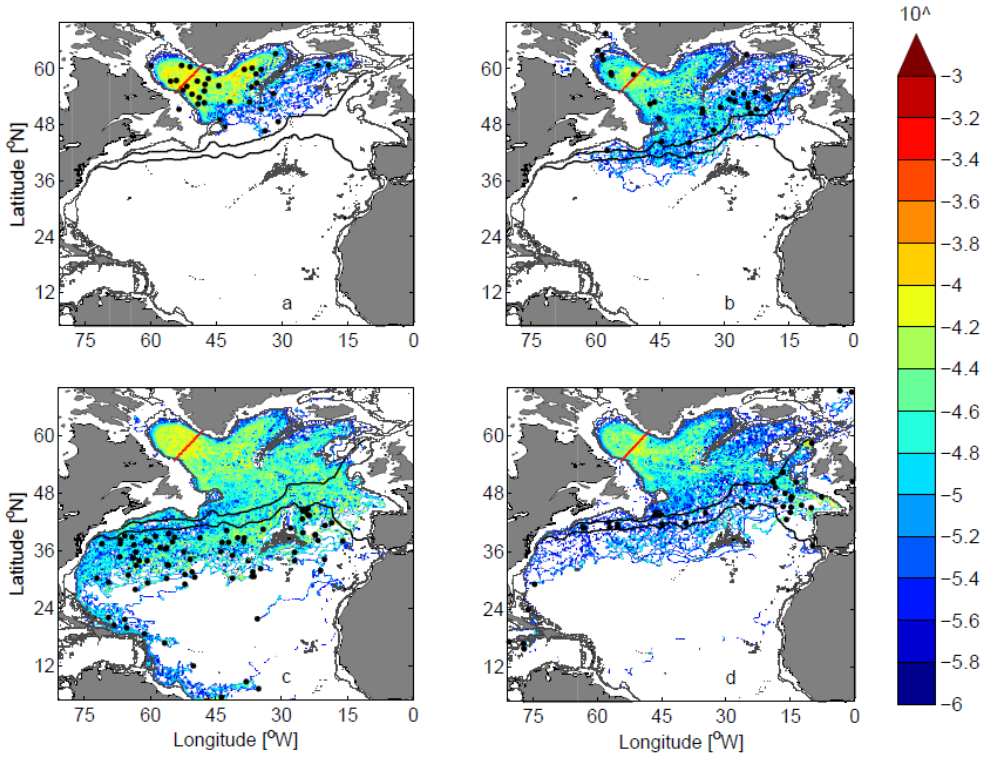

Figure 8: Simulated LSW spreading pathways from the Labrador Sea. Probability maps of trajectories 40 years after launch on March 1st, 1990: (a) never exported floats (17% of total); (b) recirculated floats (15%); (c) exported floats (42%); (d) in-between floats (26%). The probability map is created by first dividing the North Atlantic into 0.25°×0.25° grids, counting the number of times floats pass through each grid (including repetitions), and then dividing the number of passes in each grid by the total float passes over all grids (Gary, et al., 2012). Black solid lines represent the inter-gyre boundaries. Black dots indicate final float positions. 700m, 1500m isobaths are contoured in gray.

Repeating the above analysis for all 44 launches (1961-2004) reveals that there is relatively little variability over time (Figure 9): on average, 34% of the total floats stayed within the subpolar basin 40 years after launch; 46% were able to reach the subtropics; and 20% stayed between the two boundaries. Despite the significant change in the number of floats launched each year, the fractions remain relatively constant (±7%) except for the years 1961, 1969 and 1971, when fewer than 10 floats were launched along AR7W, a paucity that indicates weak convective activity in the Labrador Sea during those years. These floats are too few to draw conclusions on their preferred pathways, but given the pathways from the other years, there is not much variability in LSW spreading pathways.

The decrease (increase) in the percentage of floats in the subpolar (subtropical) gyre persists over the full 40 years, an indication of the long residence time for LSW in the subpolar basin. The percentage of floats between boundaries, however, remains relatively constant after 25 years, indicating a smaller residence time scale for this region.

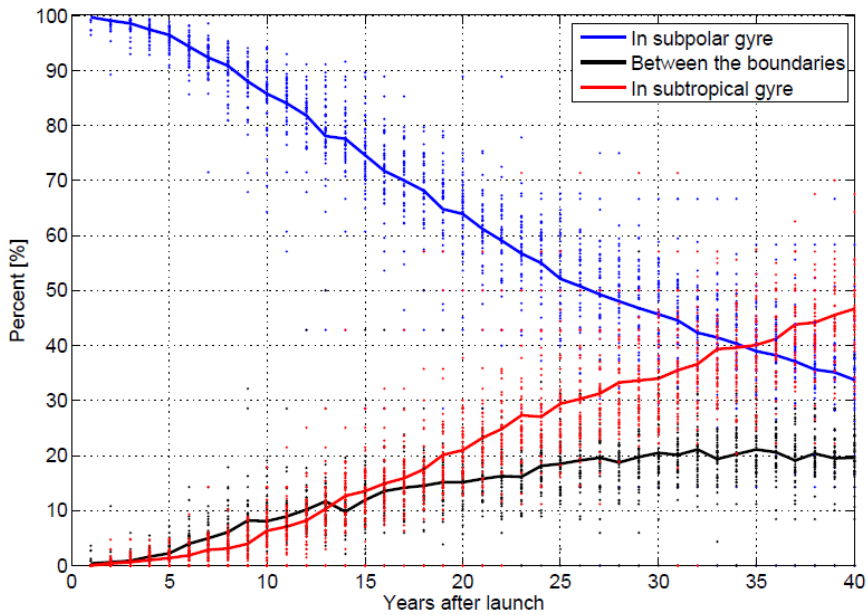

Figure 9: Percentage of LSW distribution. The percentage of floats in the subpolar gyre (blue), subtropical gyre (red) and in the area bounded by the inter-gyre boundaries (black) as a function of time after the launch across AR7W. The solid curves designate the percentage averaged over all 44 releases while the colored dots represent the percentages for each release.

2.5 The age of exported LSW

So far, it is shown that only 46% of the floats launched along AR7W end up in the subtropical gyre after 40 years, which indicates a long advective time scale for LSW to reach the subtropical gyre. A calculation and mapping of LSW age confirms this expectation (Figure 10, left panel). The youngest LSW is found in the Labrador and Irminger Seas, as well as along the deep western boundary current, through which floats reach the subtropical gyre within 15 years (the fastest float took less than 3 year). The average age of floats at the inter-gyre boundary region is 22 ± 10 years, which is also evident in the cross-sectional plot of age along AR7W in Figure 10 (right). As discussed

above, the majority of the floats launched in the central basin along AR7W took 20 years on average to first cross the subtropical boundary. However, floats launched in the DWBC, which account for less than 5% of the total launched, took less than 15 years to be exported to the subtropical gyre.

At 30°N, where floats are less likely to recirculate back to the subpolar gyre, the age is 30 ± 8 years. The age distribution along AR7W of the floats that reach 30°N is similar to that shown in Figure 10 (right), but with greater ages. The spatial distribution of LSW age shown in Figure 10 (left) is consistent with the age of simulated LSW from Gary et al. (2012). Using a CFC observational data set, Rhein et al. (2015) show a similar LSW age distribution: their youngest waters are in the Labrador and Irminger Seas; age increases eastward from south of the Grand Banks to the Rockall Trough near the inter-gyre boundary region; and age in the western subtropical gyre increases steadily to the south. In Rhein et al. (2015), the age of young LSW (age < 40 years) is 16 years when it crosses the inter-gyre boundary and 22-24 years at 30°N. Both of these ages fall in the range derived from Lagrangian floats in this study.

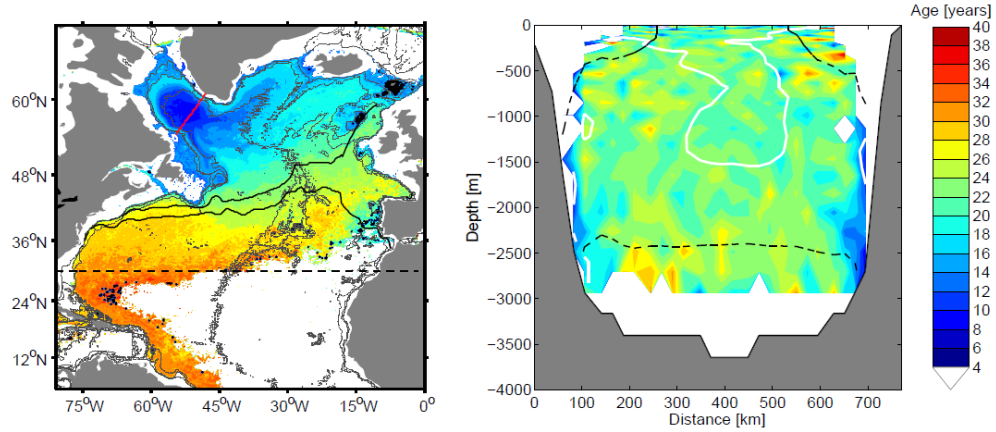

Figure 10: Age of LSW. (Left) Average age of floats for 44 releases of 40 years: the whole domain is divided into 0.25° by 0.25° grids and the age for each grid is computed by averaging the time elapsed since launch for each particle. Repeated visits by the same float to the same grid are included in the age calculation. To avoid biasing the average, only when the box has more than 100 float occurrences is the mean age computed. The black solid lines indicate the subpolar boundary (north) and the subtropical boundary (south); the black dashed line indicates 30°N. Initial launch locations are shown in red. 700m, 1500m, and 3000m isobaths are shown in gray. (Right) The average age of all floats from 44 releases that cross the subtropical boundary in 40 years as a function of initial position along AR7W. Black dashed contours show where climatological density is between [27.75 27.84] kg/m^3; white contours show the area with PV smaller than 4×10^{-12} $m^{-1}s^{-1}$.

Considering the long residence time for LSW in the subpolar basin, the volume export at the subtropical boundary or at 30°N for any particular year is expected to be comprised of waters with many different ages. The results in Figure 11 confirm this expectation. In 2003, floats exported across the subtropical boundary, as well as floats arriving at 30°N, are of various ages and, importantly, there is no distinguishable difference in the number of floats from one age to the next even though the number of the floats launched varies significantly with time. Also, the number of floats from any given launch year that contributes to the 2003 export is quite small (~2%) compared to

the number of floats launched each year, which, as discussed above, is a measure of the convective strength in the Labrador Sea. Similar results are observed in other years' export. In the Eulerian frame, the vertical diapycnal mass flux in the Labrador Sea has been estimated to be ~2 Sv (Pickart & Spall, 2007), thus the contribution of the transformed water mass to the amount of LSW exported each year is thus 0.04 Sv, a negligible quantity compared to the 11.3 ± 1.0 Sv of LSW within DWBC at 53°N (Fischer, et al., 2010). In other words, from both an Eulerian and Lagrangian perspective, convection strength in the Labrador Sea and newly-formed LSW export are not tightly coupled, as discussed further below.

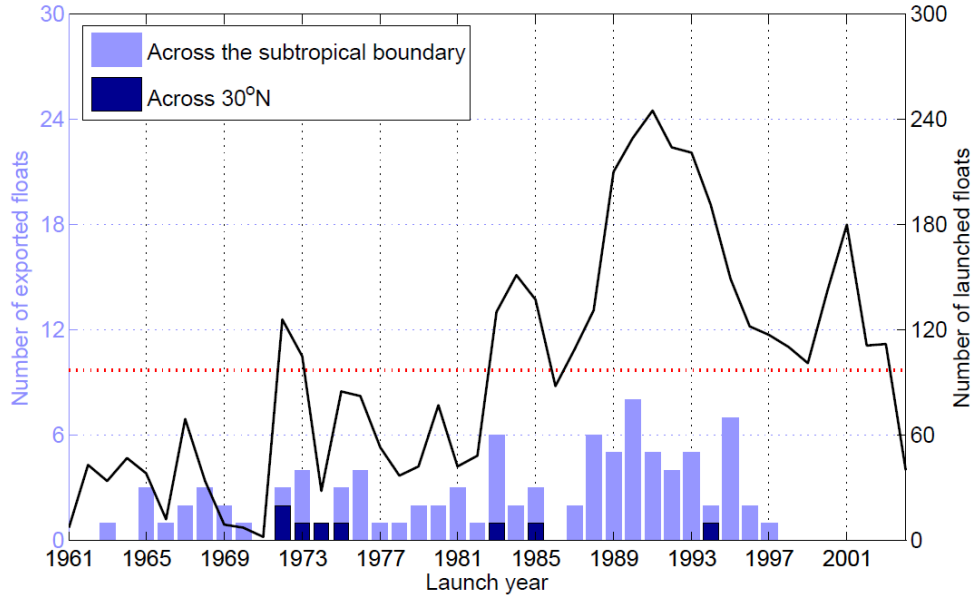

Figure 11: Histogram of exported float number in 2003. The number of floats from each launch year exported south of the subtropical boundary (light blue bars) and 30°N (dark blue bars) in 2003 are plotted. Initial launch number is plotted with a black solid line; its average is denoted by the red dashed line. On average only 2% of

floats released each year along AR7W contribute to the 2003 LSW export across the subtropical boundary.

2.6 Linkage between LSW production and the export of blended LSW

The above analyses make clear that there is no coherent arrival of LSW in the subtropical gyre with the same age. Thus, to further investigate the relationship between LSW production and its export, floats are no longer identified by their launch year in the Labrador Sea. Instead, I seek to understand the relationship between LSW production and the blended LSW export to the subtropical gyre regardless of age. In order to identify the locations of blended LSW near the subtropical boundary, all AR7W launched floats are located when they are crossing the boundary (Figure 12). In Figure 12, floats are concentrated within the area where PV is < 12×10^{-12} $m^{-1}s^{-1}$ and density is between [27.75, 27.84] kg/m^3 west of the Mid-Atlantic Ridge. These property ranges are chosen as the criteria for the new float launches into blended LSW.

Floats were then released on each January 5th north of the subtropical boundary (Figure 13) from 1961 to 2004, and the blended LSW export for each year is the total number of floats that crossed the subtropical boundary by the end of that year. I consider this time series an indication of export variability for blended LSW, rather than LSW linked to water mass formation in a given year. Similar dynamic launches were conducted at 23°N, where southward-moving floats are concentrated within the DWBC and between isopycnals of [27.75, 27.84] kg/m^3 (Figure 14). Again, the time series of

blended LSW export to the south of 23°N is derived from the number of floats that crossed 23°N each year.

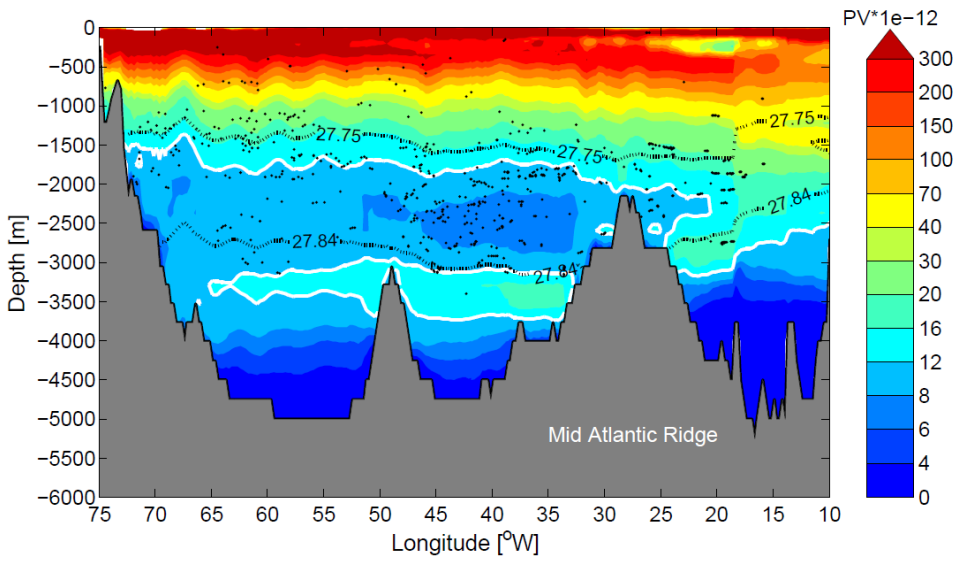

Figure 12: Vertical distribution of LSW across the inter-gyre boundary. Positions of simulated floats launched in the Labrador Sea when they crossed the subtropical boundary in 2003 (black dots), with annually averaged PV ($m^{-1}s^{-1}$) shown in color. White contours outline the area where PV is smaller than 12×10^{-12} $m^{-1}s^{-1}$, and the black dashed line indicates density between [27.75, 27.84] kg/m^3. When they reached the subtropical boundary, over 70% of floats (launched from 1961 to 2002) were located within the area bounded by the two density contours. The PV map and float distributions shown here for 2003 are representative of other years.

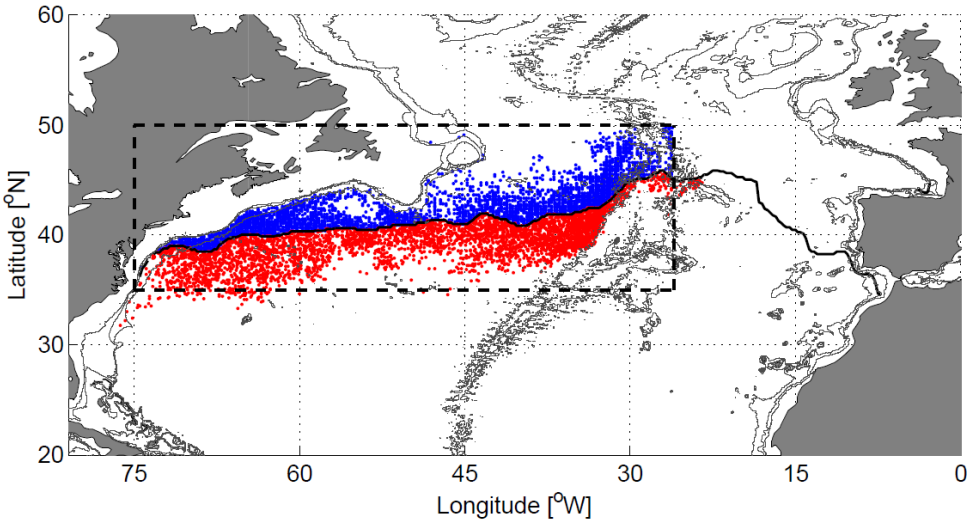

Figure 13: Initial and final positions of blended LSW across inter-gyre boundary in 2003. Floats were launched on January 5th, 2003 with their initial positions shown in blue dots and their final locations in red dots. Only those that were able to reach the subtropical basin within one year are used. One-tenth of the total data points were randomly selected for plotting. Black solid curve indicates the subtropical boundary. The black dashed box (north of the subtropical boundary) indicates the dynamic launch area: longitude [75°W, 26°W], latitude [35°N, 50°N], PV [0, 12×10^{-12}] $m^{-1}s^{-1}$ and density [27.75, 27.84] kg/m^3. Only a few floats launched outside the box made it to the subtropics within a year. This float distribution map differs only slightly from year to year. 700m, 1500m, and 3000m isobaths are contoured in gray.

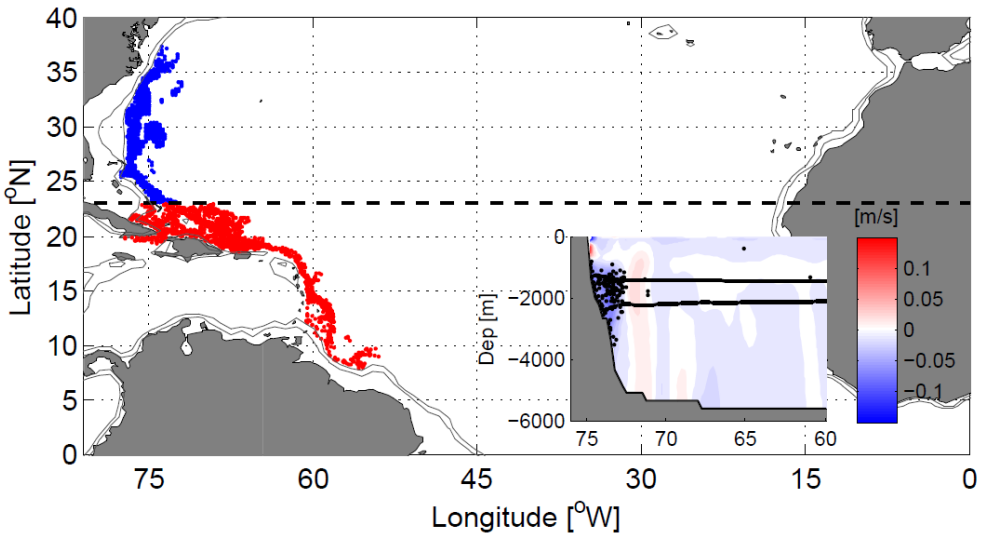

Figure 14: Initial and final positions of blended LSW across 23°N. The inset shows the positions of those AR7W launched floats when crossing 23°N, superposed on the 44-year mean meridional velocity, with black contours outlining the density between [27.75, 27.84] kg/m^3. This distribution sets the criteria for the blended LSW launch north of 23°N (PV at this location is not distinguishable and thus is not used to identify LSW). Again, the float distribution map and velocity field are representative of all other years.

Figure 15 (upper panel) shows the lead/lag correlation coefficients between the convection strength in the Labrador Sea, given by the float number launched each year along AR7W, and the blended LSW export to the subtropical gyre. The coefficient reaches a maximum of 0.63 with the blended LSW export lagging by 3 years, yet after detrending, no significant correlation is observed. A maximum correlation coefficient of 0.55 is found between convection and the export volume across 23°N at 0 lag/lead; a 0.38 coefficient is computed after detrending the two time series, with convection leading the export by 3 years.

Since the advective time scale for floats from AR7W to the subtropical gyre (23°N) is on average 22 (30) years, the high correlations (before detrending) are not considered to result from a causal relationship between convection strength and LSW advective export. Rather, it is suggested that the fast response of blended LSW export to LSW formation results from a boundary density anomaly induced by convection in the Labrador Sea, the signal of which can be propagated southward quickly though boundary waves. This supposition is supported by a modeling study which showed an overall strengthening of the AMOC within 1-2 years after LSW convection (Biastoch, et al., 2008). Also demonstrated in this study is that the AMOC response to convection is primarily on decadal time scales. The fact that there are negligible correlations after detrending (which dampens decadal variability) also validates our assessment that convective variability in the Labrador Sea cannot explain the downstream variability of LSW export through advection.

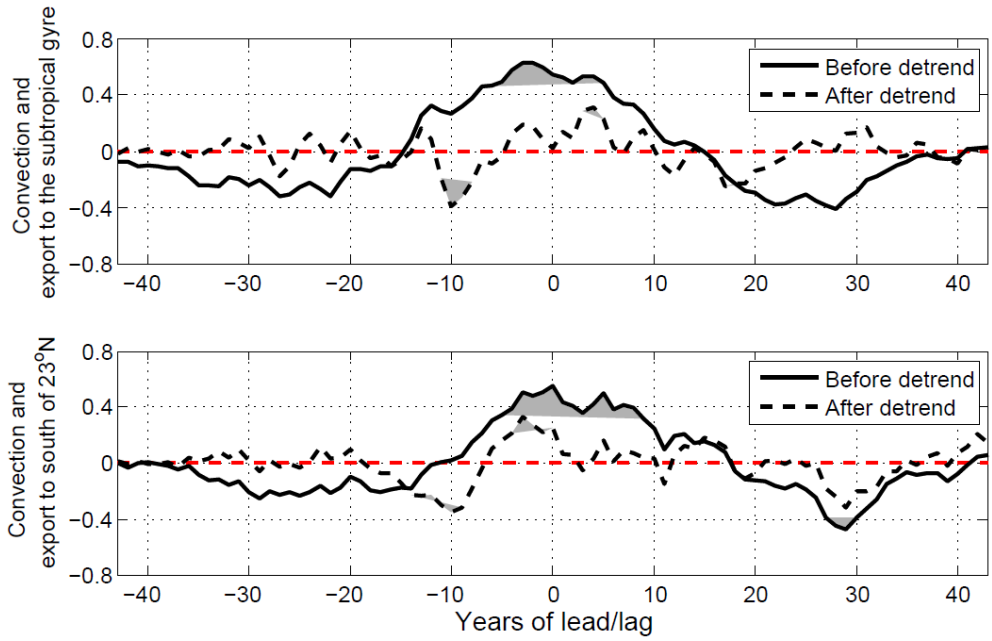

Figure 15: Correlation between LSW production and its export. (Upper) Cross-correlation coefficients as a function of lead/lag for the launched float number anomalies along AR7W and exported float number anomalies across the subtropical boundary. Black solid line indicates the coefficient before detrending and the dashed line indicates the value after detrending. The values at 95% confidence level are shaded with light gray. Negative values along the x-axis indicate that convection is leading export. (Lower) Same as the upper panel, but for the float number anomalies launched and exported number anomalies across 23°N.

2.7 Summary

In this study, I use trajectories of synthetic floats launched in the Labrador Sea in an ocean general circulation model to simulate the spreading pathways of newly-formed LSW. It is shown that only 46 ± 7% of the LSW formed during winter is able to reach the subtropical boundary after 40 years. The rest of the water mass largely recirculates within the subpolar gyre or is resident in the area between the gyre's boundaries. The exported floats primarily enter the subtropics via interior pathways that extend from the

western boundary to the eastern basin of North Atlantic, though not all of those pathways indicate a direct route for export. Some floats that cross into the subtropical gyre recirculate back to the subpolar basin more than once before ending up in the subtropical gyre, which lengthens the average time scale for the floats to be exported. The mean age of floats when they first reach the subtropical boundary is 22 ± 10 years and it takes 30 ± 8 years for them to reach 30°N. The youngest floats, with ages less than 15 years, are those that originate or travel near the western boundary, yet these floats account for less than 5% of the total.

An analysis of the age of LSW when it crosses into the subtropical gyre shows that it is a combination of waters formed years or even decades prior to the year of the crossing. It is shown that floats launched in a particular winter contribute only marginally to future LSW volume exports. Thus, it is concluded that the contribution of particular winter's convection to the total LSW export in any given subsequent year is too small to appreciably impact the volume of that export.

The analysis is extended to include blended LSW export, by which the water mass is defined by its hydrographic properties only, not by its age. No linkage is found between LSW formation and the export of blended LSW across the subtropical boundary or 30°N through advection. Rather, the water mass export in this layer appears to respond to Labrador Sea convection via fast western boundary waves with a time lag of no more than 1-2 years.

The relatively long time for LSW to reach 30°N (30 years on average) stands in contrast to the arrival time of LSW from the Labrador basin to the subtropical gyre based on property correlations: Curry et al. (1998) show a high correlation between LSW thickness and temperature anomalies at 32°N near Bermuda with the former leading by only 6 years, while van Sebille et al. (2011) estimate that LSW reaches 26°N (at Abaco) in 9 years based on classical LSW salinity anomalies. Thus, left unanswered in this study is the question as to how property signals observed in the Labrador Sea are transmitted to the subtropical gyre in such a relatively short time scale, if not through advection. This question forms the basis for an ongoing study that is illustrated in section 5.2.

3. Observed and Modeled Spreading Pathways of ISOW

The spreading of ISOW in the eastern North Atlantic has largely been studied in an Eulerian frame using numerical models or with observations limited to a few locations. No study to date has provided a comprehensive description of the ISOW spreading pathways from both Eulerian and Lagrangian perspectives. In this Chapter, I use a combination of previously unreported current meter data, hydrographic data, RAFOS float data, and a high resolution (1/12°) numerical ocean model to study the spreading pathways of ISOW from both of these perspectives. This chapter has been published in *Progress in Oceanography* (Zou, et al., 2017), and is reproduced here with slight modifications.

3.1 Introduction

ISOW is formed in the Nordic Seas from these identified sources: open-ocean convection in the Greenland Sea, dense water formation along the Arctic shelves and the transformation of Atlantic water (Rudels, et al., 1999; Eldevik, et al., 2009). After formation, ISOW flows to the eastern subpolar gyre mainly through the Faroe-Shetland Channel, with a small portion over the Iceland-Faroe Ridge. ISOW entrains the ambient water as it spreads southward primarily along the slope of the northwest Iceland Basin and then out into the eastern North Atlantic (Fleischmann, et al., 2001; van Aken & Boer, 1995).

An understanding of the distribution and variability of ISOW spreading pathways, together with the other two components of the lower limb of the AMOC, the LSW and DSOW, is fundamental to our understanding of AMOC structure and variability.

Traditionally, the DWBC was considered the major conduit from the subpolar to the subtropical gyre for these deep water masses. As a consequence of this assumption, DWBC transport variability was roughly equated to variability of the deep AMOC limb (Molinari, et al., 1998; Curry, et al., 1998; Schott, et al., 2006). However, recent studies have demonstrated the importance of interior pathways in exporting LSW (Bower, et al., 2009; Lavender, et al., 2005; Gary, et al., 2012) and OW (Xu, et al., 2015; Lozier, et al., 2013; Gary, et al., 2011; Stramma, et al., 2004) to the subtropical gyre in the western North Atlantic, thus calling into question the DWBC as the sole conduit of deep water masses in the North Atlantic. Besides an interior pathway for overflow waters in the western North Atlantic, studies based on models and Lagrangian floats have identified a southward pathway of ISOW along the eastern flank of the Mid-Atlantic Ridge (MAR) (Xu, et al., 2010; Machín, et al., 2006; Lankhorst & Zenk, 2006).

In addition to the southward branch along the eastern flank of the MAR, two other ISOW spreading pathways have also been identified in the eastern North Atlantic: one via gaps in the Reykjanes Ridge (RR) north of the Charlie Gibbs Fracture Zone (CGFZ), and the other via a westward crossing through the CGFZ. The former branch

has been mostly studied with models (Xu, et al., 2010; Chang, et al., 2009), while the latter branch has been studied using both model output (Xu, et al., 2010; Chang, et al., 2009) and current meter measurements (Saunders, 1994; Bower & Furey, 2017). In both cases, the pathways are deduced from Eulerian data.

Though these prior Eulerian studies identified particular ISOW pathways, no study to date has validated these pathways from a Lagrangian perspective, primarily because Lagrangian data has been so limited. Additionally, no previous study has assessed the temporal interplay among the spreading branches. Thus, the goals of this study are to: 1) provide a comprehensive description of the ISOW spreading pathways in a combined Eulerian and Lagrangian frame; 2) shed light on the interplay between spreading pathways on interannual time scales.

3.2 Prior knowledge on ISOW pathways and transports

ISOW enters the eastern subpolar North Atlantic between Iceland and Scotland primarily through the Faroe-Shetland Channel (FSC) (Hansen & Østerhus, 2007) and a minor part over the Iceland-Faroe Ridge (Beaird, et al., 2013) (Figure 16). After flowing through the FSC, one ISOW branch flows into the Iceland Basin through the Faroe Bank Channel (FBC), filling the bottom layer (density ≥ 27.80 kg/m^3 with a depth range from 1300m to the bottom) on the Icelandic Slope (Saunders, 1996; Kanzow & Zenk., 2014; Xu, et al., 2010). Another branch travels southward into the Rockall Trough across the Wyville-Thomson Ridge (WTR) (Chang, et al., 2009; Ellett & Roberts, 1973; Sherwin &

Turrell, 2005). A small branch flows southward west of the Maury Channel (Chang, et al., 2009; Xu, et al., 2010). As ISOW spreads southward and westward, it mixes with lighter intermediate waters, such as LSW from the western subpolar gyre, and Lower Deep Water (LDW) from the south (van Aken, 1995; McCartney, 1992).

Direct measurements of the transport in the ISOW layer are available at limited locations (labeled in magenta in Figure 16). The FBC overflow is measured to be 2.1-2.2 Sv (1 Sv = $10^6\ m^3/s$) (Hansen & Østerhus, 2007; Hansen, et al., 2016) and the overflow over the IFR is estimated to be > 0.8 Sv (Beaird, et al., 2013). A southward transport of 3.2-3.8 Sv is observed in the ISOW layer along the northwestern slope of the basin south of Iceland (Saunders, 1996; Kanzow & Zenk., 2014). A transport of 0.1-3.0 Sv with large uncertainties through the Rockall Trough is estimated by Dickson and Brown (1994), while a more recent study shows that the transport across the WTR is at the lower bound of the range (Sherwin, et al., 2008). A westward transport of waters in the ISOW layer across the CGFZ, measured with mooring arrays, is 1.7-2.4 Sv (Saunders, 1994; Bower & Furey, 2017). However, this branch is highly variable due to the frequent approach of the eastward-flowing NAC (Schott, et al., 1999; Bower & Furey, 2017), whose deep flow field interacts with the westward transport of ISOW. The transport of waters denser than 27.80 kg/m^3 in the southward branch along the eastern MAR flank from the Iceland Basin to the West European Basin (WEB) has been estimated to be 2.4-3.5 Sv from tracer data (Fleischmann, et al., 2001).

In addition to the Eulerian-based studies, past Lagrangian studies have also investigated the spreading of intermediate and deep waters in the Iceland Basin. With passive neutrally buoyant RAFOS floats (released between 1419 to 2866 dbar), Lankhorst and Zenk (2006) identify three major pathways of LSW in the Iceland Basin: westward escape into the Irminger Sea through the Bight Fracture Zone (BFZ) along the RR (see also Bower et al., 2002); eastward flow across the CGFZ, which is the major exchange gateway of LSW between the Irminger Sea and the Iceland Basin; and a southward spreading along the eastern flank of the MAR (see also Machín et al., 2006). Though these pathways are mostly identified in the LSW layer, which is shallower than the ISOW layer, the pathways across the RR gaps and along the eastern flank of the MAR are similar to those observed in the ISOW layer (as detailed below), indicating a barotropic structure for the spreading of intermediate and deep waters.

A number of modeling studies have also estimated the volume transport of different ISOW branches (labeled in magenta with parentheses in Figure 16). For example, Xu et al. (2010) estimate that the total transport of ISOW along the northwestern slope south of Iceland is 3.3 Sv. The cross-RR transport in the ISOW layer is estimated to be 1.2 Sv and the westward transport through the CGFZ is 1.9 Sv. Another modeling study (Chang, et al., 2009) also gives the estimate of the ISOW layer transport west of the Maury Channel (1.5 Sv), within the Rockall Trough (2.2 Sv), and

into the WEB (4.6 Sv). Most of these model-based estimates compare fairly well with observational estimates except for the transport estimate into the WEB.

However, to my knowledge, there is to date no observational or modeling study that describes these ISOW branches from a Lagrangian perspective, nor one that investigates the time-varying relationship among the different ISOW branches. The current research aims at filling those gaps and intends to shed light on the similarities and differences between the Eulerian-based and Lagrangian-based studies of ISOW spreading pathways and transports.

3.3 Data and methods

3.3.1 Mooring array and CTD stations in the Iceland Basin

To identify ISOW and its transport cores in the Iceland Basin, I use a mooring array (M1, D1, D2, D3, M2, D4, M3 and M4 in Figure 16) and a set of CTD stations (black dashed line in Figure 16) across the Iceland Basin at 58-59°N. The mooring array and the CTD stations constitute part of the Overturning in the Subpolar North Atlantic Program (OSNAP) - East section, which extends from the southern tip of Greenland to Scotland (Lozier, et al., 2016).

The mooring array was deployed in July 2014 across the entire Iceland Basin at depths between 699m and 2830m. Here I use the mean velocity and property profiles at depths ≥ 1000m from the first year of measurements to study the ISOW transport. On the same cruise, CTD measurements were conducted across the OSNAP section. CTD data

at depths ≥ 1000m along the eastern flank of the RR, where the ISOW major branch is located, is also used in this study.

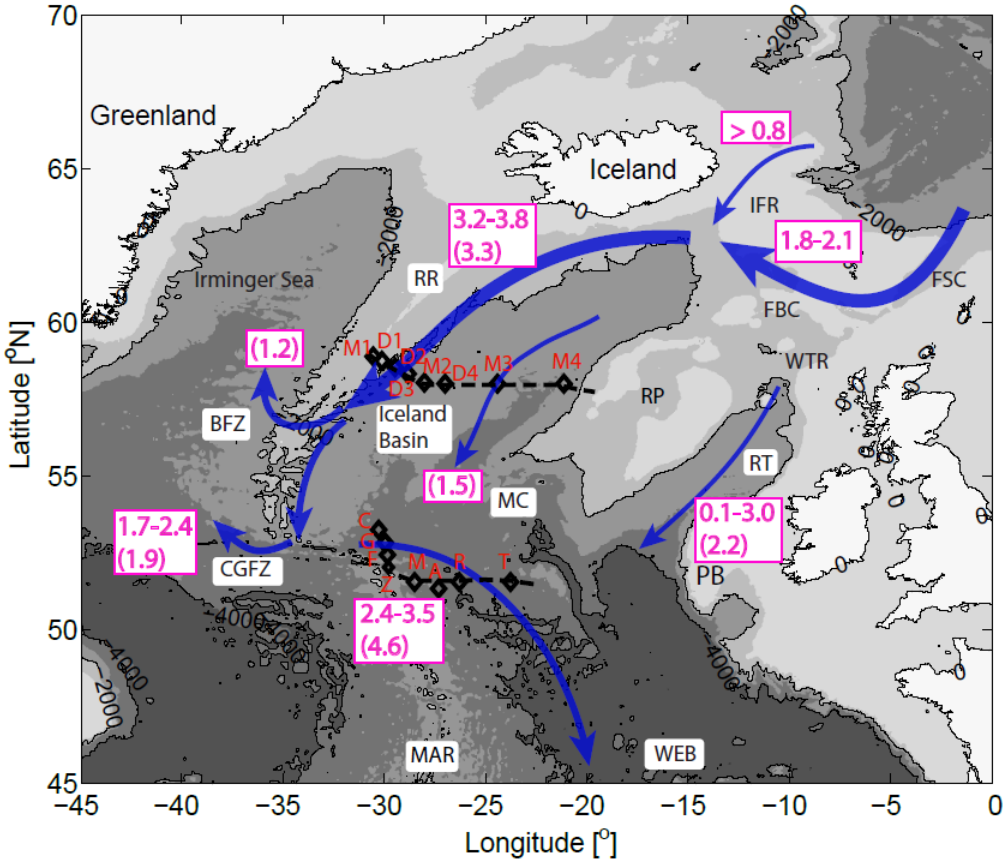

Figure 16: A schematic of the major ISOW spreading pathways. Black diamonds and dashed lines indicate the location of the moorings and CTD sections used in this study. Volume transports (unit: Sv) from previous Eulerian studies are labeled in magenta with those from models enclosed with parentheses. Abbreviations are: Iceland Faroe Ridge (IFR); Faroe-Shetland Channel (FSC); Faroe Bank Channel (FBC); Reykjanes Ridge (RR); Wyville-Thomson Ridge (WTR); Rockall Trough (RT); Rockall Plateau (RP); Porcupine Bank (PB); Bight Fracture Zone (BFZ); Charlie Gibbs Fracture Zone (CGFZ); Maury Chanel (MC); Mid-Atlantic Ridge (MAR) and West European Basin (WEB). All transport estimates shown here are from studies referenced in section 3.1.

3.3.2 Mooring array and CTD stations east of CGFZ

Another mooring array used in this study is located to the east of the CGFZ. The moorings, labeled C, G, F, Z, M, A, R and T are shown in Figure 16. Moorings C, G, F and Z were deployed on June 25, 1999 and largely recovered on July 1, 2000. Moorings M, A, R and T were deployed on August 9, 1998 and recovered on June 16, 1999. All instruments were deployed at depths between 1650m and 3890m. The data used here is the annual mean velocity field at all instrumental depths. Additionally, CTD profiles conducted on FS METEOR in June 1999, when moorings M, A, R and T were recovered, are also used in this study.

3.3.3 RAFOS floats data

Along the 2014 OSNAP cruise track in the Iceland Basin, acoustically tracked deep Range and Fixing of Sound (RAFOS) floats were released to study the ISOW spreading pathways (Lozier, et al., 2016). In this paper, I use 9 floats that were initiated between 1800dbar and 2400dbar along the eastern flank of the RR. The initial launch locations and the trajectories of these floats can be found in Figure 17-Figure 19. These floats followed isobaric surfaces and had an approximate lifetime of two years.

Gaps in float positions, noted in Figure 18-Figure 19, possibly result from: 1) the blockage of the sound signal by a topographic feature, such as a seamount or bight; 2) the degradation of signal strength due to rough surface conditions; and/or 3) too great of

a distance between the sound source and the float. As shown below, these gaps do not seriously impair our view of the floats' spreading pathways.

3.3.4 FLAME model

The model used in this paper is the eddy-resolving (1/12°) member of the Family of Linked Atlantic Models Experiment (FLAME) (Biastoch, et al., 2008; Böning, et al., 2006). The model uses primitive equations and is spun up from rest with European Center for Medium-Range Weather Forecasts (ECMWF) climatological forcing for 10 years. After spin-up, the model is forced with monthly anomalies of NCEP/NCAR reanalysis data (Kalnay, et al., 1996) superimposed on climatological forcing to create a hindcast dataset from 1990 to 2004. Climatological temperature and salinity are maintained at the open boundaries during the simulation.

The z-coordinate model has 45 levels in the vertical, with spacing increasing from 10m near the surface to 250m in the deep ocean. The domain spans from 18°S to 70°N on a Mercator grid. Data used in this paper are the temperature, salinity and three-dimensional velocity fields from 1990 to 2004, all with a temporal resolution of 3 days.

Several past studies have demonstrated FLAME's ability to reproduce observed property and velocity fields in the North Atlantic (Lozier, et al., 2013; Gary, et al., 2011). Additionally, the spreading pathways of the deep water masses simulated in FLAME are similar to those derived from observed floats (Bower, et al., 2009; Getzlaff, et al., 2006) and the eddy kinetic energy (EKE) fields at 15m in FLAME and from observations

(altimetry and surface drifter velocity fields) show similar structure (Burkholder & Lozier, 2011). As shown below, FLAME is also capable of recreating the volume transport and spreading pathways of ISOW observed by mooring arrays and RAFOS floats. Therefore, in addition to the confidence in the model's ability to reproduce the general characteristics of the North Atlantic circulation, FLAME is considered highly suitable for analyzing ISOW transport pathways.

3.3.5 Simulated float launch configuration and trajectory computation

To compute trajectories, floats are initiated at specific locations defined by latitude, longitude and depth. Since our focus is on ISOW pathways, all floats are initiated in the ISOW layer, which is distinguished from the LSW layer by higher density and salinity. For density, I choose the threshold of 27.80 kg/m^3 in the Iceland Basin for both observations and FLAME, the same threshold applied in previous modeling (Xu, et al., 2010; Chang, et al., 2009) and observational studies (Kanzow & Zenk., 2014). FLAME salinities and densities are larger than observed, so the modeled isopycnal of 27.80 kg/m^3 is shallower than the observed isopycnal (shown below), resulting in a thicker ISOW layer in FLAME. Thus, to better distinguish the modeled ISOW layer, I also apply salinity thresholds in the range of [34.95, 34.98], which compare to observed thresholds in the range of [34.91, 34.94]). The choice of isohalines to define ISOW depends on geographic locations, as well as time period. These choices are subjective and based on

inspection of the salinity and density fields. Only when the float's initial density and salinity are greater than the thresholds is the float released.

From an initial launch position, float trajectories are computed using the three-dimensional velocity in FLAME, as detailed in Gary et al. (2011). To extend the lifetime of floats launched in the last few years of the model duration, the model velocity fields are recycled with a single discontinuity between December 31, 2004 and January 1, 1990, so that velocity fields on January 1, 2005 and onward are the same as January 1, 1990 and onward.

3.4 Spreading pathways of ISOW in the eastern North Atlantic

3.4.1 Escape of ISOW through gaps in RR

To trace ISOW spreading pathways, I use observed and simulated floats initiated in the ISOW layer along the OSNAP section (58-59°N). Figure 17 shows the cross-sectional salinity based on CTD stations in July 2014 (left panel) and the salinity across 58°N in FLAME averaged between 1990 and 2004 (right panel). Both observations and model output show the ISOW layer attached to the ridge, with fresh LSW occupying the interior basin at intermediate depths. The initial launch locations of the 9 RAFOS floats are shown as colored circles in Figure 17 (left). To illustrate the different ISOW pathways, the RAFOS floats are divided into two subsets: one subset of floats was initiated at pressures of ~1800dbar (red circles) and the other was initiated at pressures

greater than 2000dbar (blue circles). In this section, the focus is on the first subset of the shallower floats.

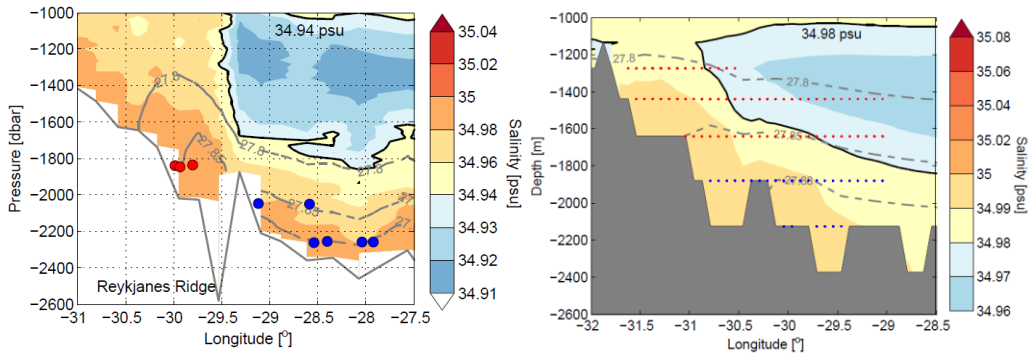

Figure 17: Initial launch locations for observed and simulated floats. (Left) Observed salinity in July 2014 across the OSNAP section (58-59°N, black dashed line in Figure 16) along the eastern flank of the RR. The initial launch locations of the 9 RAFOS floats are plotted as colored circles (red and blue). Isohaline is shown in solid black and isopycnals are contoured as dashed gray lines. (Right) Modeled salinity averaged from 1990 to 2004 across 58°N. Dots in the right panel show the initial launch locations of simulated floats. All floats were initiated in the ISOW layer defined by the property field at launch, which is different from the 15-year mean shown in this panel. Therefore, though some dots appear in the fresh LSW layer, they were in ISOW when they were initiated. Note that the salinity color scale is different between the two panels.

Trajectories of the three shallower RAFOS floats are shown as black curves in Figure 18. Two of them escape into the Irminger Sea through the gaps in RR: one through the BFZ and one through an un-named gap further south. The remaining float continues southward until the latitude of CGFZ.

Considering that RAFOS floats are limited in number, I turn to simulated floats to further illustrate this escape branch. Simulated floats were released in the shallower ISOW layer (< 1800m) along the RR eastern flank at 58°N every 3 months from 1990 to

2002 (red dots in Figure 17, right), and integrated forward by two years. The probability map of the two-year float trajectories is shown in Figure 18. The simulated pathways of the shallower ISOW are well aligned with those from RAFOS floats: a sizable number of floats escape to the Irminger Sea through BFZ and other gaps in the RR; the remaining floats primarily continue southward to the latitude of CGFZ.

In summary, based on observed and simulated float trajectories, the relatively shallow ISOW along the eastern RR flank can escape into the Irminger Sea through RR gaps before reaching the CGFZ, as previously noted in Eulerian modeling studies (Xu, et al., 2010; Chang, et al., 2009). This pathway is also shared by LSW, as illustrated with RAFOS floats studied by Lankhorst and Zenk (2006). A quantification of this pathway is addressed in section 3.5-3.6.

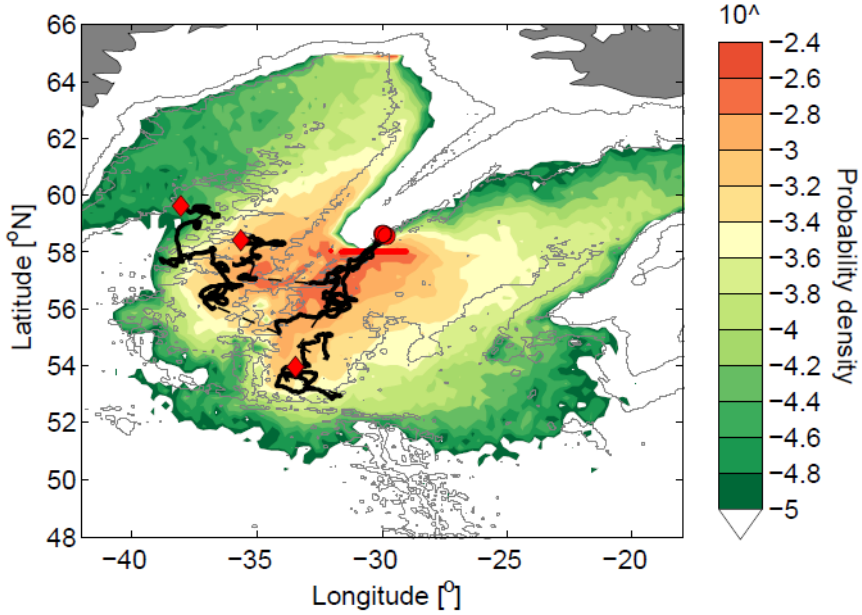

Figure 18: Pathways of shallow ISOW from RR eastern flank. Two-year trajectories of three RAFOS floats are plotted in thick black curves with their initial (final) locations shown as red circles (diamonds). The thin dashed lines connect the gaps where float positions are missing. Probability map of simulated trajectories of shallow ISOW is shaded in color underneath the RAFOS trajectories. Floats were released at 58°N every three months from 1990 to 2002 and were integrated forward by two years. The probability is computed by dividing the North Atlantic into 0.25°×0.25° grids, counting the number of times floats pass through each grid (including repetitions), and then dividing the number of passes in each grid by the total float passes over all grids (Gary, et al., 2012; Zou & Lozier, 2016). The probabilities shown here are on a log scale. 4234 simulated floats were launched along the red short line (also shown in Figure 17, right). 1000m, 2000m and 3000m isobaths are contoured in light gray.

3.4.2 Westward spreading of ISOW through CGFZ

The second subset of RAFOS floats (6 in total) released at greater depths (blue circles in Figure 17, left) reveals a different spreading pathway. Instead of crossing the RR gaps into the Irminger Sea, all 6 floats move southward along the eastern RR flank. Essentially, these floats are too deep to cross the RR gaps, such as the BFZ (~2030m).

Along this southward route, two of the floats turn eastward into the basin interior (Figure 19). The remaining 4 floats continue moving southward, with three reaching the CGFZ. Interestingly, after reaching the CGFZ, two floats immediately turn southward along the western flank of the MAR and one float travels westward. None of the floats show northward spreading along the western RR boundary. This interesting feature is under investigation in a related, but separate study (A. Bower, personal communication).

Again, I turn to modeled floats for a more complete illustration. The launch strategy is similar to that in section 3.4.1, except that the floats were released at greater depths (> 1800m) (blue dots in Figure 17, right). Figure 19 shows the probability map of the simulated deep ISOW spreading pathways within two years. While a small amount escapes through the RR gaps, the majority of the simulated deep ISOW follows similar pathways observed by RAFOS floats. It first flows southward and then either turns into the basin interior or continues southward to the latitude of CGFZ, where westward crossing and southward spreading along the western MAR are both seen. A primary difference is that the modeled trajectories reveal a weak southward spreading of ISOW into the WEB, which is not observed by RAFOS floats. One possible reason for this difference is that the RAFOS floats are too few in number to have sampled this branch. Another reason is that, as will be shown in the next section, the primary origin of waters

within this southward branch is the interior and eastern portion of the Iceland Basin, yet the RAFOS floats were released along the western part of the basin.

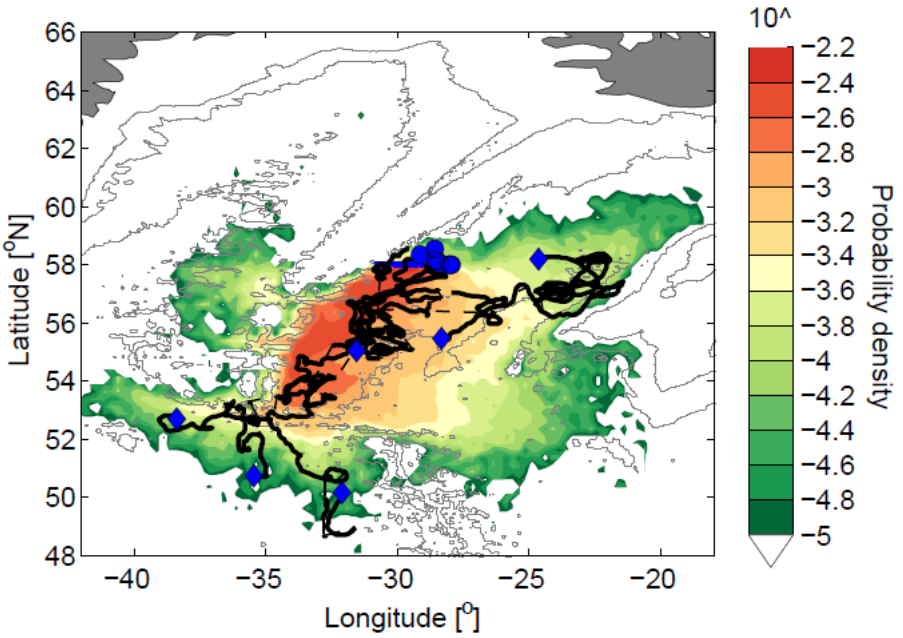

Figure 19: Pathways of deep ISOW from RR eastern flank. Similar to Figure 18, but for pathways of ISOW originated at greater depths. The initial (final) positions of the 6 RAFOS floats are shown as blue circles (diamonds). The initial launch locations of simulated floats are shown with a blue short line at 58°N. The total float number is 2534.

Westward transport across the CGFZ has been shown to be impacted by meridional shifts of the NAC (Schott, et al., 1999; Bower & Furey, 2017). For example, Bower and Furey (2017) show that on eddy time scales, a strong westward ISOW transport across the CGFZ is observed when there is a southward shift of the NAC: when the NAC approaches the northern channel of the CGFZ, the transport in the ISOW layer is eastward. To test whether NAC's shift has a similar impact on ISOW transport on interannual time scales, I plot the annual cross-sectional zonal velocity across the

CGFZ in 1996 and 2003 (Figure 20). The former year is when the Eulerian-based westward ISOW transport in the model is the strongest during the decade and the latter year is when the transport is the weakest.

In 1996, the NAC almost disappears in the upper water column of the CGFZ northern channel. Instead, a bottom intensified westward velocity is seen. In 2003, a branch of eastward NAC overlies a weak westward ISOW transport, but this shift is less evident compared to what is observed by Bower and Furey (2017) on eddy time scales. Though the model behavior appears to be consistent with what has been inferred from Bower and Furey (2017), further work is needed to assess the dependence of ISOW transport variability on NAC variability on interannual time scales.

In summary, deep ISOW along the RR eastern flank mainly flows southward until the CGFZ, where some continues spreading southward along either side of the MAR and some crosses westward into the western subpolar gyre. The westward crossing varies on both eddy time scales and interannual time scales, apparently in concert with NAC interactions. Within two years from 58°N, very few floats flow northward along the western RR boundary after reaching CGFZ.

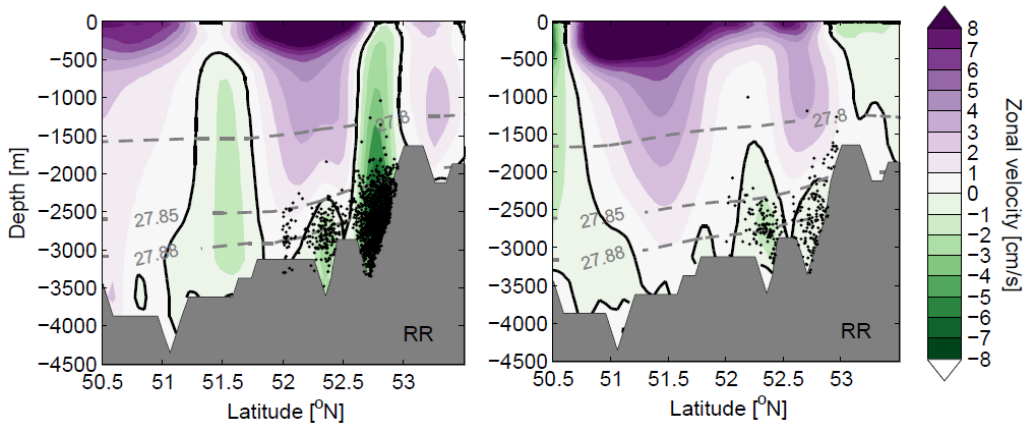

Figure 20: Interaction between NAC and ISOW transport in CGFZ. (Left) Annual mean zonal velocity across the CGFZ in 1996. The float positions while crossing the fracture zone in 1996 are plotted as black dots. (Right) Similar to the left panel, but for the mean zonal velocity across CGFZ in 2003. The zero velocity contour is shown in black. Isopycnals are contoured in dashed gray.

3.4.3 Southward spreading of ISOW into the WEB

The third ISOW export pathway discussed in this paper is a southward spreading into the WEB east of the MAR. Here I present previously unpublished current meter observations that measure this deep southward transport. Figure 21 (left) shows the mean velocity at mooring locations C, G, F and Z (deployed from June 1999 to July 2000) and M, A, R and T (deployed from August 1998 to June 1999) at instrument depths between 1650 and 3890m. The deep-reaching northeastward NAC is observed at moorings G, F and Z. At mooring R, a bottom-intensified southward flow is observed in both the salty ISOW layer and the relatively fresh LDW layer near the bottom, as shown by the hydrographic section from CTD casts conducted in June 1999 (Figure 21, right).

The southward velocity increases from 1.7 cm/s to 6.1 cm/s in the ISOW layer and reaches 8 cm/s in the LDW layer.

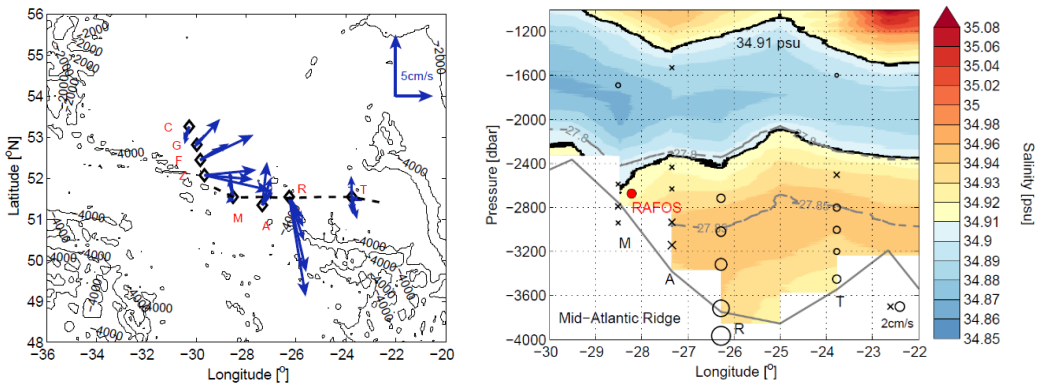

Figure 21: Observed velocity field in ISOW layer east of CGFZ. (Left) Mean velocities at the depths of all current meters for moorings C, G, F, Z, M, A, R and T (black diamonds). Moorings C, G, F and Z were deployed on June 25 1999 and recovered on July 1 2000. Moorings M, A, R and T were deployed on August 9 1998 and recovered on June 16 1999. All current meters are located between 1650 and 3890 dbar. The CTD section is shown as a black dashed line. (Right) Observed salinity in June 1999 east of the MAR (~51.5°N) from the CTD stations shown in the left panel. The depths of the current meters for each mooring are marked as black circles if the mean velocity is southward and crosses if the mean velocity is northward, with size proportional to the current speed. A few markers are below the bottom (gray solid line) due to the longitude difference between the mooring locations and the CTD section. The red circle indicates the approximate location of the RAFOS float when it crossed 51.5°N. Isopycnals are shown as dashed gray contours.

The modeled annual mean velocity in 1998, when moorings M, A, R and T were in water, is indicated with blue arrows in Figure 22 (left), with the cross-sectional meridional velocity at 51.5°N shown in Figure 23 (left). Also shown is the annual mean velocity field in 1992, when the southward velocity is the strongest of all model years (Figure 22 left, green arrows; Figure 23 right). Overall, though the southward velocities in the ISOW layer are evident near moorings A and R in FLAME for both years, their

magnitudes are much weaker than observations. The bottom intensification of the observed velocity at mooring R is also not evident in FLAME, suggesting an underestimate of the southward spreading in the model.

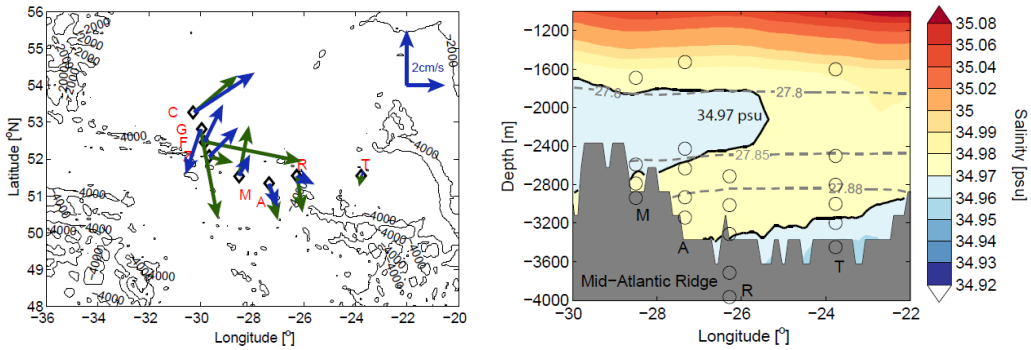

Figure 22: Modeled velocity fields in ISOW layer east of CGFZ. (Left) Annual mean velocity from FLAME in 1998 (dark blue) and 1992 (dark green), at mooring locations. The velocity is averaged over the ISOW layer. Mooring locations are indicated with black diamonds. (Right) Modeled salinity averaged from 1990 to 2004 across 51.5 °N. The longitudes of the moorings M, A, R and T are shown as black circles. Isohalines are shown in solid black and isopycnals are contoured as dashed gray lines.

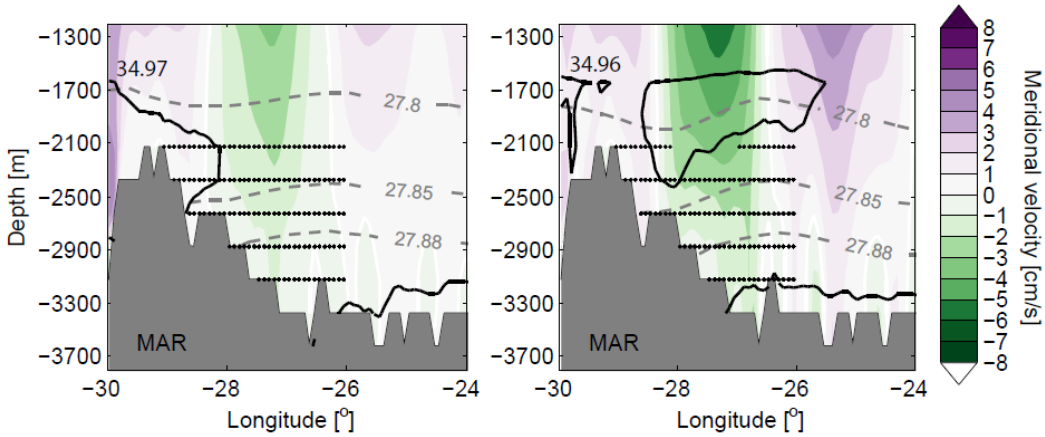

Figure 23: Launch locations of simulated floats east of CGFZ. The annual mean meridional velocity across 51.5°N in FLAME in 1998 (left) and 1992 (right). Black solid contour shows the isohaline and the gray dashed contours indicate isopycnals. Black dots indicate the launch locations of simulated floats along 51.5°N.

The meridional velocity fields at 51.5°N shown in Figure 23 also reveal significant variability from year to year in the model, which might result from the meandering or the position shift of the NAC. To test whether the velocity fields impact the southward ISOW spreading, simulated floats are released in the ISOW layer in 1998 and in 1992. The two-year probability maps of float trajectories for each of these launches are shown in Figure 24. In 1998, when the southward velocity is relatively weak, the floats prefer to travel northeastward towards the Rockall Plateau (Figure 24, left). However, in 1992, when the southward velocity is relatively strong at 51.5°N, a southward spreading pathway emerges (Figure 24, right). This southward pathway is consistent with the southward movement of a RAFOS float launched in the ISOW layer (2600 dbar) east of the CGFZ, as reported by Lankhorst and Zenk (2006). The track of this RAFOS float is also shown in Figure 24.

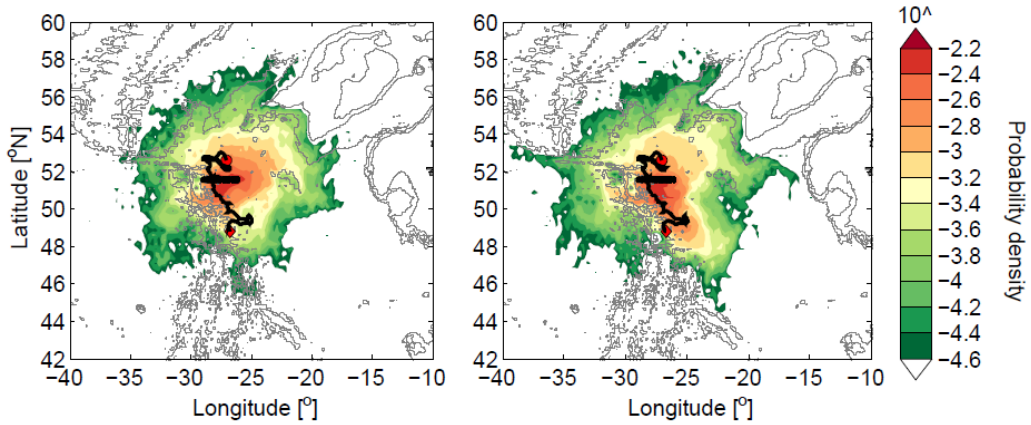

Figure 24: Spreading of ISOW east of MAR. Probability maps of float trajectories two years after release in 1998 (left) and 1992 (right) at 51.5°N in FLAME. 2824 floats were released every 3 months in the ISOW layer in 1998 and 2650 were released in 1992. Initial launch locations are shown in black (also in Figure 23). A

RAFOS float trajectory is shown as a black solid curve with its initial (final) location denoted by a red circle (diamond). The RAFOS float data is obtained from Lankhorst et al. (2017).

Although a southward spreading of deep waters is observed along the MAR eastern flank, it is difficult to ascertain the waters' source. LSW from the western subpolar gyre, subtropical water carried by the NAC, LDW from the south and ISOW from the Iceland Basin are all expected components of the deep water in this region. To study the possible origins of these deep waters, I computed backward trajectories of simulated floats released every 3 months in 1992 at 51.5°N near the moorings M, A and R. The probability maps (Figure 25) from this launch reveal that the primary source of the deep waters in this area is the interior Iceland Basin, with another important origin east of the Flemish Cap, where eastward-flowing LSW meets waters carried by the NAC. Based on these model results and current knowledge about the North Atlantic subpolar gyre circulation, it is concluded that the waters moving southward along the eastern MAR flank are a composite of subpolar water masses, with ISOW a strong contributor. This conclusion is consistent with an Eulerian study by Xu et al. (2010).

In summary, from both observations and FLAME output, a southward spreading of ISOW into the WEB is identified east of the MAR. However, in FLAME, this southward spreading appears much weaker and is temporally variable depending upon the local velocity field, which has been suggested to be influenced by NAC meandering (Bower & Furey, 2017).

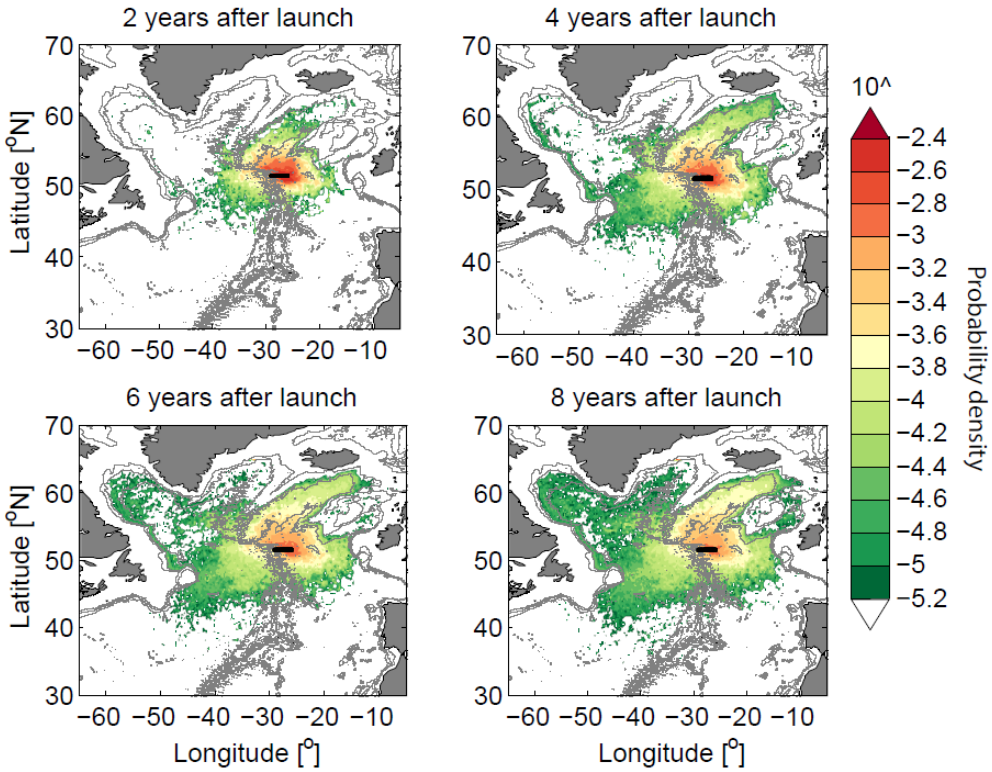

Figure 25: Backward-tracked deep waters from east of CGFZ. Probability maps of backward trajectories of floats released every 3 months in 1992 in the ISOW layer at 51.5°N (black short line).

3.4.4 An overall view of ISOW spreading pathways from the Iceland Basin

In order to identify ISOW across the entire Iceland Basin, I use current meter and hydrographic data from the OSNAP mooring array and data from FLAME. The observed mean velocities (July 2014-July 2015) at depths ≥ 1000m are shown in red in Figure 26, along with the 15-year mean volume transport in the layer below the isopycnal of 27.80 kg/m^3 in FLAME. The vertical structure of the velocity field at the observational array and from FLAME are shown in Figure 27. Overall, the modeled velocity structure compares fairly well with observations: they both reveal bottom-

intensified southward velocity cores near the mooring locations (one core near moorings M1, D1 and D2, one near D4 and another near M3). A difference between the model and observations is noted: in the model, the bottom southward flow field is much weaker at moorings D3 and M2, and reverses directions at mooring M4. The difference at mooring M4 can perhaps be attributed to the fact that the observations were conducted during 2014 and 2015 while FLAME spans only from 1990 to 2004. For example, the flow direction near mooring M4 does change from year to year in FLAME (e.g. the velocity at M4 is northward in 2003, not shown). The weak velocities at moorings D3 and M2 in the model are present every year, revealing the shortcoming of FLAME in capturing the entire boundary current east of the RR. However, ISOW in the high velocity core of the boundary current is well resolved in the model, and this branch is the major ISOW transport branch.

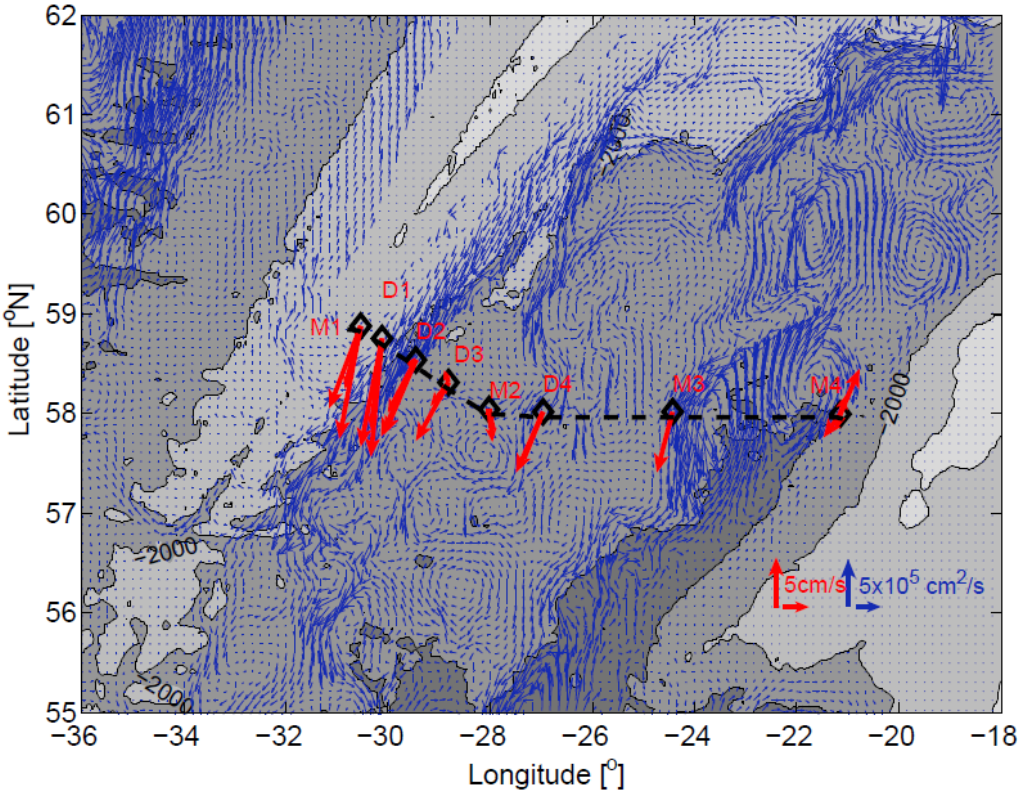

Figure 26: Mean velocity fields in ISOW layer in the Iceland Basin. Annual mean velocity from current meter data at all observed depths is shown with red arrows. Locations of mooring M1, D1, D2, D3, M2, D4, M3, and M4 are shown with black diamonds. All moorings were deployed in July 2014 and recovered in July 2015. Blue arrows show the 15-year mean volume transport per unit width (product of velocity and layer thickness, unit: cm^2/s) for the layer below the isopycnal of 27.80 kg/m^3. Black dashed line shows the section in FLAME that replicates the mooring site. 1000m, 2000m and 3000m isobaths are shown in gray.

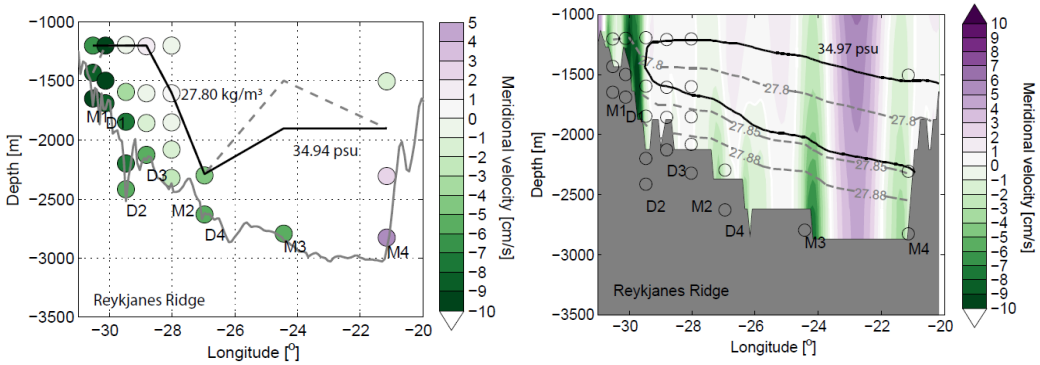

Figure 27: Comparison of the mean velocity structure between observations and FLAME across the OSNAP section. (Left) Mean meridional velocity from OSNAP moorings between July 2014 and July 2015, with bathymetry shown by the gray line. The 27.80 kg/m³ isopycnal and 34.94 isohaline are plotted in solid black and gray dashed lines, respectively. Note that the salinity and density for each mooring array are measured with CTDs, which occupy more vertical layers than current meters. (Right) Mean meridional velocity averaged from 1990 to 2004 in FLAME along the section that replicates the OSNAP array (black dashed line in Figure 26). The vertical distributions of the OSNAP current meters are shown in open circles. Isopycnals are contoured in dashed gray and the isohaline is contoured in sold black. Modeled bathymetry is shaded in dark gray. A few deep open circles are located in the gray area due to the coarse resolution of bathymetry in FLAME.

To study the overall ISOW spreading, I released floats every 3 months in 1990 in the bottom-intensified southward velocity cores in the ISOW layer identified above. The two western cores near M1-D2 and near D3 are clearly associated with southward ISOW flow from the northern Iceland Basin, while the core near M3 appears to be at least partly associated with a localized deep circulation cell in the model in the eastern part of the basin. These floats were released across 59°N, a latitude close to the mooring section and one that captures the southward ISOW transport cores (Figure 28, left). After launch, floats were integrated forward by 10 years.

From the probability map of 10-year trajectories of exported floats (Figure 28, right), the strong recirculation of ISOW in the Iceland Basin and the three major export pathways discussed above are recognized: one branch crosses into the Irminger Sea via gaps along RR, while another branch spreads southward along the eastern RR flank until the CGFZ area, where it bifurcates into a westward pathway through the CGFZ and a pathway continuing southward along the eastern flank of the MAR. There is also a relatively weak southward spreading of the floats along the western flank of the MAR. Launches in years other than 1990 were performed; no discernable difference in the overall spreading pathways was detected.

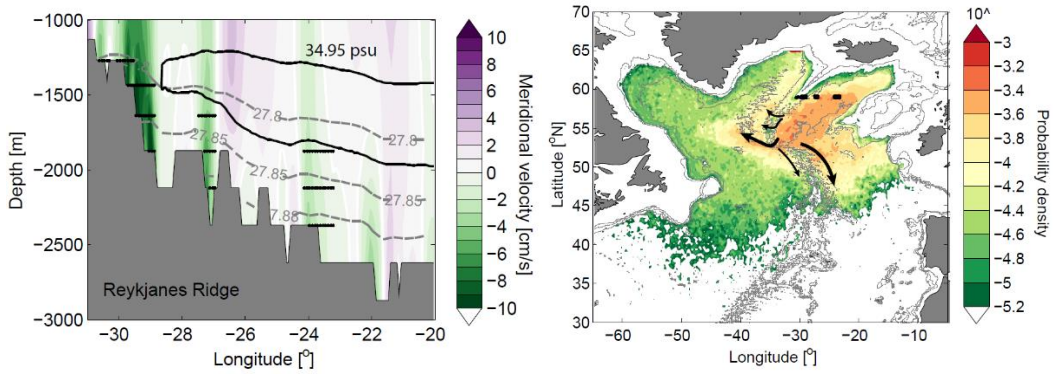

Figure 28: Overall spreading of ISOW from central Iceland Basin. (Left) Annual mean meridional velocity across 59°N in 1990 from FLAME. Initial launch locations of floats are shown as black dots. (Right) Probability map of 10-year trajectories of exported floats (1227 in total). Floats were released every 3 months in 1990 in the southward velocity cores at 59°N. Only floats whose final locations are outside of the Iceland Basin are used for this plot. Floats' initial locations are shown as black dots at 59°N. Major ISOW export branches are illustrated with black solid curves. 1000m, 2000m and 3000m isobaths are shown in gray.

3.5 Quantification of ISOW pathways – A Eulerian view

In this section, I use FLAME to calculate the annual volume transport of ISOW in the eastern North Atlantic, and compare those transports to results from previous observational and modeling studies. In FLAME, the mean (1990-2004) of the annual alongshore transport of ISOW along the slope south of Iceland (~62°N) is 3.8 Sv, with a standard deviation of 0.7 Sv (labeled in blue in Figure 30). As it flows southward, this branch splits into two branches that remain near the boundary. A third southward branch of ISOW is located west of the Maury Channel in the basin interior. This branch, with a transport of 1.8 ± 0.7 Sv, has no obvious connection to the ISOW branch south of Iceland and instead appears part of a local circulation feature. The net southward transport in the interior Iceland Basin east of 26°W, which includes this third branch, is 0.4 ± 0.4 Sv. Summing all transports, I derive a net southward transport in the ISOW layer across the entire Iceland Basin at 59°N of 4.2 ± 0.5 Sv.

The transport time series for the major ISOW export branches are plotted in Figure 29. The mean cross-RR transport between 60°N and CGFZ is calculated as 1.2 ± 0.1 Sv and the mean transport across the CGFZ is 0.9 ± 0.4 Sv. These two branches do not have significant trend, but the CGFZ branch exhibits strong interannual variability. Finally, the net throughput of deep waters into the WEB is 2.8 ± 0.7 Sv on average. This branch exhibits a significant increasing trend since 1990. Most of these modeled transports compare favorably with previous studies (values in magenta in Figure 30),

except for the branch through the CGFZ. Part (though certainly not all) of this mismatch may be attributed to the subjective choice of the salinity threshold for ISOW the layer in the model. Appropriate choices for this threshold yield a range of mean transports from 0.8 Sv to 1.3 Sv, with the latter closer to previous transport estimates.

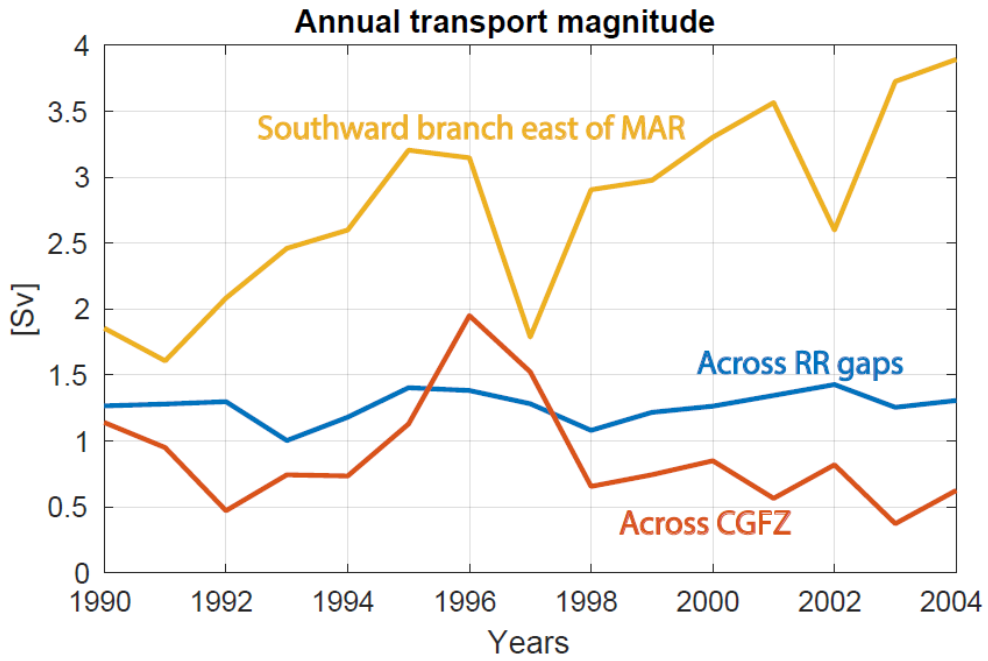

Figure 29: Time series of ISOW transport magnitudes via different branches.

3.6 Quantification of ISOW pathways – A Lagrangian view

To understand the source of the waters constituting each of these branches, I turn again to a Lagrangian perspective. Floats were released every 3 months each year from 1990 to 2004 in FLAME across 59°N in the Iceland Basin (red dashed line in Figure 30) and integrated forward by 10 years. Floats were released each year in the ISOW layer regardless of whether the initial velocity was northward or southward. The interest is in the export of floats across the red solid lines marked in Figure 30, selected to designate

the destinations of the three identified spreading branches. Thus, these sections are used to measure export. For example, if a float crosses the red solid section along the RR axis sometime within 10 years of launch, and by the end of the 10th year it remains in the western North Atlantic, this float is considered to have been exported through the RR. With this counting, the number of exported floats through each section (RR, CGFZ and east of MAR) is obtained from each launch year. Those numbers are converted to percentages by dividing by the total number of initial floats launched (4860 ± 950, float number varies in different years as ISOW layer thickness varies).

The percentage of each branch increases almost linearly with time of integration (not shown). As seen in Figure 30, 10 years after launch, the fraction exported across the RR is 7%, with a standard deviation of 1% among all launches. The fraction exported across the CGFZ is 13 ± 2% and east of the MAR is 21 ± 3%. The southward export of ISOW along the eastern flank of the MAR is more significant compared to the other two export pathways. The distribution is slightly different if floats are released only within the mean southward velocity cores across 59°N: 11 ± 1% across the RR; 10 ± 2% through the CGFZ; and 18 ± 2% along the eastern flank of the MAR. Also, a small portion (4 ± 0.5 %) of the floats flow southward along the western flank of the MAR. Most of the remaining floats are un-exported, meaning that they remain in the Iceland Basin during this 10-year period.

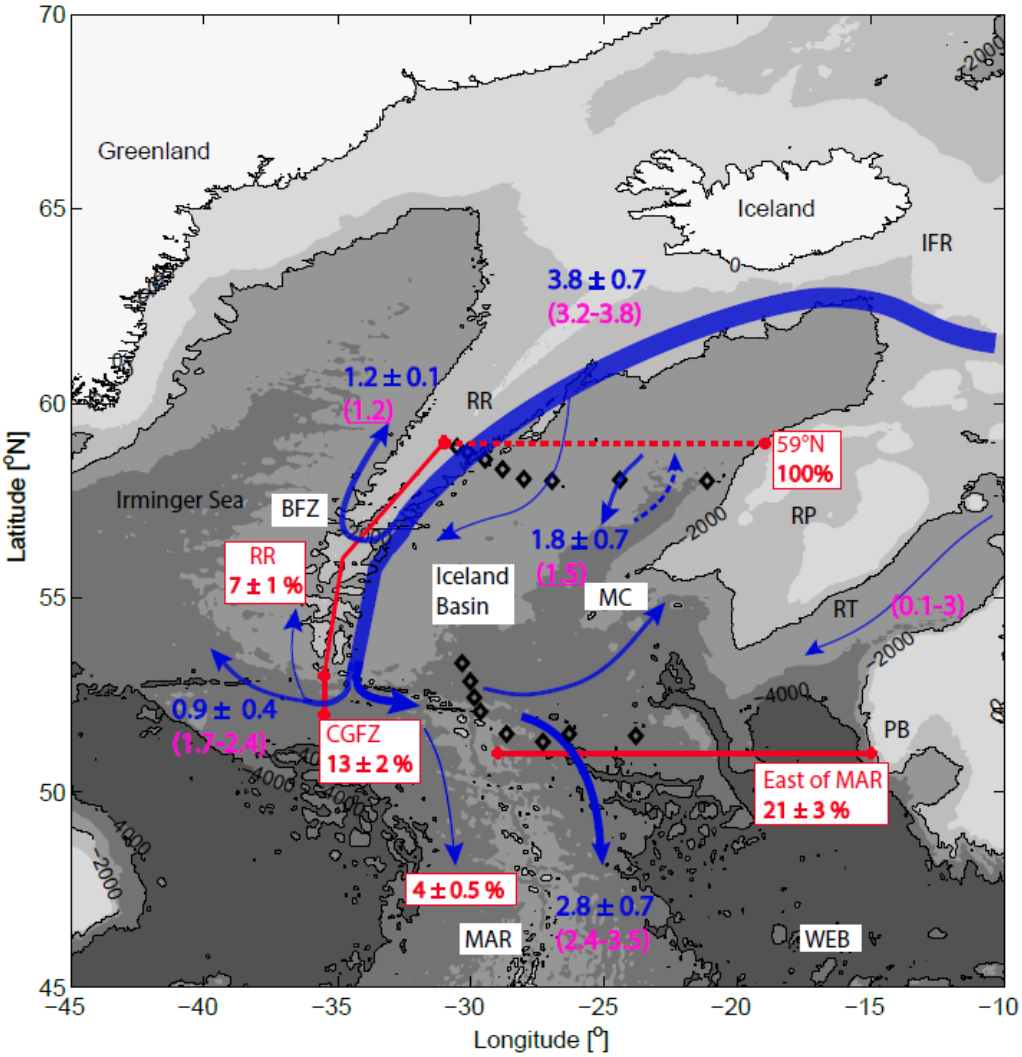

Figure 30: An updated schematic of ISOW pathways in the eastern North Atlantic. Mean pathways are shown in blue curves. Volume transports (Sv) for major branches from the model are labeled in blue. The transport values from previous studies are listed in magenta within parentheses, with those from modeling studies underlined. The percentage of exported floats within 10 years after release at 59°N (red dashed line) through different sections (RR, CGFZ, east of MAR) is shown in red. Mooring arrays used in this paper are plotted as black diamonds.

Float export variability through the different sections as a function of their initial launch years is shown in Figure 31. The percentage of southward export along the eastern flank of the MAR is negatively correlated with the export percentage via RR gaps (r = -0.75 before detrending; r = -0.66 after detrending). The correlation primarily stems from opposite trends (Figure 31, left) and anti-phase variability on semi-decadal time scales (Figure 31, right). A negative correlation is also seen between the southward export east of the MAR and the westward export across the CGFZ, with a correlation coefficient of -0.38 before detrending and -0.83 after detrending. The strong negative correlation between the two detrended time series results from the anti-phase variability on interannual time scales. If the export percentage via the RR gaps and through the CGFZ are added, the total is significantly anti-correlated with the southward export pathway east of the MAR (r = -0.78 before detrending; r = -0.91 after detrending), indicating that when cumulative ISOW transport across RR gaps and the CGFZ is relatively strong, southward ISOW transport into the WEB is weak. One should note that since the data is recycled to get the 10-year float trajectories for launches after 1995, the export variability derived here might not reflect the real export variability from year to year. However, this work sheds light on the potential relationship between different pathways in exporting ISOW out of the Iceland Basin.

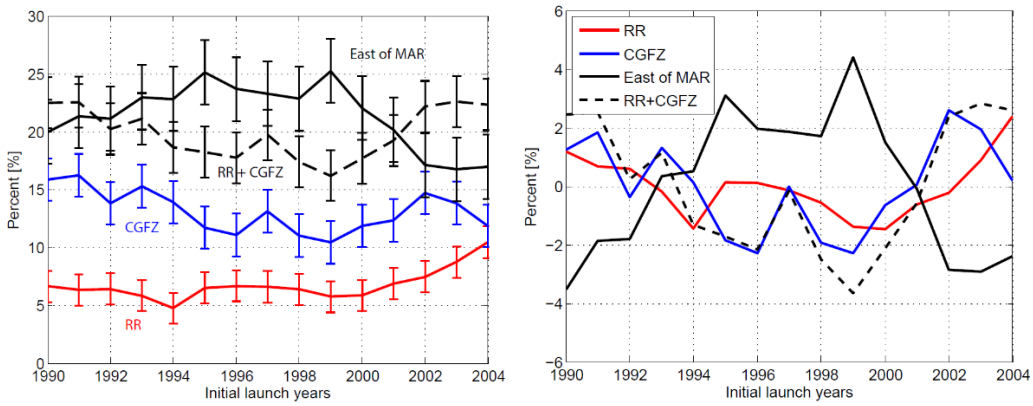

Figure 31: Export variability expressed as a percentage of floats through different sections within 10 years. Floats were released across the entire Iceland Basin at 59°N. (Left) Before detrending. The standard deviation is shown as an error bar. (Right) After detrending. Export percentages from studies where floats were released only in the southward velocity cores at 59°N show similar variability to the time series shown above.

3.7 Summary

Earlier studies of the ISOW pathways in the eastern North Atlantic have relied on model output and/or limited observations; in both cases pathways were inferred using an Eulerian framework. In this study, for the first time, I use a combination of Eulerian and Lagrangian approaches, and a combination of observations and high-resolution numerical model output, to trace and quantify ISOW spreading branches.

After entering the Iceland Basin, ISOW primarily travels along the eastern flank of the RR, with some ISOW flowing to the basin interior. When it reaches 59°N, three ISOW transport cores are identified from an OSNAP mooring array and from model output: one major core is along the RR boundary; another weaker core is in the basin interior at ~27°W; and the third one resides in the eastern basin at ~24°W, appearing to

be part of a local circulation cell. With observed and simulated trajectories, the spreading branches of ISOW from these transport cores are identified. A portion of shallow ISOW along the RR eastern boundary escapes to the Irminger Sea via gaps along the Ridge (modeled volume flux: 1.2 ± 0.1 Sv) before reaching the CGFZ. The remaining ISOW, either along the boundary or from the basin interior, primarily flows southward to the CGFZ, where one branch of this deep water crosses westward into the western subpolar gyre (modeled volume flux: 0.9 ± 0.4 Sv) and another continues spreading southward into the WEB (modeled volume flux: 2.8 ± 0.7 Sv). While these export branches are consistent with previous Eulerian studies, they are identified here with Lagrangian floats for the first time. Furthermore, this study provides the first direct observational validation of the southward branch into the WEB, a validation possible due to the examination of previously unpublished current meter data. In addition to the identification of the major export pathways mentioned above, Lagrangian floats reveal a weak southward spreading along the western flank of the MAR and strong recirculation of the remaining ISOW in the Iceland Basin.

A quantification of different ISOW branches in a modeled Lagrangian frame reveals that downstream of 59°N in the Iceland Basin after 10 years, 7-11% of ISOW escapes the basin via RR gaps; 10-13% flows into the western subpolar gyre through the CGFZ; and 18-21% continues moving southward into the WEB along the eastern flank of the MAR. In other words, the export via RR gaps and through the CGFZ are

comparable, while the southward export east of the MAR is more significant. Most of the remaining ISOW (~50%) stays in the Iceland Basin 10 years following launch. A small portion (4%) exports along the western flank of the MAR. Note that these float percentages indicate preferred ISOW pathways from 59°N over the course of 10 years, a different metric than the volume transport at a fixed location.

From our modeling experiments, I find that the southward ISOW transport percentage into the WEB and the westward ISOW transport percentage through the CGFZ have strong interannual variability. In both cases, this variability appears linked to the variability of the NAC in the magnitude and/or position. Further work is needed to confirm the dynamic link between them.

Changes in the modeled pathways are shown to be interrelated. An increase of the total ISOW export percentage across the RR gaps and through the CGFZ is associated with a decrease in the southward transport percentage to the WEB on interannual time scales as well as on longer time scales. On interannual time scales, this association is driven by the relationship between the CGFZ transport and the southward transport: when the westward CGFZ transport is relatively strong, the southward transport into the WEB is relatively weak, and vice-versa. On longer time scales, the transport through the RR gaps is more important to this linkage.

With this work, I have provided an overall view of the ISOW spreading pathways and confirmed them to the extent possible with observations. However, there

is still a lack of understanding on the variability of these transport pathways and the mechanisms responsible for that variability. As more OSNAP data becomes available in the next few years, the gaps in that understanding are expected to diminish.

4. Exploring the Relationship between NADW Transport and AMOC

While the ocean community has placed a strong focus in recent years on the latitudinal coherence of AMOC, continuity in the downstream transport of the water masses that constitute the lower AMOC limb has received considerably less attention. With output from ocean circulation models and an ocean reanalysis dataset, I investigate UNADW and LNADW transport from the subpolar to the subtropical gyre, and assess their relationship with AMOC.

4.1 Introduction

Models have revealed a meridional coherence of AMOC variability in response to the production of LSW on decadal time scales (Delworth, et al., 1993; Yeager & Danabasoglu, 2014; Polo, et al., 2014; Biastoch, et al., 2008; Zhang, 2010). It is generally assumed that this meridional coherence is achieved via the export of subpolar-originated deep waters to lower latitudes, yet a few recent studies have cast doubt on this supposition.

From an analysis of moored current meter data over two periods 1993-1995 and 1999-2001, Schott et al. (2004) found a lack of causal linkage between Labrador Sea convection and the deep water transports east of the Grand Banks. The authors concluded that the Grand Banks boundary current transport was more closely related to the NAC variability than to upstream transport variability. By focusing only on boundary current transports, this study did not account for the transport of water

masses carried equatorward in the lower AMOC limb by eddy-induced interior pathways (Lozier, 1997; Bower, et al., 2009; Gary, et al., 2012).

A second study, based on an eddy-permitting ocean-general circulation model, explores the relationship between LSW production and its Lagrangian export to the subtropical gyre on interannual to decadal time scales (Zou & Lozier, 2016). The authors find a negligible or at best modest impact of LSW production on the LSW export to the subtropical gyre. This finding is attributed to the strong recirculation of LSW within the subpolar gyre (Lavender, et al., 2005; Gary, et al., 2012) and the mixing and stirring along the export pathways from the subpolar to the subtropical gyre that act as a strong filter for LSW production signals.

Also related to the linkage between the AMOC and deep water mass transport are recent studies of observations at the RAPID array (26.5°N) that have revealed the dominance of local forcing on deep water transport variability. AMOC variability on interannual to semi-decadal time scales at this subtropical latitude is dominated by wind-driven upper ocean transport (Cabanes, et al., 2008; Roberts, et al., 2013; Zhao & Johns, 2014). Transport in the lower AMOC limb has, as expected, an in-phase response to these upper limb changes: as the upper limb increases or decreases its northward flow, the lower limb's southward flow responds in kind. Interestingly, this mass compensation is largely contained within the Lower North Atlantic Deep Water (LNADW, 3000m-5000m) layer rather than the Upper North Atlantic Deep Water

(UNADW, 1000m-3000m) layer (Figure 32) (McCarthy, et al., 2012; Frajka-Williams, et al., 2016), the latter of which is generally understood to contain LSW.

Taken together, these studies raise questions about: (1) the extent to which deep water transport anomalies from the subpolar gyre impact transport anomalies downstream; and (2) the extent to which local AMOC variability is linked to water mass transport anomalies. Though studies on the meridional connection of AMOC variability are extensive (Bingham, et al., 2007; Zhang, 2010; Biastoch, et al., 2008), to my knowledge no study to date has explored these two questions. To address this gap, I utilize output from eddy-resolving/permitting ocean circulation models and an ocean reanalysis. This choice permits an exploration of connections on longer time scales and over a broader spatial domain than current observations allow.

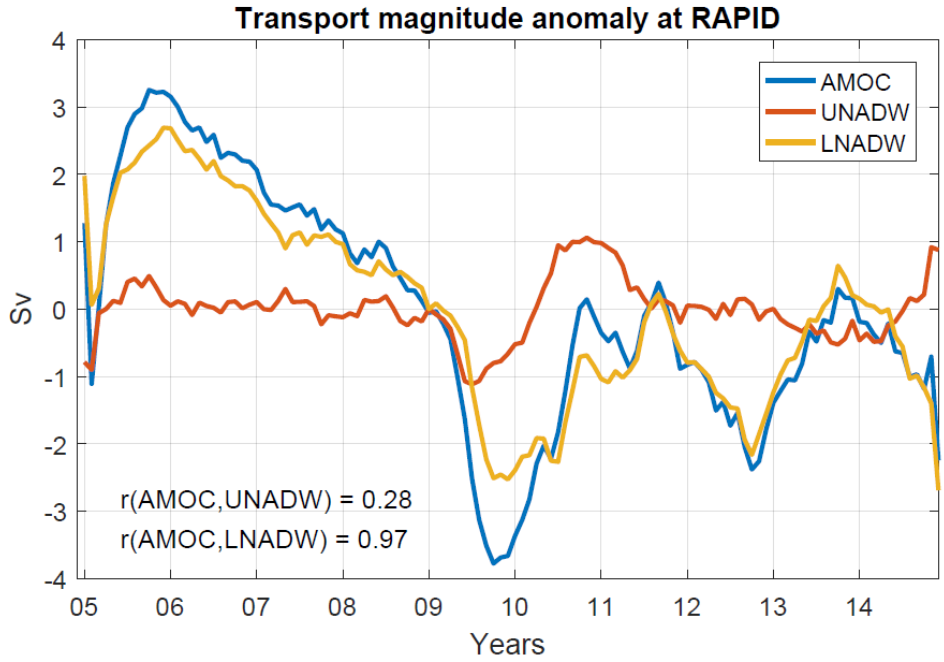

Figure 32: Time series of monthly AMOC, UNADW and LNADW transport magnitude anomalies at RAPID (26.5°N). The time series are deseasonalized and smoothed with a 1-year filter. Data from the RAPID-MOCHA program are funded by the U.S. National Science Foundation and U.K. Natural Environment Research Council and are freely available at www.rapid.ac.uk/rapidmoc and www.rsmas.miami.edu/users/mocha.

4.2 Data and methods

4.2.1 Model data

The model outputs I used are FLAME and ORCA025. Further information about these two models can be found in sections 3.3.4 and 2.2.2.

I also use the Simple Ocean Data Assimilation (SODA2.2.4) reanalysis in our study, which has been shown to be the best reanalysis to assess the AMOC variability (Tett, et al., 2014). SODA is based on an ocean circulation model, POP2.x, forced with the 20CRv2 atmospheric data product, and sequentially assimilates observations from

World Ocean Database (WOD) and the International Comprehensive Ocean-Atmosphere Data Set (ICOADS) (Carton & Giese, 2008). The model has a horizontal resolution of 0.5° on average and has 40 vertical levels. Data used in this paper is the monthly output from 1961 to 2009.

It is emphasized that while the interest is in how this relationship compares among the three models, the study focus is not on an inter-model comparison of AMOC and these water masses.

4.2.2 Calculation of AMOC in σ_2 space

At each latitude (φ), the AMOC strength is defined as the maximum of the overturning streamfunction (Ψ) in density space with reference to 2000 dbar (σ_2),

$$AMOC(\varphi, t) = \max \Psi(\varphi, \sigma_2, t) = \max \left[\int_{\sigma_2}^{\sigma_2\, surface} \int_{x_w}^{x_e} v(x, \varphi, \sigma_2, t) dx d\sigma_2 \right]. \quad (3)$$

Here, $v(x, \varphi, \sigma_2, t)$ is the meridional velocity in σ_2 space and x is longitude, with x_w and x_e denoting the westward and eastward positions, respectively, of the ocean bottom at a particular σ_2 level. The AMOC strength, $AMOC(\varphi, t)$ is calculated from monthly data at each latitude between [25°N, 53°N] and achieved at $\sigma_2 = \sigma_2^{max}(\varphi, t)$. The outputs are then averaged annually and a linear trend is removed.

4.2.3 Definition of UNADW and LNADW

The UNADW layer is defined as the water mass directly below the time-varying isopycnal that separates the northward from the southward flow, i.e. at $\sigma_2^{max}(\varphi, t)$, and above the fixed isopycnal of 36.98 kg/m^3, determined to be the lower bound for

UNADW from an analysis of temperature, salinity and potential vorticity fields. The LNADW layer is defined as the layer below the 36.98 kg/m^3 isopycnal and above the ocean floor. Both layers are dynamic, meaning that their thickness varies in time, and they constitute the entire AMOC lower limb.

Transport time series in both UNADW layer and LNADW layers are calculated at each latitude as the integrated transport across all longitudes over each layer's thickness, i.e.,

$$T(\varphi, t) = -\int_{\sigma_{2\ upper\ bound}}^{\sigma_{2\ lower\ bound}} \int_{x_w}^{x_e} v(\mathrm{x}, \varphi, \sigma_2, t) dx d\sigma_2. \quad (4)$$

With this sign convention, a southward flow will have a positive value of $T(\varphi, t)$. All time series are derived from monthly data, which are then averaged into annual means after the trend is removed.

4.3 Meridional connection of AMOC anomalies

I first explore the meridional coherence of AMOC anomalies. Overall, AMOC in either subpolar or subtropical gyre shows in-phase variability, with discontinuity at the gyre-gyre boundary (Figure 33 for FLAME; Figure 34 for ORCA025; Figure 35 for SODA). To specifically evaluate the downstream propagation of the AMOC anomalies in the subpolar gyre, cross-correlation coefficients are calculated using the AMOC time series at 53°N and the time series at other latitudes. In addition to the gyre-specific in-phase variability of AMOC, I find that in all of the models, the subtropical AMOC shows significant linkage to the subpolar AMOC, with the former lagging by less than 4 years

(Figure 36; consistent with Zhang, 2010). In the next section, we examine the presence of this meridional connection in different vertical layers of AMOC lower limb.

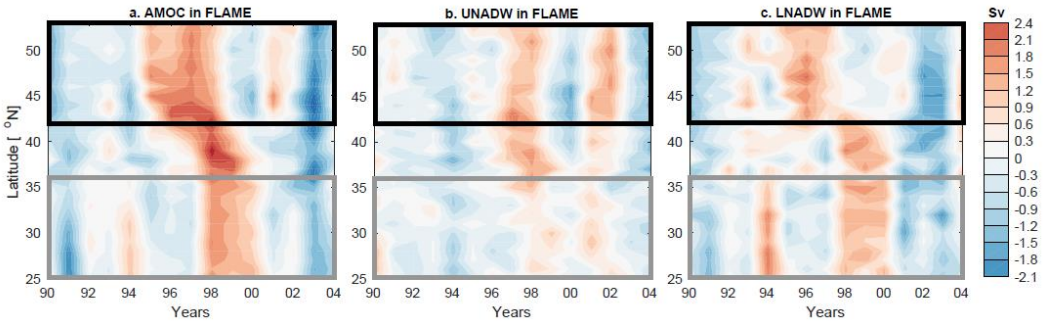

Figure 33: Hovmöller diagrams of AMOC/transport anomalies in FLAME. (a) AMOC anomalies. (b) Anomalies in the UNADW layer. (c) Anomalies in the LNADW layer. Black (gray) boxes indicate the subpolar (subtropical) gyre.

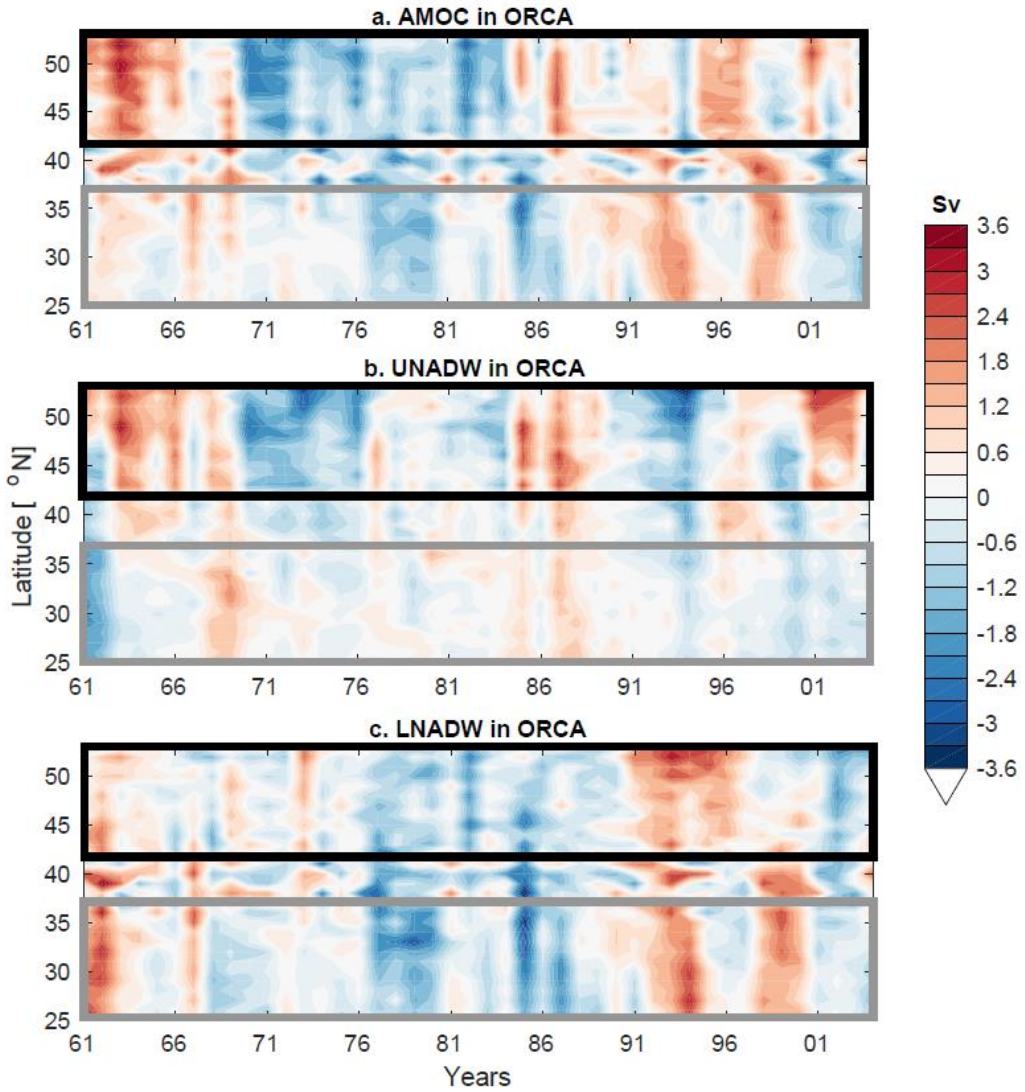

Figure 34: Hovmöller diagrams of AMOC/transport anomalies in ORCA025.

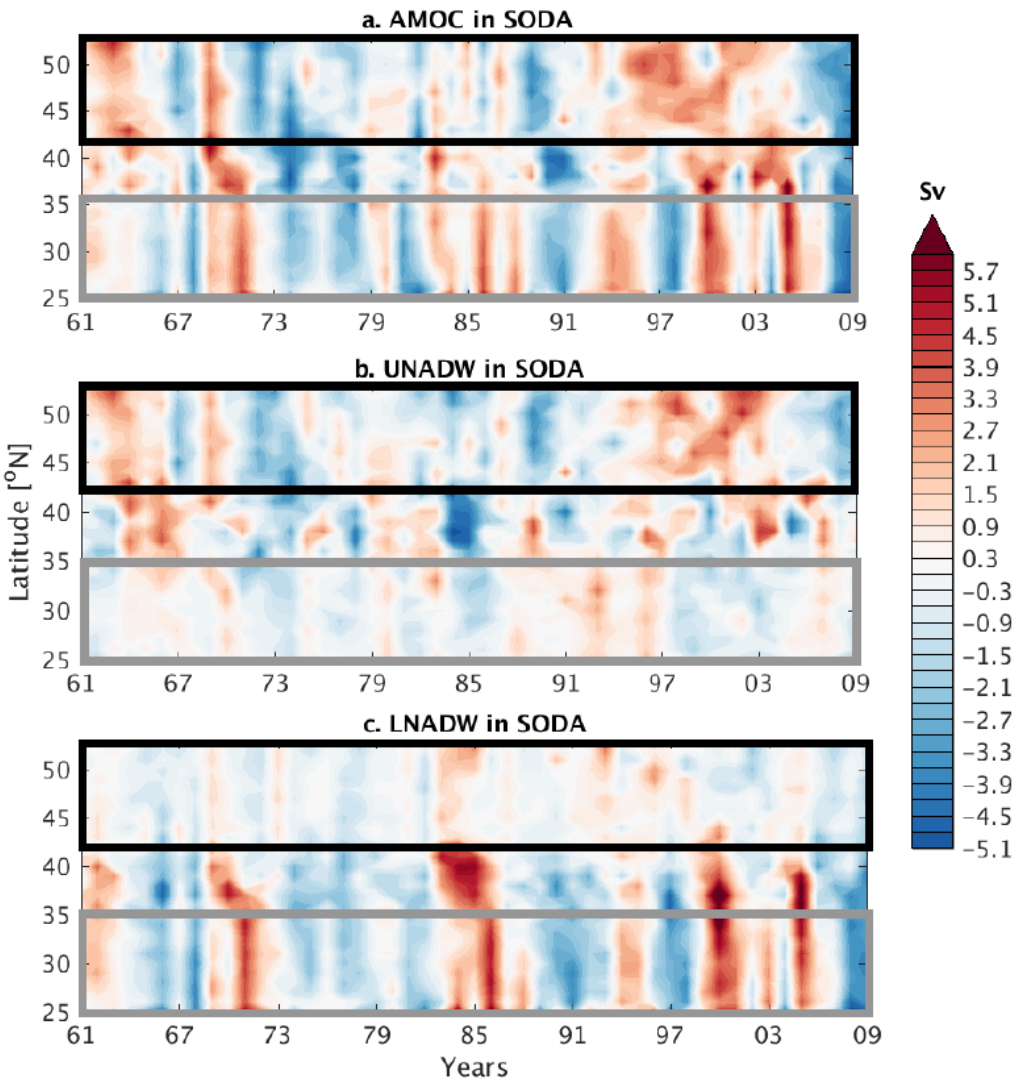

Figure 35: Hovmöller diagrams of AMOC/transport anomalies in SODA.

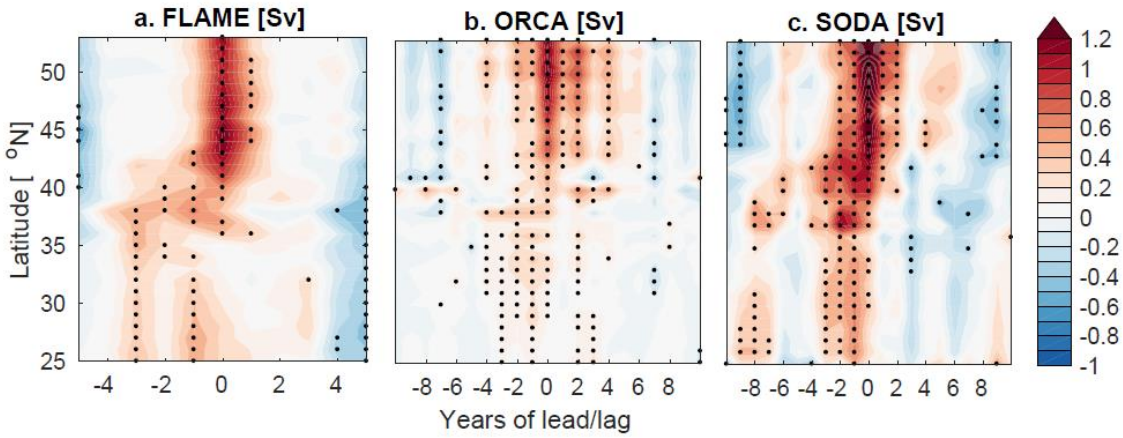

Figure 36: Cross-correlation between normalized AMOC time series at 53°N and AMOC at other latitudes. (a) In FLAME. (b) In ORCA025. (c) In SODA. Shading indicates the coefficient times the standard deviation of AMOC at each latitude (unit: [Sv]). Negative years indicate that the 53°N time series are leading. Black dots indicate correlations significant at a 95% confidence level.

4.4 Meridional connection of deep water transport anomalies

To understand the extent to which transport anomalies from the subpolar gyre are connected to transports downstream, I investigate the meridional connection of transport anomalies in the UNADW and LNADW layers.

In general, all transports show intra-gyre in-phase variability for both the subpolar and the subtropical gyres (Figure 33 for FLAME; Figure 34 for ORCA025; Figure 35 for SODA). However, at the latitudes between the two gyre (38°N-42°N), referred to as the gyre-gyre boundary, the meridional connection between the two gyres is ambiguous, casting doubt on a strong inter-gyre connection for these transports.

Cross-correlation coefficients between UNADW transport time series at 53°N and the same time series at other latitudes are shown in Figure 37. At all subpolar

latitudes, significant 0-lag correlations are present, indicating in-phase gyre-scale variability. However, for all three models the positive correlations drop dramatically at the gyre-gyre boundary and essentially disappear south of 35°N, indicating either that UNADW transport anomalies do not propagate to the subtropical gyre or that the propagated anomalies are too weak to impact local transport.

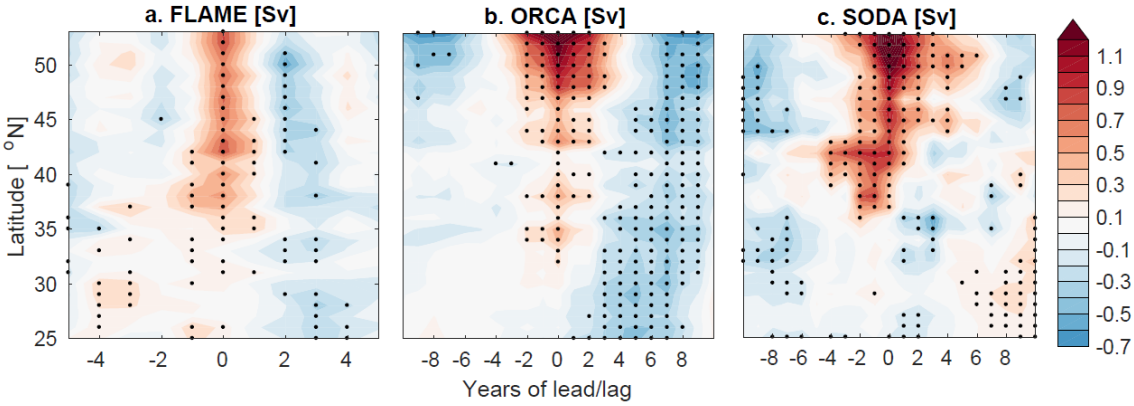

Figure 37: Cross-correlation between normalized UNADW layer transport time series at 53°N and the transport time series at other latitudes. Shaded in color is the correlation coefficient times the standard deviation of the layer transport at each latitude (unit: [Sv]). Negative years indicate that the 53°N time series are leading. Black dots indicate the correlations are significant at 95% confidence level. (a) In FLAME. (b) In ORCA025. (c) In SODA.

Next I conduct a similar assessment for LNADW. In this case, the correlation plots appear similar to those for AMOC anomalies: significant correlations are found not only within the subpolar gyre, but also in the subtropical gyre, where transports lag those at 53°N by less than 4 years (Figure 38a-b for FLAME and ORCA025). However, because the correlations are weak (particularly for ORCA025) near the gyre-gyre boundary, a coherent propagation of LNADW transport anomalies from the subpolar

gyre to the subtropical gyre appears unlikely. As for the results in SODA, though a significant correlation is also found between LNADW transport in the subtropical and the subpolar gyres (not shown), the anomalies in the subtropical gyre are so strong that they cannot be traced back to the subpolar gyre, where transport anomalies are quite weak (Figure 35). Instead, these anomalies appear to be generated at the gyre-gyre boundary, where they are of maximum strength.

Though weak, the potential for an inter-gyre connection for LNADW anomalies warrants further investigation, particularly into whether this connection is contingent on the strength of the transport anomalies. In FLAME, LNADW transport variability in both gyres is dominated by strong anomalies in the 1990s (Figure 33), which are also captured by ORCA025 (Figure 34). These strong anomalies, which appear to originate in the subpolar gyre, exhibit a relatively coherent southward spreading compared to anomalies in other years, raising the possibility that this time period alone is responsible for the connection of LNADW transports in the subtropical gyre with those in the subpolar gyre (Figure 38a-b). To test this possibility, I re-calculate the correlation coefficient between transports at 53°N and at other latitudes in the LNADW layer in ORCA025 from 1961 to 1989 only (Figure 38c). Interestingly, no significant positive correlation is observed south of 45°N. To ensure that this lack of correlation is due to the exclusion of the 1990s event instead of the shortening of the time series, I repeat the calculation with time series from 1976 to 2004, which has a similar temporal span but

now includes the 1990s event. The cross-correlation map is very similar to Figure 38b, except that the correlations are much stronger. Collectively, these analyses indicate that while a southward propagation from the subpolar to the subtropical gyre is possible for strong transport anomalies, there is, in general, a lack of inter-gyre connection for LNADW transport anomalies generated in the subpolar gyre.

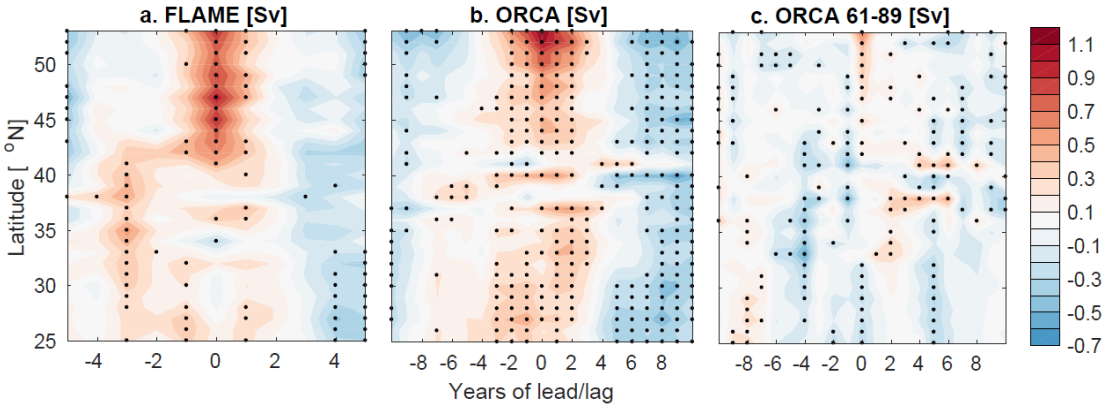

Figure 38: Cross-correlation between normalized LNADW layer transport time series at 53°N and transport time series at other latitudes. (a) In FLAME. (b) In ORCA025. (c) In ORCA025, but only with time series from 1961 to 1989.

4.5 Relationship between deep water transport and AMOC

I now turn to the second part of this study, namely a study of the relationship between local (i.e. at the same latitude) AMOC variability and local deep water transport variability. In the subpolar gyre, UNADW and LNADW transport variabilities are both strongly and positively correlated with AMOC variability (Figure 39). The UNADW and LNADW relationships to AMOC are comparable in FLAME (Figure 39a), as expected since the strong subpolar AMOC anomaly in the 1990s appears in both layers (Figure 33).

In the subpolar gyre, in ORCA025 and SODA, the relationship between AMOC and UNADW is much stronger than that between AMOC and LNADW (Figure 39b-c), suggesting a dominant role of UNADW. This is especially true in SODA, where the subpolar LNADW transport anomalies are quite weak (Figure 35).

In the subtropical gyre (Figure 39, gray boxes), all models exhibit weak and insignificant correlations between AMOC variability and UNADW variability. In contrast, LNADW variability is strikingly similar to AMOC variability. In particular, the LNADW transport variability is stronger than AMOC variability in ORCA025 and SODA, where the UNADW and LNADW transport anomalies are anti-correlated. Thus, consistent with the RAPID observations, it appears that AMOC variability in the subtropical gyre is expressed in the LNADW layer. Considering that most of the transport anomalies in the LNADW layer do not originate from the subpolar gyre (section 4.4), it is concluded that those anomalies are either generated in the subtropical gyre, or imported from the gyre-gyre boundary.

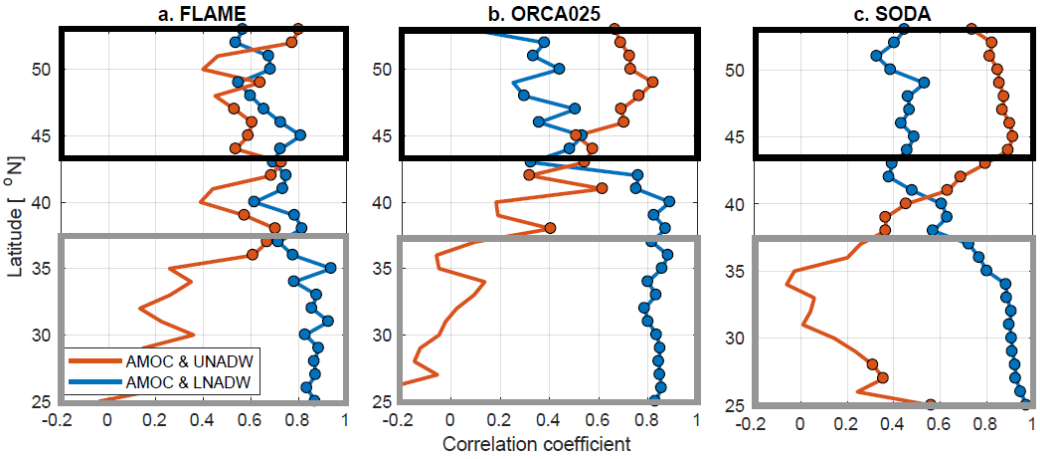

Figure 39: Correlation coefficients between AMOC and layer transport across latitudes. (a) In FLAME. (b) In ORCA025. (c) In SODA. Colored circles indicate that the correlations are significant at 95% confidence level. Black (gray) boxes indicate the subpolar (subtropical) gyre.

4.6 Summary and discussion

With output from two ocean circulation models and one ocean reanalysis, I test the causal linkage between water mass transport and AMOC by focusing on: (1) the meridional connection of UNADW/LNADW transport anomalies; and (2) the linkage between these deep water transports and AMOC strength.

Though subpolar UNADW transport anomalies are related to local AMOC changes on interannual to decadal time scales, these transport anomalies, regardless of strength, do not propagate coherently from the subpolar to the subtropical gyre, nor do they impact the subtropical AMOC strength. Thus, LSW production signals do not appear to result in meridionally coherent AMOC changes via an UNADW transport response.

The lack of meridional coherence in transport anomalies is also evident in the LNADW layer. An exception to this generality is that, strong anomalies are likely to be communicated to the subtropical gyre, where they have the potential to influence the local AMOC strength. Despite this tenuous downstream connectivity for LNADW transport anomalies, a significant linkage between LNADW transport and local AMOC strength is present at all latitudes, and the linkage strengthens from high to low latitudes. In fact, most of the AMOC variability in the subtropical gyre is explained by LNADW transport variability, consistent with observations from RAPID.

This modeling study has placed the intriguing LNADW variability at RAPID in a larger spatial and temporal context. That context reveals that LNADW dominance in the subtropical gyre is not similarly attained in the subpolar gyre, where both deep water masses contribute to AMOC variability. Additionally, this study explains why the UNADW contribution to AMOC variability in the subtropical gyre is so weak, namely that there is no clear pathway for UNADW transport anomalies from the subpolar to the subtropical gyre.

Continued observations from the RAPID array as well as those from recently deployed OSNAP (Lozier, et al., 2016) will aid more complete assessment of AMOC's response to deep water mass formation in both the subtropical and subpolar basins.

Of note is that this modeling study leaves open the question as to why and how LNADW transport variability dominates the signal of AMOC variability in the

subtropics. The different responses in layer transport are possibly related to the impact of the bottom pressure torque (BPT) on these transports. The connection of the AMOC to the wind-driven barotropic circulation through BPT has been recently established by Yeager (2015). Specifically, wind stress curl (WSC) variability prompts a BPT response, which is balanced by planetary vorticity changes in the deep ocean, leading to subsequent changes of the meridional flow. The role of the BPT is largest in the LNADW layer, where the LNADW transport core interacts with the sloping topography. BPT's role in the UNADW layer, on the other hand, is likely much weaker, if it exists at all, since the UNADW transport core is not closely attached to the western boundary. Instead, LNADW transport variability is more likely controlled by Ekman pumping variability and the resultant gyre-scale adjustment via Rossby waves. A similar linkage between BPT and WSC is expected in the subpolar gyre, but there buoyancy forcing may impact deep water transports to a greater degree by modifying the density gradient across the basin. Further analysis is required to address this interesting observation.

5. Ongoing Research

5.1 Decomposing the AMOC variability

5.1.1 Introduction

As stated above, decadal AMOC variability has been linked to buoyancy forcing in the subpolar and subarctic regions, where the deep waters are formed (Delworth, et al., 1993; Latif, et al., 2006; Zhang, 2010; Yeager & Danabasoglu, 2014). Modeling studies have suggested that these AMOC anomalies are communicated to tropical latitudes by advection (Marotzke & Klinger, 2000; Buckley, et al., 2012), boundary waves (Biastoch, et al., 2008; Eden & Willebrand, 2001; Häkkinen, 1999), or both (Zhang, 2010; Getzlaff, et al., 2006), and that these anomalies generated at high latitudes dominate local AMOC changes on decadal time scales (Buckley, et al., 2012; Polo, et al., 2014; Pillar, et al., 2016).

These decadal signals, however, are masked by high frequency, wind-driven AMOC variability at subtropical latitudes (Biastoch, et al., 2008; Cabanes, et al., 2008; Roberts, et al., 2013; Zhao & Johns, 2014; Polo, et al., 2014), leading to latitudinal incoherency in AMOC variability between the subpolar and the subtropical gyres. For example, with a range of ocean models, Bingham et al. (2007) evaluate AMOC meridional coherence in depth space and find that the subpolar AMOC is dominated by decadal variability, while the subtropical AMOC primarily varies on interannual time scales. Using a data-assimilated numerical model, Lozier et al., (2010) find opposing decadal changes in AMOC between the subpolar and the subtropical gyres. They

conclude that these gyre-specific changes are a result of gyre dynamics that take place on interannual to decadal time scales.

A further look at the meridional coherence in AMOC vertical structure is provided by Cabanes et al. (2007). Using an assimilation product (1993-2003), the authors apply an Empirical Orthogonal Function (EOF) analysis to the overturning streamfunction. They show that the dominant overturning mode maximizes south of 40°N and that the time series for this mode correlated with the NAO. Though this overturning mode extends to the subpolar gyre, the strength is much reduced. This pattern is possibly due to an underestimation of AMOC variability in depth space at high latitudes (Zhang, 2010), and a time period of study that is insufficient to cover the full range of variability in the subpolar AMOC.

In summary, despite a focus of the AMOC community in recent years, the extent to which AMOC signals are connected between gyres remains an open question. Furthermore, the meridional coherence in the vertical structure of the overturning is unclear.

In this Chapter, the latitudinal AMOC (calculated in density space) variability is decomposed with EOF analysis in two ocean circulation models (FLAME and ORCA025) and two ocean reanalysis datasets (SODA3 and ECCO4). A meridionally coherent mode and a gyre-specific mode are detected. Their variability and driving mechanisms are discussed.

5.1.2 Data and methods

For this study, I use two ocean circulation models, FLAME and ORCA025. The details of these models can be found in sections 3.3.4 and 2.2.2.

I also use two reanalysis datasets for this analysis. The first dataset is SODA3.4.2, an updated version of SODA2 (see section 4.2.1), but based on GFDL MOM5/SIS model (1/4°x1/4°x50level). The model is forced with ERA-Interim reanalysis and uses COARE4 bulk formula. The data spans from 1980 to 2015.

The second dataset is Estimating the Circulation and Climate of the Ocean (ECCO Version 4 Release 3, or ECCOv4r3). The underlying model for ECCO is Massachusetts Institute of Technology (MIT) Ocean GCM (Marshall, et al., 1997), with a spatial resolution ranging from 22km to 110km and 46 vertical levels. The model synthesizes satellite and in situ data to produce an estimate of the ocean circulation from 1992 to 2015.

The calculation of AMOC in density space is the same as the one described in section 4.2.2.

5.1.3 The meridionally coherent mode and gyre-specific mode for AMOC variability

With EOF analysis, I decompose the latitudinal AMOC variability into two modes (Figure 40). With the trend removed, EOF1 (50%) in all datasets detects a meridionally coherent mode of AMOC variability. This mode maximizes in the subpolar

gyre and decreases towards low latitudes. Interestingly, the time series for this mode do not have a significant dominant frequency on decadal time scales (Figure 41).

EOF2 (20-30%) reveals a gyre-specific mode with AMOC strength in the subpolar gyre out-of-phase with that in the subtropical gyre. Power spectral analysis of the time series for this mode does not reveal a dominant frequency in general, except for a significant period of 4 years in SODA.

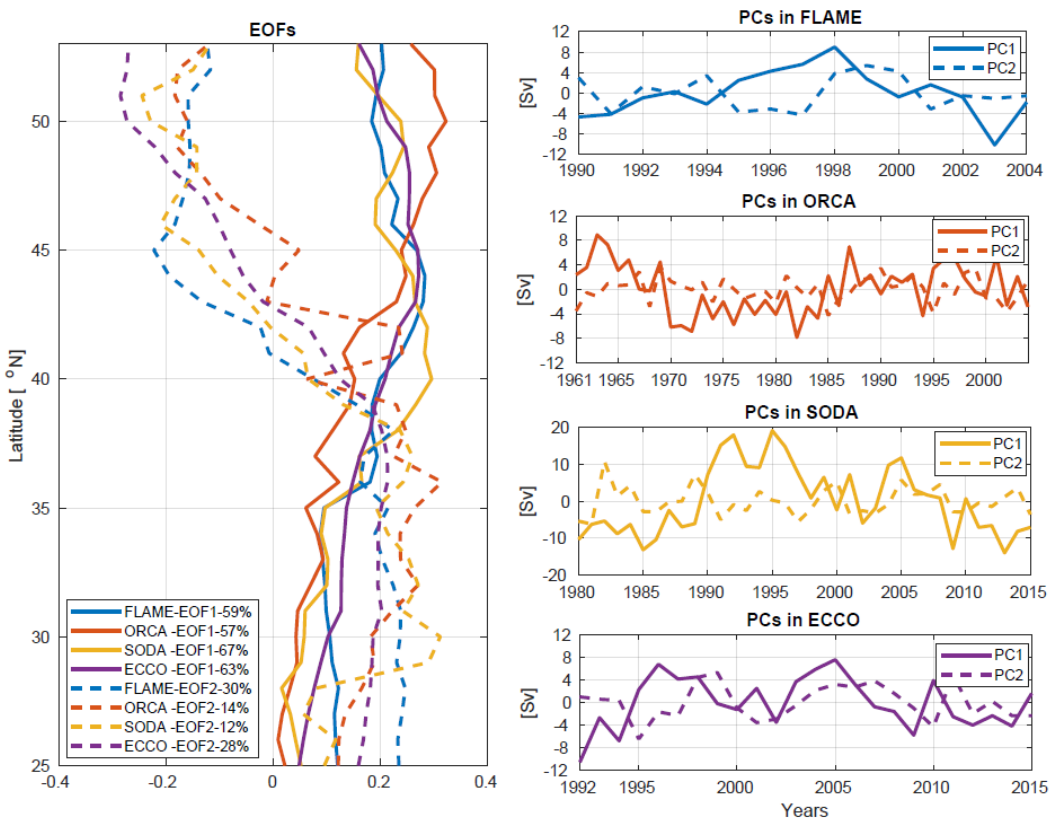

Figure 40: EOFs and PCs for detrended AMOC variability in different data sets.

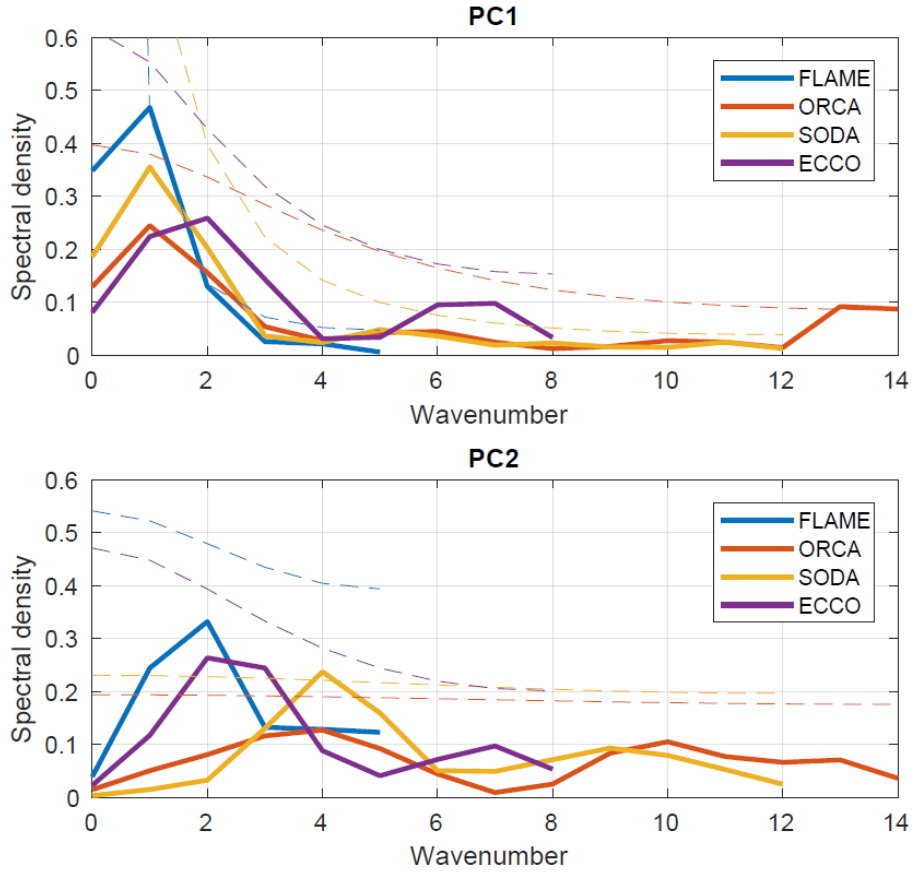

Figure 41: Power spectral density for PCs as a function of wavenumber. (Upper) For PC1. (Lower) For PC2. Dashed lines represent 95% confidence upper limit of red noise spectrum.

5.1.4 Transition latitudes as a key region to detect a meridionally coherent AMOC mode

At the transition latitudes near the gyre-gyre boundary (40-45°N), where EOF2 reverses signs (i.e. EOF2=0), AMOC variability can be reconstructed from the first mode only (Figure 42), suggesting this location as the key region to detect the meridionally coherent mode of AMOC variability.

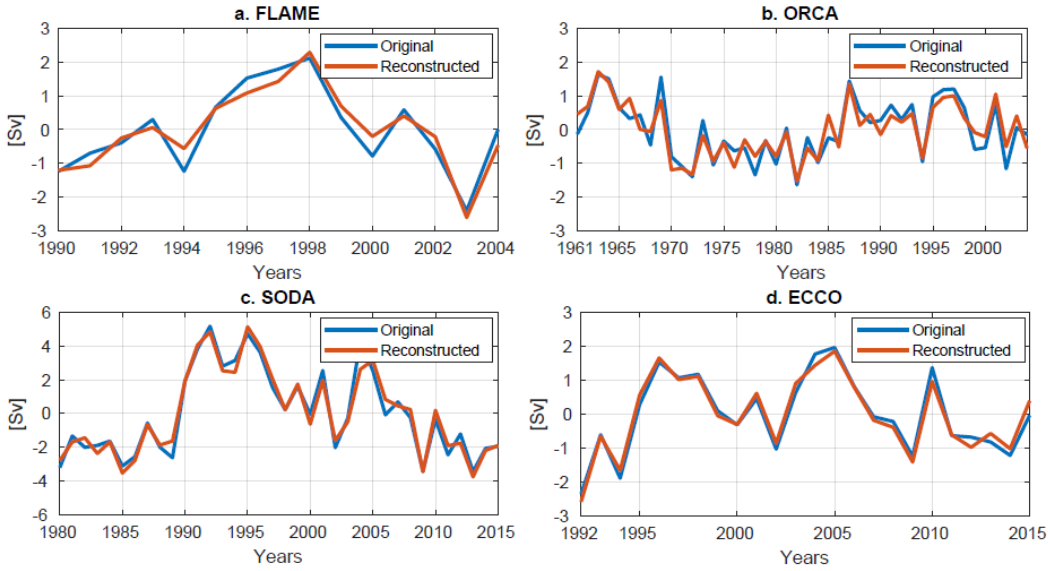

Figure 42: A comparison between original AMOC and reconstructed AMOC time series at the transition latitudes. The original time series of detrended AMOC averaged over the transition latitudes (40-45°N) are shown in blue. The time series of reconstructed AMOC from EOF1 (i.e. EOF1 at transition latitudes * PC1) are shown in orange.

5.1.5 Linkage between gyre-specific AMOC and wind stress

To understand the mechanism of different AMOC modes, I focus in this section on the gyre-specific mode and regress the PC2 onto local wind stress fields. The regression map shows an NAO-like pattern.

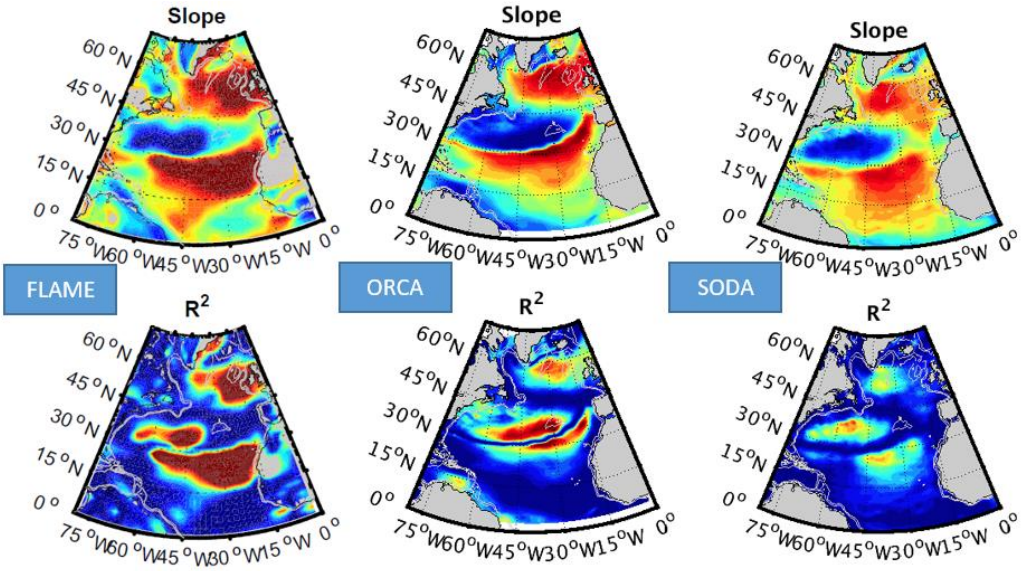

Figure 43: Linkage between the gyre-specific mode and wind stress. (Upper) Regression of AMOC PC2 onto the detrended wind stress in FLAME, ORCA025 and SODA. (Lower) R^2 for each regression.

5.1.6 Next steps

The driving mechanism for EOF1 will be examined. The hypothesis is that either buoyancy forcing, or wind forcing, or both in the subpolar gyre dominates PC1 variability, and that this signal propagates to the tropical latitudes with a weakening magnitude. I will also explore the vertical structure of the overturning streamfuntion for the two modes.

5.2 The contradiction between LSW property propagation and its advection

5.2.1 Introduction

The propagation of LSW from its formation site to the subtropical gyre has been based on correlations between LSW layer properties in the Labrador Sea and at downstream location. For example, Molinari et al. (1998) found the arrival of recently formed LSW, with low salinity and temperature anomalies, from the Labrador Sea to 26.5°N in the DWBC (the Abaco region) within 10 years. Curry et al. (1998) found a 6-year transit time of the LSW layer signal from the Labrador basin (detected using LSW thickness) to the interior western subtropical gyre near Bermuda region (LSW temperature anomalies). Moreover, with a high-resolution model, van Sebille et al. (2011) reported a 9-year propagation time scale of LSW salinity anomalies from the Labrador Sea to the western subtropics through both DWBC and interior pathways, and concluded that "decadal classical LSW anomalies stay relatively coherent while getting advected, despite the important role of interior pathways".

The relationship of LSW layer property anomalies between the Labrador Sea and the western subtropical gyre identified by the above studies is based on the assumption that both DWBC and interior pathways are advecting LSW southward effectively within a decade. Bolstering this assumption, Lagrangian modeling studies have shown that the swiftly-moving DWBC is able to carry newly formed LSW to the subtropical gyre within a decade (Zou & Lozier, 2016; Gary, et al., 2012). However, observational and modeling

studies have shown that the DWBC carries only a small portion of newly-formed LSW (Bower, et al., 2009; Lavender, et al., 2005; Gary, et al., 2012; Zou & Lozier, 2016) and is only responsible for the intermediate layer property anomalies within the western boundary (e.g. the Abaco region). Property variability in the interior of the subtropical gyre, e.g. in the vicinity of Bermuda, remains unexplained for this reason: the advective time scale for the interior pathways that connect the Labrador Sea to the interior subtropical gyre at 30°N exceeds 20 years (Zou & Lozier, 2016; Rhein, et al., 2015), which is in contrast to the observed 10-year lagged correlation in property anomalies. This discrepancy raises the question as to whether or not the Labrador Sea is the primary origin of the LSW layer property anomalies in the western subtropical gyre.

In this ongoing study, I am investigating the driving mechanism of the 10-year relationship between LSW salinity in the Labrador Sea and in the western subtropical gyre.

5.2.2 Data and methods

The observational dataset EN4 (version 4.1.1) from Met Office Hadley Center (ref) is used in this study. Specifically, I am using the monthly objective analyses formed from the quality controlled subsurface ocean temperature and salinity profiles with Gouretski and Reseghetti (2010) corrections. As I am interested in interannual to decadal variability of LSW layer salinity changes, the monthly data is averaged over each year from 1961 to 2014 to obtain annual mean data. The data has a spatial resolution of 1°×1°

and 42 vertical layers with grid spacing increasing from 10m near the surface to 300m at the bottom. More information on the dataset can be found at http://www.metoffice.gov.uk/hadobs/en4/.

A global ocean/sea ice model ORCA025 at eddy-permitting resolution (1/4°) is also used in this study. For model details, please refer to section 2.2.2.

For the EN4 dataset, I follow the definition of the LSW layer used in van Sebille et al. (2011) as the water within the density range of $36.82 \leq \sigma_2 \leq 36.97\ kg/m^3$ (corresponding to $27.74 \leq \sigma_0 \leq 27.80\ kg/m^3$). For ORCA025, since its LSW is saltier and denser compared to observations, I use the density of $36.82 \leq \sigma_2 \leq 36.98\ kg/m^3$ to define the LSW layer in the model. This density range corresponds to $27.75 \leq \sigma_0 \leq 27.84\ kg/m^3$ in ORCA025 and has been shown to cover the LSW layer identified with minimum potential vorticity in the Labrador Sea and near the boundary between the subpolar gyre and the subtropical gyre (Zou & Lozier, 2016). Unless specified, the properties within the LSW layer at each grid are averaged vertically over the defined density range.

5.2.3 The role of eddies

With output from EN4 and ORCA025, I calculate the cross-correlation between the LSW salinity in the Labrador Sea and that in the North Atlantic. Similar to previous studies, I find significant correlation between the Labrador Sea and the western subtropical gyre, with the latter lagging by ~10 years (Figure 44). Interestingly, the LSW layer salinity variability in the eastern subpolar gyre, especially around the Rockall

Plateau, is also significantly related to the salinity in the Labrador Sea, also with ~10 years lag. This simultaneous variation of LSW salinity is further illustrated in Figure 45, where 0-lag correlation is seen in the region from the western subtropical gyre to the eastern subpolar gyre. The region aligns with an anti-cyclonic circulation at the mid-latitudes, which is shown to be driven by eddies (Figure 46) (Lozier, 1997).

Next I track the LSW from the western subtropical gyre backward in time with synthetic Lagrangian floats. Within 10 years, most of the floats can be traced back to the central and eastern North Atlantic by following the anti-cyclonic circulation, with very few from the Labrador Sea (Figure 47).

These findings highlight a possibility that the "10-year lagged correlation" in the LSW layer between the Labrador Sea and the western subtropical gyre is due to eddy-induced mixing between the subpolar and the subtropical gyre, instead of a coherent propagation of LSW from the subpolar gyre to the subtropical gyre. It is hypothesized that the eddies act to mix the fresh waters from the Labrador Sea and the salty waters

from the Mediterranean Outflow Water (MOW), and creates simultaneous salinity variability within the recirculating gyre.

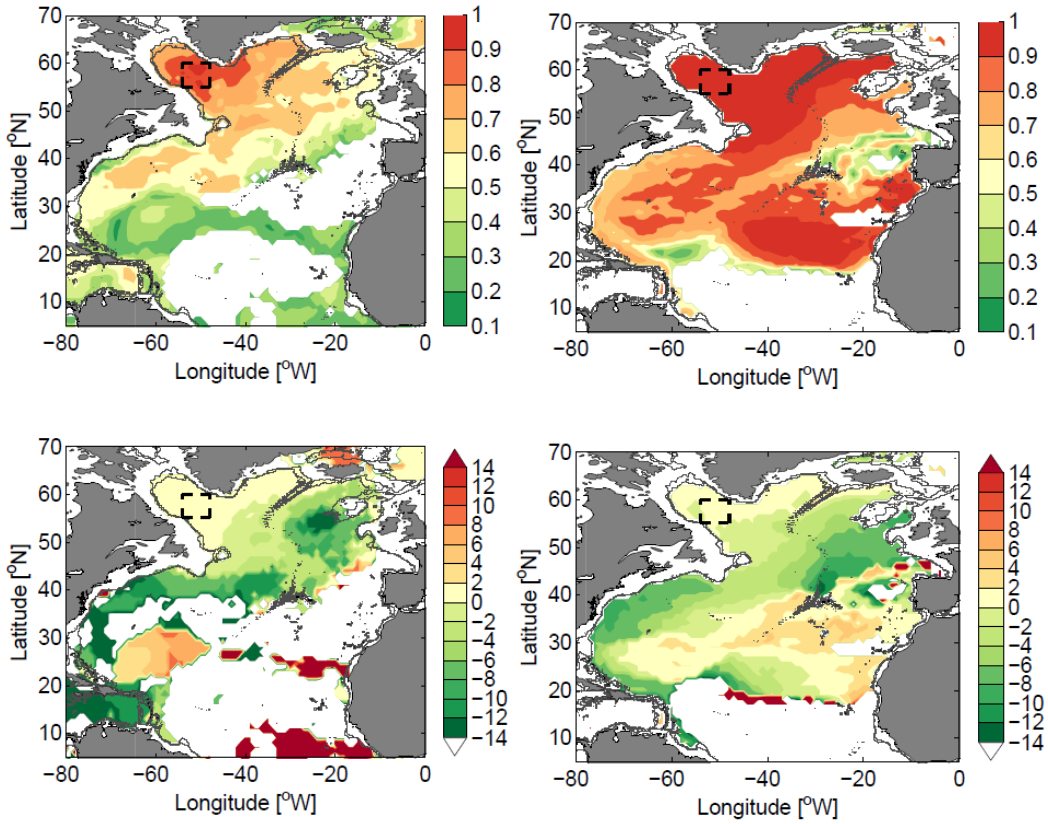

Figure 44: Maximum cross-correlation of LSW salinity between Labrador Sea and the North Atlantic. The time series of LSW salinity in the Labrador Sea are averaged within the black dashed box. The upper two plots show correlation coefficients from EN4 (left) and ORCA025 (right). The lower panels indicate the years of lead (negative) or lag (positive) when the maximum coefficients in the upper panels are reached.

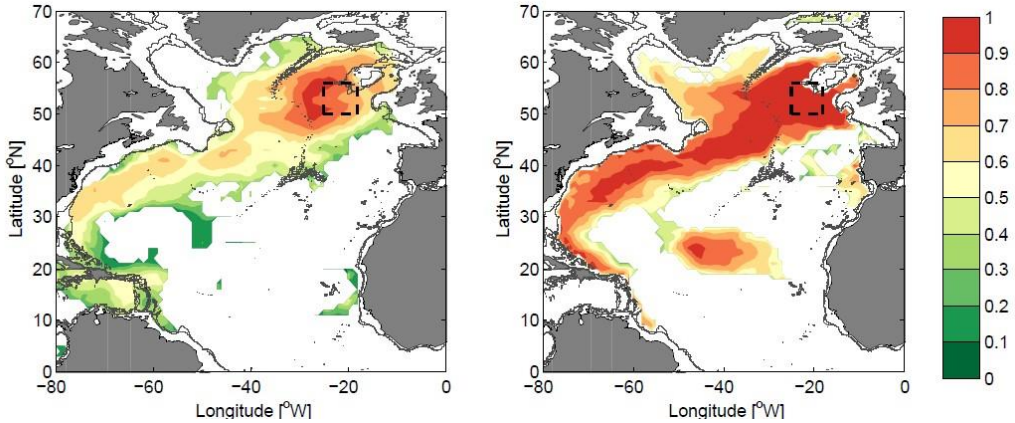

Figure 45: Significant correlation coefficients between LSW layer salinity south of Rockall Plateau (black dashed box) and the North Atlantic at no lead/lag. (Left) In EN4. (Right) In ORCA025.

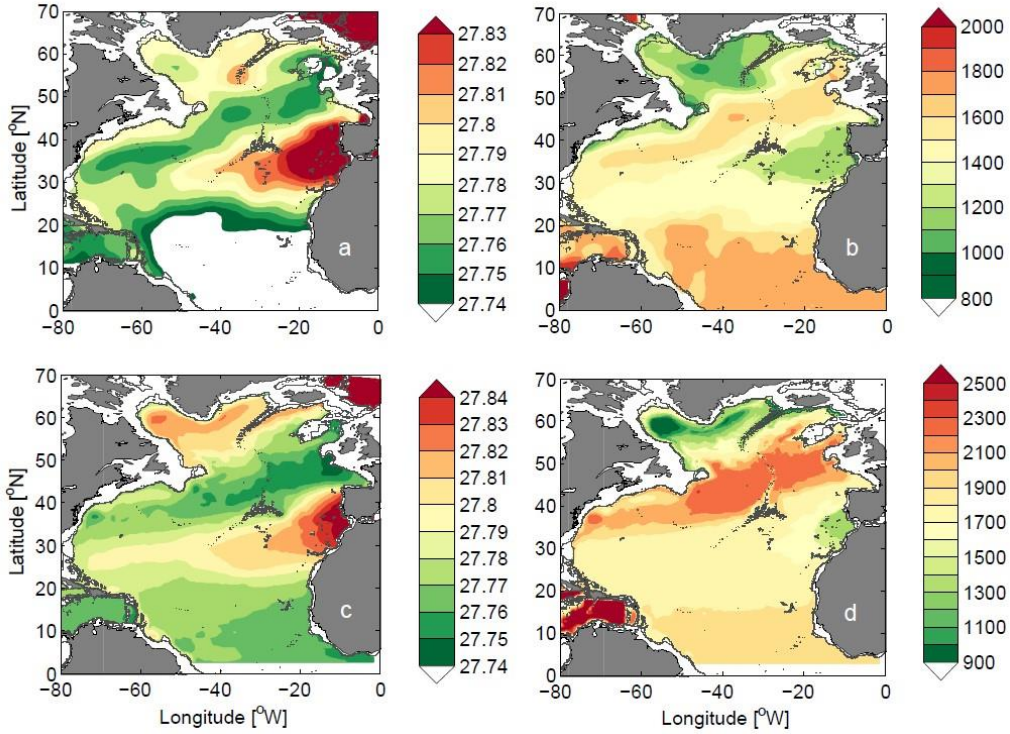

Figure 46: Geostrophic structure in LSW layer in the North Atlantic. Climatological potential density field on isobars of 1650 dbar from EN4 (a) and ORCA025 data (c). Climatological pressure field within LSW layer density surfaces from EN4 data (b) and ORCA025 data (d). All these plots indicate the geostrophic

structure at intermediate depth of the North Atlantic, i.e. a cyclonic circulation around the Labrador and Irminger Seas and an anti-cyclonic circulation extended from the western subtropical gyre to the eastern subpolar gyre.

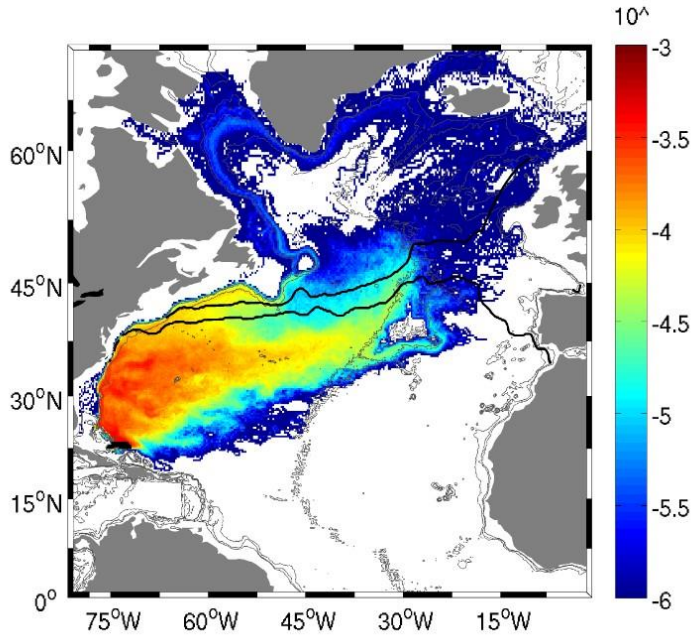

Figure 47: Probability map of 10-year backward trajectories of floats launched in the LSW layer within DWBC at 23°N. The initial launch locations are indicated in black short line. ORCA025 data is used to compute the trajectories.

5.2.4 Next steps

I will use climate models, which are coarse in resolution and do not resolve eddies, to repeat the above analysis. If the LSW salinity variability in the extended region is driven by eddies, then in these climate models, the 10-year lagged correlation in LSW salinity between the extended region and the Labrador Sea would be reduced or even missing.

Next I will calculate the residence time of LSW within the anti-cyclonic gyre (i.e. from the time when LSW enters the gyre to the time when it reaches the western

subtropical gyre). If the residence time of LSW within the gyre is on the order of ~10 years, it is expected that the 10-year relationship is created by eddies.

6. Conclusions

In this dissertation, I investigated the relationship between the production of NADW and AMOC by detailing the processes and linkages involved.

I first explored the relationship between LSW production and the AMOC (Figure 48). In an eddy-permitting model, it is shown that on interannual to decadal time scales, LSW export variability from the subpolar to the subtropical gyre is not driven by LSW production variability in the Labrador Sea (Chapter 2). This is attributed to the strong recirculation of LSW, as well as the mixing and stirring along the export pathways that minify the impact of LSW production. This conclusion also suggests a negligible or at best modest impact of LSW production on the subtropical AMOC.

With two ocean models and one ocean reanalysis dataset, a follow-on study specifically explores the relationship between the cross-basin transport in LSW (or UNADW) layer and AMOC across latitudes. Despite the driving mechanism, the LSW transport anomalies in the subpolar gyre, important in maintaining the subpolar AMOC anomalies, do not propagate coherently to the subtropical gyre, and thus contribute negligibly to subtropical AMOC anomalies (Chapter 4).

The analysis is then extended to the relationship between OW and AMOC (Figure 49). The amount of OW across the ridge into the North Atlantic has been observed to be quite steady over the past five decades, indicating that any OW-related AMOC changes have to be produced by the processes south of the ridge. Unlike LSW,

the spreading pathways of OW have been much less observed and studied, especially from a Lagrangian perspective. With observational data and an eddy-resolving ocean circulation model, I have provided a comprehensive description of the ISOW spreading pathways in the eastern North Atlantic from both Lagrangian and Eulerian perspectives (Chapter 3). I also presented a first look at the temporal interplay of different ISOW branches and highlight the impact of upper ocean dynamics on those deep pathways.

The relationship between the cross-basin transport of OW (in the LNADW layer) and the AMOC is discussed in Chapter 4. In the subpolar gyre, OW transport anomalies are linked to local AMOC anomalies, though this linkage is overall weaker compared to the linkage between LSW and AMOC. The subpolar-originated OW transport anomalies do not generally reach the subtropical gyre, unless the anomaly is strong enough (e.g. the OW anomaly in the 1990s). In the subtropical gyre, AMOC variability is mostly driven by wind-forced upper ocean dynamics, and the compensating variability in the AMOC lower limb is contained primarily in the OW layer, rather than the LSW layer (consistent with observations at 26.5°N).

Finally, to explore the extent to which AMOC signals are connected between the subpolar gyre and the subtropical gyre, I used an EOF analysis to decompose the latitudinally-dependent AMOC in two ocean circulation models and two reanalysis datasets. A meridionally coherent mode of AMOC variability is detected, but this mode decreases significantly towards the subtropical gyre. A gyre-specific mode is also

revealed with AMOC strength in the subpolar gyre out-of-phase with that in the subtropical gyre. The time series of this mode is linked to an NAO-like wind stress pattern. At the gyre-gyre boundary, where the gyre-specific mode is missing, AMOC variability can be reconstructed from the coherent mode only, suggesting this location as the key region to detect the meridionally coherent AMOC variability. An ongoing study will focus on the vertical structure of the overturning streamfunction for these two modes.

In summary, this dissertation critically assesses the linkage between deep water formation and the AMOC by exploring the key processes involved. It also sheds light on the vertical structure and meridional coherence of AMOC variability across the North Atlantic.

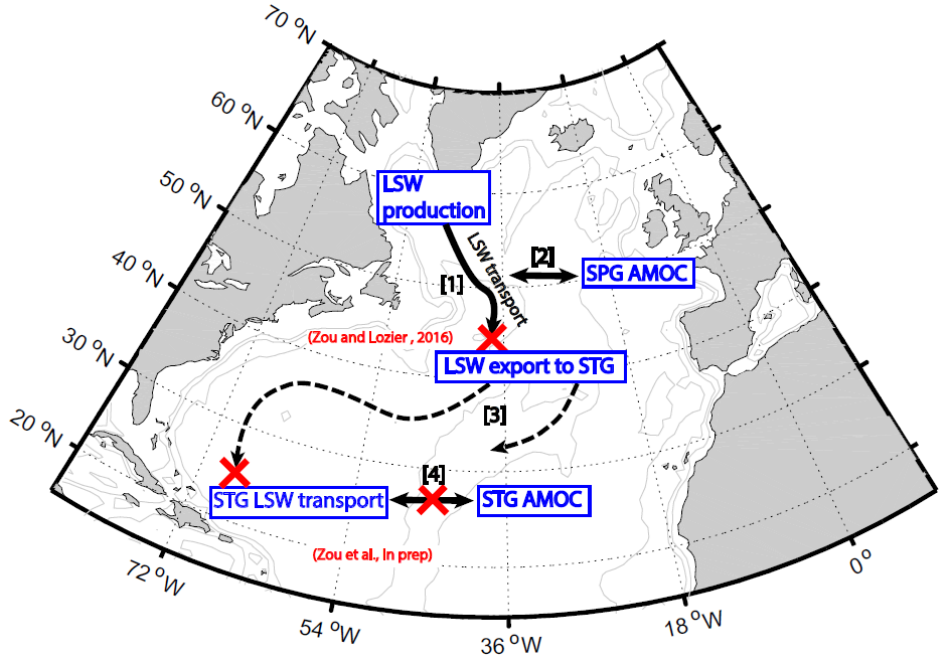

Figure 48: A research summary of the relationship between LSW production, LSW export and the AMOC. [1] LSW production does not dominate LSW export from the subpolar to the subtropical gyre. [2] LSW transport in the subpolar gyre is related to subpolar AMOC strength. [3] LSW transport signals from the subpolar gyre do not propagate coherently to the subtropical gyre, i.e. they have negligible impact on subtropical LSW transport. [4] LSW transport in the subtropical gyre is not correlated with local AMOC strength.

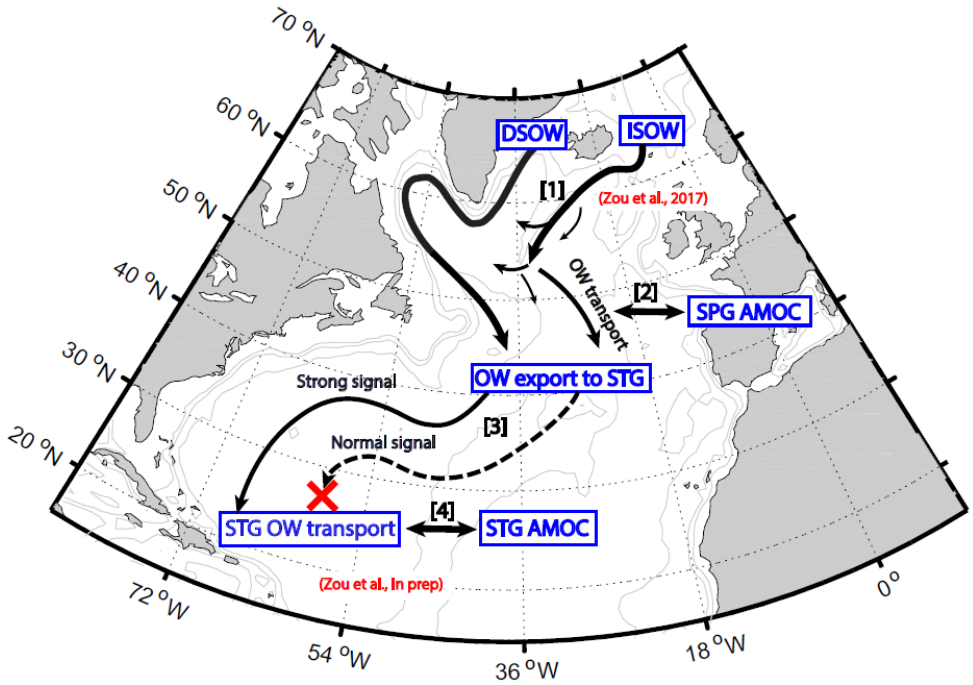

Figure 49: A research summary of the ISOW spreading pathways and the linkage between OW and AMOC. [1] The spreading pathways of ISOW in the eastern North Atlantic. [2] OW transport in the subpolar gyre is correlated with subpolar AMOC strength. [3] Only strong OW transport anomalies propagate coherently from the subpolar to the subtropical gyre; normal-strength OW anomalies do not reach the subtropical gyre. [4] Subtropical OW transport is linked to subtropical AMOC strength, and both are driven by local wind forcing.

References

Beaird, N. L., Rhines, P. B. & Eriksen, C. C., 2013. Overflow Waters at the Iceland–Faroe Ridge Observed in Multiyear Seaglider Surveys. *Journal of Physical Oceanography* , 43(2334-2351).

Berliand, M. & Strokina, T., 1980. Global distribution of the total amount of clouds. Hydrometeorological, Leningrad, 71.

Bernard, B. et al., 2006. Impact of partial steps and momentum advection schemes in a global ocean circulation model at eddy permitting resolution. *Ocean Dynamics,* Volume 56, p. 543–567.

Biastoch, A. et al., 2008. Causes of Interannual-Decadal Variability in the Meridional Overturning Circulation of the Midlatitude North Atlntic Ocean. *J. of Climate,* , Volume 21, pp. 6599-6615.

Bingham, R., Hughes, C., Roussenov, V. & Williams, R., 2007. Meridional coherence of the North Atlantic meridional overturning circulation. *Geophysical Research Letters,* 34(23).

Blanke, B. & Grima, N., 2010. ARIANE v2.2.6. Laboratoire de Physique des Oceans.

Böning, C. W. et al., 2006. Decadal variability of subpolar gyre transport and its reverberation in the North Atlantic overturning. *Geophysical Research Letters,* Volume 33.

Bower, A., Lozier, M., Gary, S. & Böning, C., 2009. Interior pathways of the North Atlantic meridional overturning circulation. *Nature,* , Volume 459, pp. 243-247.

Bower, A. S. et al., 2002. Directly measured mid-depth circulation in the northeastern North Atlantic Ocean. *Nature* , 419(6907), pp. 603-607.

Bower, A. S. & Furey, H., 2017. Iceland-Scotland Overflow Water transport variability through the Charlie-Gibbs Fracture Zone and the impact of the North Atlantic Current. *Journal of Geophysical Research: Oceans.*

Buckley, M. et al., 2012. On the relationship between decadal buoyancy anomalies and variability of the Atlantic meridional overturning circulation. *Journal of Climate,* , 25(23), pp. 8009-8030.

Burkholder, K. C. & Lozier, M. S., 2011. Subtropical to subpolar pathways in the North Atlantic: Deductions from Lagrangian trajectories. *Journal of Geophysical Research* , Volume 116.

Cabanes, C., Lee, T. & Fu, L., 2008. Mechanisms of interannual variations of the meridional overturning circulation of the North Atlantic Ocean. *Journal of Physical Oceanography,* 38(2), pp. 467-480.

Carbon Dioxide International Analysis Center, 2015. *Subset used: 1992-2004, accessed 29 January 2015..*

Carton, J. & Giese, B., 2008. A reanalysis of ocean climate using Simple Ocean Data Assimilation (SODA). *Monthly Weather Review,* , 136(8), pp. 2999-3017.

Center, N. N. W. S. C. P., n.d. cited 2015: NOAA/ National Weather Service Climate Prediction Center. Subset used: December 1960 – March 2004..

CERSAT, 2002. Mean Wind Fields (MWF product) Volume 1 – ERS-1, ERS-2 & NSCAT User Manual. Ref C2-MUT-W-05-IF, Version 1.0. Department of Oceanography from Space, Ifremer.

Chang, Y. S., Garraffo, Z. D., Peters, H. & Özgökmen, T. M., 2009. Pathways of Nordic Overflows from climate model scale and eddy resolving simulations. *Ocean Modelling* , Volume 29, pp. 66-84.

Curry, R., McCartney, M. & Joyce, T., 1998. Oceanic transport of subpolar climate signals to mid-depth subtropical waters. *Nature,* Volume 391, pp. 575-577.

Delworth, T., Manabe, S. & Stouffer, R., 1993. Interdecadal variations of the thermohaline circulation in a coupled ocean-atmosphere model. *Journal of Climate,,* 6(11), pp. 1993-2011.

Dengler, M., Fischer, J., Schott, F. & Zantopp, R., 2006. Deep Labrador Current and its variability in 1996–2005. *Geophysical Research Letters,* Volume 33.

Dickson, R. R. & Brown, J., 1994. The production of North Atlantic Deep Water: Sources, rates, and pathways. *Journal of Geophysical Research* , 99(12319).

Eden, C. & Willebrand, J., 2001. Mechanism of interannual to decadal variability of the North Atlantic circulation. *Journal of Climate,* 14(10).

Eldevik, T. et al., 2009. Observed sources and variability of Nordic seas overflow. *Nature Geoscience,* Volume 2, pp. 406-410.

Ellett, D. J. & Roberts, D. G., 1973. The overflow of Norwegian sea deep water across the Wyville-thomson Ridge. *Deep Sea Research and Oceanographic Abstracts,* 20(819-835).

Fischer, J., Visbeck, M., Zantopp, R. & Nunes, N., 2010. Interannual to decadal variability of outflow from the Labrador Sea. *Geophysical Research Letters,* Volume 37.

Fleischmann, U., Hildebrandt, H., Putzka, A. & Bayer, R., 2001. Transport of newly ventilated deep water from the Iceland Basin to the Westeuropean Basin. *Deep Sea Research Part I: Oceanographic Research Papers,* Volume 48, pp. 1793-1819.

Frajka-Williams, E. et al., 2016. Compensation between meridional flow components of the Atlantic MOC at 26°N. *Ocean Science,* 12(2), p. 481.

Gary, S., Lozier, M., Biastoch, A. & Böning, C., 2012. Reconciling tracer and float observations of the export pathways of Labrador Sea Water. *Geophysical Research Letters,* 39(24).

Gary, S., Lozier, M., Böning, C. & Biastoch, A., 2011. Deciphering the pathways for the deep limb of the Meridional Overturning Circulation. *Deep-Sea Research II,* Volume 58, pp. 1781-1797.

Getzlaff, K., Böning, C. W. & Dengg, J., 2006. Lagrangian perspectives of deep water export from the subpolar North Atlantic. *Geophysical research letters* , 33(21).

Goosse, H., 1997. Modeling the large scale behaviour of the coupled ocean-sea ice system. Ph.D. thesis, Université Catholique de Louvain, 231.

Häkkinen, S., 1999. Variability of the simulated meridional heat transport in the North Atlantic for the period 1951–1993. *Journal of Geophysical Research,* 104(C5), pp. 10991-11007.

Han, G. et al., 2010. Decline and partial rebound of the Labrador Current 1993–2004: Monitoring ocean currents from altimetric and conductivity-temperature-depth data. *Journal of Geophysical Research: Oceans,* Volume 115.

Hansen, B., Larsen, K., Hátún, H. & Østerhus, S., 2016. A stable Faroe Bank Channel overflow 1995-2015. *Ocean Science,* Volume 12, p. 1205–1220.

Hansen, B. & Østerhus, S., 2007. Faroe Bank Channel overflow 1995–2005. *Progress in Oceanography* , 75(817-856).

Jourdan, D., Balopoulos, E., Garcia-Fernandez, M.-J. & Maillard, C., 1998. Objective analysis of temperature and salinity historical data set over the Mediterranean basin. *OCEANS '98 Conf. Proc. (Volume: 1). Piscataway, 82–87.*

Kalnay, E., Kanamitsu, M., Kistler, R. & Coauthors, 1996. The NCEP/NCAR 40-year reanalysis project. *Bull. Amer. Meteor. Soc.*, Volume 77, p. 437–471.

Kanzow, T. & Zenk., W., 2014. Structure and transport of the Iceland Scotland Overflow plume along the Reykjanes Ridge in the Iceland Basin. *Deep Sea Research Part I: Oceanographic Research Papers* , Volume 86, pp. 82-93.

Kieke, D. et al., 2009. Variability and propagation of Labrador Sea Water in the southern subpolar North Atlantic. *Deep Sea Res. I,* Volume 56, pp. 1656-1674.

Kieke, D. et al., 2007. Changes in the pool of Labrador Sea Water in the subpolar North Atlantic. *Geophysical Research Letters,* 34(6).

Kieke, D. & Yashayaev, 2015. Studies of Labrador Sea Water formation and variability in the subpolar North Atlantic in the light of international partnership and collaboration. *Progress in Oceanography,* Volume 132, pp. 220-232.

Knauss, J., 1997. Introduction to physical oceanography. Waveland Press, Inc.. p. 338 .

Knight, J., Folland, C. & Scaife, A., 2006. Climate impacts of the Atlantic multidecadal oscillation. *Geophysical Research Letters,* 33(17).

Lankhorst, M. & Zenk, W., 2006. Lagrangian Observations of the Middepth and Deep Velocity Fields of the Northeastern Atlantic Ocean. *Journal of Physical Oceanography,* Volume 36, pp. 43-63.

Latif, M. et al., 2006. Is the thermohaline circulation changing?. *Journal of Climate,* 19(18)), pp. 4631-4637.

Lavender, K. L., Owens, W. B. & Davis, R. E., 2005. The mid-depth circulation of the subpolar North Atlantic Ocean as measured by subsurface floats. *Deep-Sea Research I,* Volume 52, pp. 767-785.

Levitus, S. & Coauthors, 1998. *NOAA Atlas NESDIS 18, World Ocean Database 1998: vol. 1: Introduction. U.S. Government Printing Office, Washington D.C..*

Lozier, M., 1997. Evidence for large-scale eddy-driven gyres in the North Atlantic. *Science,* 277(5324)), pp. 361-364.

Lozier, M., Roussenov, V., Reed, M. & Williams, R., 2010. Opposing decadal changes for the North Atlantic meridional overturning circulation. *Nature Geoscience,* , 3(10), p. 728.

Lozier, M. S., 2012. Overturning in the North Atlantic. *Annual review of marine science,* Volume 4, pp. 291-315.

Lozier, M. S., Bacon, S., Bower, A. S. & coauthors, 2016. Overturning in the Subpolar North Atlantic Program: a new international ocean observing system. *Bulletin of the American Meteorological Society.*

Lozier, M. S., Gary, S. F. & Bower, A. S., 2013. Simulated pathways of the overflow waters in the North Atlantic: Subpolar to subtropical export. *Deep Sea Research Part II: Topical Studies in Oceanography* , Volume 85, pp. 147-153.

Machín, F., Send, U. & Zenk., W., 2006. Intercomparing drifts from RAFOS and profiling floats in the deep western boundary current along the Mid-Atlantic Ridge. *Scientia Marina* , Volume 70.1, pp. 1-8.

Marotzke, J. & Klinger, B. A., 2000. The dynamics of equatorially asymmetric thermohaline circulations. *Journal of Physical Oceanography,* 30(5), p. 955–970.

Marshall, J. et al., 1997. A finite-volume, incompressible Navier Stokes model for studies of the ocean on parallel computers. *Journal of Geophysical Research: Oceans,* 102(C3), pp. 5753-5766.

McCarthy, G. et al., 2012. Observed interannual variability of the Atlantic meridional overturning circulation at 26.5 N. *Geophysical Research Letters,* 39(19).

McCartney, M. S., 1992. Recirculating components to the deep boundary current of the northern North Atlantic. *Progress in Oceanography* , Volume 29, pp. 283-383.

Molinari, R. L. et al., 1998. The arrival of recently formed Labrador sea water in the Deep Western Boundary Current at 26.5°N. *Geophys. Research Letters,* Volume 25, pp. 2249-2252.

Olsen, S., Hansen, B., Quadfasel, D. & Østerhus, S., 2008. Observed and modelled stability of overflow across the Greenland–Scotland ridge. *Nature,* 455(7212), p. 519.

Pena-Molino, B., Joyce, T. M. & Toole, J. M., 2011. Recent changes in the Labrador Sea Water within the deep western boundary current southeast of Cape Cod. *Deep-Sea Research I,* Volume 58, pp. 1019-1030.

Pickart, R., 1992. Water mass components of the North Atlantic deep western boundary current. *Deep Sea Research Part A: Oceanographic Research Papers* , 39(9), pp. 1553-1572.

Pickart, R. S. & Spall, M. A., 2007. Impact of Labrador Sea Convection on the North Atlantic Meridional Overturning Circulation. *Journal of Physical Oceanography* , Volume 37, , pp. 2207-2227.

Pickart, R. S., Torres, D. J. & Clarke, R. A., 2002. Hydrography of the Labrador Sea during active convection. *Journal of Physical Oceanography* , Volume 32, pp. 428-457.

Pillar, H., Heimbach, P., Johnson, H. & Marshall, D., 2016. Dynamical attribution of recent variability in Atlantic overturning. *Journal of Climate,* 29(9), pp. 3339-3352.

Polo, I., Robson, J., Sutton, R. & Balmaseda, M., 2014. The importance of wind and buoyancy forcing for the boundary density variations and the geostrophic component of the AMOC at 26 N. *Journal of Physical Oceanography,* 44(9), pp. 2387-2408.

Rhein, M. et al., 2002. Labrador Sea Water: Pathways, CFC inventory, and formation rates. *Journal of Physical Oceanography* , Volume 32, pp. 648-665.

Rhein, M. et al., 2011. Deep water formation, the subpolar gyre, and the meridional overturning circulation in the subpolar North Atlantic. *Deep-Sea Res. II,* Volume 58, pp. 1819-1832.

Rhein, M., Kieke, D. & Steinfeldt, R., 2015. Advection of North Atlantic Deep Water from the Labrador Sea to the southern hemisphere. *Journal of Geophysical Research: Oceans,* , Volume 120, pp. 2471-2487.

Roberts, C. et al., 2013. Atmosphere drives recent interannual variability of the Atlantic meridional overturning circulation at 26.5 N. *Geophysical Research Letters,* 40(19), pp. 5164-5170.

Rudels, B., Friedrich, H. J. & Quadfasel, D., 1999. The Arctic Circumpolar Boundary Current. *Deep Sea Research Part II: Topical Studies in Oceanography* , Volume 46, pp. 1023-1062.

Sarafanov, A., 2009. On the effect of the North Atlantic Oscillation on temperature and salinity of the subpolar North Atlantic intermediate and deep waters. *ICES Journal of Marine Science,* Volume 66, pp. 1448-1454.

Saunders, P. M., 1994. The flux of overflow water through the Charlie-Gibbs Fracture Zone. *Journal of Geophysical Research ,* Volume 99, p. 12343.

Saunders, P. M., 1996. The Flux of Dense Cold Overflow Water Southeast of Iceland. *Journal of Physical Oceanography,* Volume 26, pp. 85-95.

Schott, F. A., Fischer, J., Dengler, M. & Zantopp, R., 2006. Variability of the Deep Western Boundary Current east of the Grand Banks. *Geophysical Research Letters ,* Volume 33.

Schott, F. A. et al., 2004. Circulation and Deep-Water Export at the Western Exit of the Subpolar North Atlantic. *Journal of Physical Oceanography, ,* Volume 34, pp. 817-843.

Schott, F., Stramma, L. & Fischer, J., 1999. Interaction of the North Atlantic Current with the Deep Charlie Gibbs Fracture Zone Throughflow. *Geophysical Research Letters,* Volume 26, pp. 369-372.

Schott, F. et al., 2004. Circulation and deep-water export at the western exit of the subpolar North Atlantic. *Journal of Physical Oceanography,* 34(4), pp. 817-843.

Serreze, M., Holland, M. & Stroeve, J., 2007. Perspectives on the Arctic's shrinking sea-ice cover. *Science,* 315(5818), pp. 1533-1536.

Sherwin, T. J., Griffiths, C. R., Inall, M. E. & Turrell, W. R., 2008. Quantifying the overflow across the Wyville Thomson Ridge into the Rockall Trough. *Deep Sea Research Part I: Oceanographic Research Papers ,* 55(4), pp. 396-404.

Sherwin, T. J. & Turrell, W. R., 2005. Mixing and advection of a cold water cascade over the Wyville Thomson Ridge. *Deep Sea Research Part I: Oceanographic Research Papers ,* 52(1392-1413).

Smethie, W., Fine, R., Putzka, A. & Jones, E., 2000. Tracing the flow of North Atlantic Deep Water using chlorofluorocarbons. *Journal of Geophysical Research: Oceans,* 105(C6), pp. 14297-14323.

Steele, M., Morley, R. & Ermold, W., 2001. PHC: A Global Ocean Hydrography with a High Quality Arctic Ocean. *Journal of Climate,* Volume 14, p. 2079–2087.

Stommel, H. & Arons, A., 1959. On the abyssal circulation of the world ocean—I. Stationary planetary flow patterns on a sphere. *Deep Sea Research (1953),* Volume 6, pp. 140-154.

Stramma, L. et al., 2004. Deep water changes at the western boundary of the subpolar North Atlantic during 1996 to 2001. *Deep-Sea Research I,* Volume 51, pp. 1033-1056.

Takahashi, T. et al., 2009. Climatological mean and decadal change in surface ocean pCO2, and net sea–air CO2 flux over the global oceans. *Deep Sea Research Part II: Topical Studies in Oceanography,* 56(8-10), pp. 554-577.

Talley, L. & McCartney, M., 1982. Distribution and circulation of Labrador Sea water. *Journal of Physical Oceanography,* 12(11), pp. 1189-1205.

Tett, S., Sherwin, T., Shravat, A. & Browne, O., 2014. How much has the North Atlantic Ocean overturning circulation changed in the last 50 years?. *Journal of Climate,,* 27(16), pp. 6325-6342.

The DRAKKAR Group, 2007. Eddy-permitting ocean circulation hindcasts of past decades. *CLIVAR Exchanges,* Volume 12, p. 8–10.

Toole, J. et al., 2017. Moored observations of the Deep Western Boundary Current in the NW Atlantic: 2004–2014. *Journal of Geophysical Research: Oceans,* 122(9), pp. 7488-7505.

Trenberth, K., Olson, J. & Large, W., 1989. A global ocean wind stress climatology based on ECMWF analyses. Climate and Global Dynamic Division, National Center for Atmospheric Research, Boulder.

van Aken, H. M., 1995. Hydrographic variability in the bottom layer of the Iceland Basin. *Journal of physical oceanography,* 25(7), pp. 1716-1722.

van Aken, H. M. & Boer, C. J. D., 1995. On the synoptic hydrography of intermediate and deep water masses in the Iceland Basin. *Deep Sea Research Part I: Oceanographic Research Papers* , Volume 42, pp. 165-189.

van Aken, H. M., Jong, M. F. D. & Yashayaev, I., 2011. Decadal and multi-decadal variability of Labrador Sea Water in the north-western North Atlantic Ocean derived from tracer distributions: Heat budget, ventilation, and advection. *Deep-Sea Research I,* Volume 58, pp. 505-523.

van Sebille, E. et al., 2011. Propagation pathways of classical Labrador Sea water from its source region to 26°N. *Journal of Geophysical Research* , 116(C12027).

Vellinga, M. & Wood, R., 2008. Impacts of thermohaline circulation shutdown in the twenty-first century. *Climatic Change,* 91(1-2), pp. 43-63.

Xie, P. & Arkin, P., 1997. Global Precipitation: A 17-Year Monthly Analysis Based on Gauge Observations, Satellite Estimates, and Numerical Model Outputs. *Bull. Amer. Meteor. Soc.,* Volume 78, pp. 2539-2558.

Xu, X., Rhines, P. B., Chassignet, E. P. & Schmitz, W. J., 2015. Spreading of Denmark Strait Overflow Water in the Western Subpolar North Atlantic: Insights from Eddy-Resolving Simulations with a Passive Tracer. *Journal of Physical Oceanography,* 45(2913-29).

Xu, X. et al., 2010. Transport of Nordic Seas overflow water into and within the Irminger Sea: An eddy-resolving simulation and observations. *Journal of Geophysical Research* , Volume 115.

Yashayaev, I., 2007. Hydrographic changes in the Labrador Sea, 1960–2005. *Progress in Oceanography,* Volume 73, pp. 242-276.

Yashayaev, I. & Loder, J., 2009. Enhanced production of Labrador Sea Water in 2008. *Geophysical Research Letters,* Volume 36.

Yashayaev, I. & Loder, J., 2017. Further intensification of deep convection in the Labrador Sea in 2016. *Geophysical Research Letters,* 44(3), pp. 1429-1438.

Yeager, S., 2015. Topographic coupling of the Atlantic overturning and gyre circulations. *Journal of Physical Oceanography,* 45(5), pp. 1258-1284.

Yeager, S. & Danabasoglu, G., 2014. The origins of late-twentieth-century variations in the large-scale North Atlantic circulation. *Journal of Climate,* 27(9), pp. 3222-3247.

Zhang, R., 2008. Coherent surface-subsurface fingerprint of the Atlantic meridional overturning circulation. *Geophysical Research Letters,* 35(20).

Zhang, R., 2010. Latitudinal dependence of Atlantic meridional overturning circulation (AMOC) variations. *Geophysical Research Letters,* 37(16).

Zhang, R. & Delworth, T., 2006. Impact of Atlantic multidecadal oscillations on India/Sahel rainfall and Atlantic hurricanes. *Geophysical Research Letters,* 33(17).

Zhao, J. & Johns, W., 2014. Wind-forced interannual variability of the Atlantic Meridional Overturning Circulation at 26.5° N. *Journal of Geophysical Research: Oceans,* 119(4), pp. 2403-2419.

Zou, S. & Lozier, M., 2016. Breaking the linkage between Labrador Sea Water production and its advective export to the subtropical gyre. *Journal of Physical Oceanography,* 46(7), pp. 2169-2182.

Zou, S. et al., 2017. Observed and Modeled Pathways of the Iceland Scotland Overflow Water in the eastern North Atlantic. *Progress in Oceanography.*

Biography

Sijia Zou was born on January 23rd, 1991 in Zibo, Shandong, China. She earned a B.S. with honors in Marine Sciences from Ocean University of China in 2013. She has published two peer-reviewed articles as the first author (Zou and Lozier 2016; Zou et al. 2017). Sijia has also published two conference papers as the first author (Zou and Yi, 2012a; Zou and Yi, 2012b). She received a National Scholarship from The National Ministry of Education in China in 2012, a Science and Technology Innovation Scholarship from Ocean University of China (OUC) in 2012, a ZhangZi Island Scholarship for Top Hundred Outstanding Students from OUC in 2012, Outstanding Student Scholarships from OUC in 2009, 2010, and 2011, Scholarships for Excellent Academic Achievements from OUC in 2009, 2010, and 2011.

Zou, S. & Lozier, M., 2016. Breaking the linkage between Labrador Sea Water production and its advective export to the subtropical gyre. *Journal of Physical Oceanography,* 46(7), pp. 2169-2182.

Zou, S. et al., 2017. Observed and Modeled Pathways of the Iceland Scotland Overflow Water in the eastern North Atlantic. *Progress in Oceanography.*

Zou, S. & Yi, L., 2012a, May. Features of northwest passage variation of sea ice concentration from 2002 to 2010 and analysis of possible reasons. *In Systems and Informatics (ICSAI), 2012 International Conference, IEEE,* pp. 2403-2406.

Zou, S. & Yi, Li., 2012b, July. Computer Simulation of the Influence on Sea Ice Concentration Caused by Sea Surface Temperature and Sea Level Pressure. In *Computing, Measurement, Control and Sensor Network (CMCSN), 2012 International Conference, IEEE,* pp. 261-264.